

# Global Simulation of Noble Gases and Their Binary Mixtures

Inaugural-Dissertation  
zur Erlangung des Doktorgrades  
der Mathematisch-Naturwissenschaftlichen Fakultät  
der Universität zu Köln

Afshin Eskandari Nasrabad  
aus Mashad-Iran  
April 3, 2003

To my mother and to Rozita, for the love and encouragement that you have given me while I was doing my PhD.

Berichterstatter: Prof. Dr. U. K. Deiters  
Institut für Physikalische Chemie  
Universität zu Köln

Prof. Dr. R. Strey  
Institut für Physikalische Chemie  
Universität zu Köln

## Acknowledgment

It is my pleasure to acknowledge following people who have contributed to the preparation of this thesis.

I would like to thank my supervisor, Prof. Dr. U. K. Deiters, for inviting me into his group and for providing me with an interesting project. I am especially grateful for his support and for his help in overcoming administrative problems. Without his insight it would not have been possible to complete this thesis.

I am grateful to Prof. Dr. R. Strey for his support of this project.

I would also like to thank the Regional Computation Center of Cologne for a generous allowance of CPU time.

# Contents

<b>Contents</b>	<b>6</b>
<b>Abstract</b>	<b>13</b>
<b>Zusammenfassung</b>	<b>15</b>
<b>1 Introduction</b>	<b>17</b>
<b>2 Simulation of Phase Equilibria</b>	<b>21</b>
2.1 Introduction . . . . .	22
2.2 Simulations including a direct interface . . . . .	22
2.3 <i>NPT</i> plus test particle method . . . . .	22
2.4 Gibbs Duhem integration . . . . .	24
2.5 Gibbs ensemble simulation . . . . .	26
2.5.1 The formulation of technique . . . . .	26
2.5.2 Chemical potential . . . . .	30
2.5.3 Determination of critical points . . . . .	31
2.5.4 Variations of the technique . . . . .	32
<b>3 Van der Waals Interactions</b>	<b>35</b>
3.1 Introduction . . . . .	36
3.2 Empirical models . . . . .	38
3.3 <i>Ab initio</i> calculation of van der Waals forces . . . . .	42
3.3.1 Perturbation approach . . . . .	43
3.3.2 Supermolecular approach . . . . .	46
3.3.3 Basis set . . . . .	47
3.3.4 Many-body interactions . . . . .	48

3.3.5	Extrapolation and fitting the potential surfaces . . .	50
<b>4</b>	<b>The gemc Program</b>	<b>53</b>
4.1	Introduction . . . . .	54
4.2	The program gemc . . . . .	54
4.2.1	Initialization . . . . .	54
4.2.2	The main() function . . . . .	54
4.2.3	Analysis of results . . . . .	56
4.3	Simulation details . . . . .	56
4.3.1	Pure fluids . . . . .	56
4.3.2	Binary mixture fluids . . . . .	57
<b>5</b>	<b>Results and discussion</b>	<b>59</b>
5.1	Neon . . . . .	60
5.1.1	Potentials . . . . .	60
5.1.2	Simulations . . . . .	62
5.1.3	Quantum corrections . . . . .	66
5.2	Argon . . . . .	69
5.2.1	Potentials . . . . .	69
5.2.2	Simulations . . . . .	71
5.3	Krypton . . . . .	75
5.3.1	Potentials . . . . .	75
5.3.2	Simulations . . . . .	78
5.4	The binary mixture neon–argon . . . . .	80
5.4.1	Potentials . . . . .	80
5.4.2	Simulations . . . . .	83
5.5	The binary mixture argon–krypton . . . . .	87
5.5.1	Potentials . . . . .	87
5.5.2	Simulations . . . . .	90
<b>6</b>	<b>Conclusion</b>	<b>95</b>
	<b>Bibliography</b>	<b>99</b>
<b>A</b>	<b>Tables</b>	<b>107</b>

# List of Figures

2.1	Test particle method . . . . .	23
2.2	<i>NPT</i> plus test particle method . . . . .	24
2.3	Gibbs-Duhem integration . . . . .	25
2.4	Periodic boundary conditions . . . . .	27
2.5	Gibbs ensemble algorithm . . . . .	28
2.6	Particle identity exchange mechanism . . . . .	33
3.1	Intermolecular forces classification . . . . .	37
3.2	Lennard-Jonse potential . . . . .	39
3.3	Exp-6 potential . . . . .	41
4.1	Schematic representation of the <code>gemc</code> program . . . . .	55
5.1	Potential energy surface of the neon dimer . . . . .	61
5.2	Second virial coefficients of neon . . . . .	61
5.3	Comparison of density of the coexisting phases for neon obtained from the simulations and experiments. . . . .	63
5.4	Comparison of the vapor pressures for neon obtained from the simulations and experiment. . . . .	64
5.5	Comparison of density of coexisting phases for neon obtained from the simulations and experiments . . . . .	65
5.6	Comparison of density of coexisting phases for neon obtained from the simulations and experiments . . . . .	66
5.7	Comparison of density of the coexisting phases for neon obtained from the simulations, equation of state, and experiments . . . . .	67
5.8	Comparison of the vapor pressures for neon obtained from the simulations, equation of state, and experiments. . . . .	68

5.9	Potential energy surface of the argon dimer . . . . .	70
5.10	Second virial coefficients of argon. . . . .	70
5.11	Comparison of density of the coexisting phases for argon obtained from the simulations and experiments . . . . .	72
5.12	Comparison of the vapor pressure for argon obtained from the simulations and experiments . . . . .	73
5.13	Comparison of density of the coexisting phases for argon obtained from the simulations and experiments . . . . .	74
5.14	Comparison of the vapor pressures for argon obtained from the simulations and experiments . . . . .	75
5.15	Potential energy surface of the krypton dimer . . . . .	76
5.16	Second virial coefficients of krypton . . . . .	76
5.17	Comparison of density of the coexisting phases for krypton obtained from the simulations and experiments . . . . .	79
5.18	Comparison of the vapor pressures of krypton obtained from the simulations and experiments . . . . .	80
5.19	Potential energy surface of the neon–argon dimer . . . . .	81
5.20	Pressure-composition diagram for the neon–argon mixtures at 95.82 K . . . . .	84
5.21	Pressure-composition diagram for the neon–argon mixtures at 101.94 K . . . . .	85
5.22	Pressure-composition diagram for the neon–argon mixtures at 110.78 K . . . . .	86
5.23	Pressure-composition diagram for the neon–argon mixtures at 121.36 K . . . . .	87
5.24	Pressure-composition diagram for the neon–argon mixtures at 129.93 K . . . . .	88
5.25	Potential energy surfaces of the argon–krypton dimer . . . . .	89
5.26	Pressure-composition diagram for the argon–krypton system at 158.15 K . . . . .	90
5.27	Pressure-composition diagram for the argon–krypton system at 163.15 K . . . . .	91
5.28	Pressure-composition diagram for the argon–krypton system at 177.38 K . . . . .	92
5.29	Pressure-composition diagram for the argon–krypton system at 193.15 K . . . . .	93



# List of Tables

3.1	Four types of forces . . . . .	36
3.2	Lennard-Jones critical parameters . . . . .	40
5.1	Characteristic properties of the neon–neon potentials . . .	60
5.2	Critical properties for neon . . . . .	64
5.3	Charactristic Properties of Ar–Ar Potentials . . . . .	69
5.4	Critical Parameters For Argon . . . . .	73
5.5	Charactristic properties of krypton–krypton potentials . .	77
5.6	Critical properties of krypton . . . . .	78
5.7	Charactristic properties of the neon–argon potentials . . .	82
5.8	Cross second virial coefficients of neon–argon . . . . .	82
5.9	Like and unlike three-body nonadditivity coefficients of neon and argon trimers . . . . .	83
5.10	Charactristic properties of argon–krypton potentials . . . .	89
5.11	Like and unlike three-body nonadditivity coefficients of ar- gon and krypton trimers . . . . .	90
A.1	<i>ab initio</i> potentials for the neon dimer . . . . .	108
A.2	Parameters of fitting for the neoen–neon potentials . . . .	108
A.3	Simulation results of neon using the av45z potential . . . .	109
A.4	Simulation results of neon using the av45z plus AT potentials	109
A.5	Simulation results of neon using the avtz+(332) potential .	110
A.6	Simulation results of neon using the avtz+(332) plus AT potentials . . . . .	111
A.7	Simulation results of neon using the av5z potential . . . .	111
A.8	<i>ab initio</i> potentials for the argon dimer . . . . .	112
A.9	Parameters of fitting for the argon–argon potentials . . . .	112
A.10	Simulation results of argon using the av45z potential . . .	113

A.11	Simulation results of argon using the av45z plus AT potentials	113
A.12	Simulation results of argon using the av5z potential . . . . .	114
A.13	<i>ab initio</i> potentials for the krypton dimer . . . . .	114
A.14	Parameters of fitting for the krypton–krypton potentials . . . . .	115
A.15	Simulation results of krypton using the av34z potential . . . . .	115
A.16	Simulation results of krypton using the av34z plus AT potentials . . . . .	116
A.17	Simulation results of krypton using the $4d2f$ - $\{2d1f\}$ potential.	116
A.18	<i>ab initio</i> potentials for the neon–argon dimer . . . . .	117
A.19	Parameters of fitting for the neon–argon potentials . . . . .	117
A.20	Simulation results for the neon–argon mixture with the av45z potential along 101.94 K . . . . .	118
A.21	Simulation results of the neon–argon mixture with the av45z potential along 110.78 K . . . . .	119
A.22	Simulation results for the neon–argon mixture with the av45z potential along 121.36 K . . . . .	120
A.23	Simulation results for the neon–argon mixture with the av45z potential along 129.93 K . . . . .	121
A.24	Simulation results for the neon–argon mixture with the av45z plus AT potentials along 101.94 K . . . . .	122
A.25	Simulation results for the neon–argon mixture with the av45z plus AT potentials along 110.78 K . . . . .	123
A.26	Simulation results for the neon–argon mixture with the av45z plus AT potentials along 121.36 K . . . . .	124
A.27	Simulation results for the neon–argon mixture with the av45z plus AT potentials along 129.93 K . . . . .	125
A.28	Simulation results for the neon–argon mixture with the av5z potential along 95.82 K . . . . .	126
A.29	Simulation results for the neon–argon mixture with the av5z potential along 101.94 K . . . . .	127
A.30	Simulation results for the neon–argon mixture with the av5z potential along 110.78 K . . . . .	128
A.31	<i>ab initio</i> potentials for the argon–krypton dimer . . . . .	129
A.32	Parameters of fitting for the argon–krypton potential . . . . .	129
A.33	Simulation results for the argon–krypton mixture with the two-body <i>ab initio</i> potentials at 193.15 K . . . . .	130

A.34	Simulation results for the argon–krypton mixture with the two-body <i>ab initio</i> potentials at 177.38 K . . . . .	131
A.35	Simulation results for the argon–krypton mixture with the two-body <i>ab initio</i> potentials at 163.15 K . . . . .	132
A.36	Simulation results for the argon–krypton mixture with the two-body <i>ab initio</i> potentials at 158.15 K . . . . .	133
A.37	Simulation results for the argon–krypton mixture with the two-body <i>ab initio</i> potentials at 193.15 K . . . . .	134
A.38	Simulation results for the argon–krypton mixture with the two-body plus AT potentials at 177.38 K . . . . .	135
A.39	Simulation results for the argon–krypton mixture with the two-body plus AT potentials at 163.15 K . . . . .	136
A.40	Simulation results for the argon–krypton mixture with the two-body plus AT potentials at 158.15 K . . . . .	137



# Abstract

Global simulations combine quantum mechanics and molecular simulations: The potential energy surface between two molecules is calculated for a sufficient number of configurations by a standard quantum chemistry method (on a sufficient level of approximation) with suitable basis sets, then fitted to an appropriate analytical form and finally used in simulations to obtain the fluid phase equilibria.

This work aims at evaluating the adequacy of *ab initio* pair potentials plus Axilrod-Teller (AT) three-body interactions for a description of macroscopic properties of pure and binary mixtures of noble gases.

In this work, three pure noble gases, namely neon, argon, krypton, and two binary mixtures neon–argon and argon–krypton were studied. For neon–neon, argon–argon and neon–argon pair interactions the *ab initio* potentials available in literature were used. However, for krypton–krypton and krypton–argon, new *ab initio* pair potentials were developed using the CCSD(T) level of theory and two correlation consistent basis sets. An extrapolation method was used to obtain the basis set limit of the interaction energies. The resulting pair potentials were fitted to a suitable analytical form containing a repulsive exponential component and an attractive damped dispersion component. To include the interaction of trimers, Axilrod–Teller triple-dipole potentials were used.

New computer programs were developed to perform standard *NVT*-Gibbs ensemble simulations for pure systems and *NPT*-Gibbs ensemble simulations for binary mixtures.

A comprehensive investigation is reported on the simulation of pure neon using three different *ab initio* pair potentials. It turns out that the better the quality of the *ab initio* potential is, the larger discrepancies in the results of the simulations and experimental data are observed, especially

in the liquid branch. By comparison with an equation of state and a newly developed correction function it can be shown that these discrepancies are mainly due to quantum effects.

The simulation results and the predicted critical properties for pure argon are in excellent agreement with experimental data. We also present a good effective two-body potential for argon based on *ab initio* calculations.

New high quality *ab initio* potentials were developed for the krypton dimer. The results of the second virial coefficient and simulations are in good agreement with the experimental data.

For the neon–argon binary mixture, *NPT*-Gibbs ensemble simulations were performed along four isotherms, 101.94, 110.78, 121.36 and 129.93 K. The results of the simulations show that the inclusion of AT potential leads to a good agreement with experimental data. The simulations for the same system were performed with effective two-body potentials along three isotherms, 95.82 , 101.94, 110.78 K. The results are in excellent agreement with experimental data.

For the argon–krypton binary mixture, simulations were performed along four isotherms, 193.15, 177.38, 163.15 and 158.15 K. The results of simulation with two-body plus AT potentials are in good agreement with experimental data for all isotherms.

# Zusammenfassung

Globale Simulationen kombinieren Quantenmechanik und molekulare Simulationen: Die intermolekulare Potentialenergiefläche kann für eine ausreichend große Zahl von Konfigurationen mit Standardmethoden der Quantenchemie mit geeigneten Basisfunktionsmengen berechnet werden (auf einem ausreichenden Approximationsniveau), dann durch eine geeignete analytische Funktion approximiert und schließlich in Computersimulationen eingesetzt werden, um die Fluid-Phasengleichgewichte zu erhalten.

Mit dieser Arbeit sollte untersucht werden, ob Ab-initio-Paarpotentiale in Verbindung mit Axilrod–Teller (AT) Dreikörperwechselwirkungen für eine Beschreibung der makroskopischen Eigenschaften von Edelgasen und ihrer binären Mischungen ausreichen.

Es wurden in dieser Arbeit drei reine Edelgase untersucht, nämlich Neon, Argon und Krypton, sowie zwei binäre Mischungen, nämlich Neon–Argon und Argon–Krypton. Für die Paarwechselwirkungen Neon–Neon, Neon–Argon und Argon–Argon wurden aus der Literatur bekannte Ab-Initio-Paarpotentiale verwendet. Für Krypton–Krypton und Argon–Krypton mußten neue Ab-initio-Paarpotentiale verwendet werden, und zwar unter Verwendung der CCSD(T)-Approximation und zweier korrelationskonsistenter Basissätze. Eine Extrapolationsmethode wurde verwendet, um daraus das Basissatzlimit der Wechselwirkungsenergie zu ermitteln. Die resultierenden Paarpotentiale wurden mit einer geeigneten analytischen Funktion approximiert, die eine exponentielle repulsive Komponente und eine gedämpfte Dispersionsfunktion als attraktive Komponente enthielt. Die Wechselwirkung von Trimeren wurde mit Dreifach-Dipolpotentialen nach Axilrod und Teller berücksichtigt.

Für die Computersimulation von Reinstoffen im Standard-NVT-Gibbs-Ensemble sowie von Mischungen im NPT-Gibbs-Ensemble wurden neue

Computerprogramme entwickelt.

Für Neon wurde eine umfassende Untersuchung durchgeführt, bei der drei verschiedene Ab-initio-Potentiale verglichen wurden. Dabei stellte sich heraus, daß die Abweichungen zwischen Simulation und Experiment umso größer wurden, je höher die Qualität des Ab-initio-Potentials war, und zwar besonders bei Simulationen flüssiger Phasen. Durch Vergleich mit einer Zustandsgleichung und einer neuentwickelten Quentenkorrekturfunktion konnte gezeigt werden, daß diese Abweichungen tatsächlich im wesentlichen auf Quanteneffekte zurückzuführen sind.

Die Simulationsergebnisse für Argon und die daraus vorhergesagten kritischen Daten stimmen ausgezeichnet mit den experimentellen Werten überein.

Es wird auch ein gutes effektives Zweikörper-Potential für Argon vorgestellt, das auf Ab-initio-Rechnungen beruht.

Neue, hochgenaue Ab-initio-Potentiale wurden auch für das Krypton-Dimere entwickelt. Die Ergebnisse für den zweiten Virialkoeffizienten und die Simulationen für das Phasengleichgewicht stimmen gut mit den experimentellen Daten überein.

Für das binäre System Neon–Argon wurden NPT-Gibbs-Ensemble Simulationen entlang vier Isothermen durchgeführt, nämlich 101,94, 110,78, 121,36 und 129,93 K. Die Simulationsergebnisse zeigen, daß die Verwendung des AT-Potentials zu einer guten Übereinstimmung mit den experimentellen Daten führt. Für das gleiche System wurden auch Simulationen mit einem effektiven Zweikörper-Potential entlang drei Isothermen durchgeführt, nämlich 95,82, 101,94, und 110,78 K. Die Resultate stimmen sehr genau mit den experimentellen Daten überein.

Für das binäre System Argon–Krypton wurden Simulationen entlang vier Isothermen durchgeführt, nämlich 193,15, 177,38, 163,15 und 158,15 K. Die Ergebnisse der Simulationen unter Verwendung von Zweikörper-Potentialen in Verbindung mit AT-Potentialen stimmen für alle Isothermen gut mit den experimentellen Werten überein.



# Chapter 1

## Introduction

The phase properties of pure fluids and their mixtures play an important role in many scientific and technological fields as well as in chemical, petrochemical and pharmaceutical industries. An enormous amount of experimental data has been collected through years and many efforts have been made to understand the phase transition phenomena. Many theoretical as well as empirical models have been developed to correlate and extend the existing experimental data.

In the course of the recent decades, with the rapidly increasing speed of computers and also a plunge in costs of CPU time, molecular simulations have become important tools for the calculations of the equilibrium as well as non-equilibrium thermophysical properties of fluids.

Molecular simulations can be performed in two different ways:

1. Molecular dynamic simulations, in which the equations of motion describing the classical mechanical motion of particles are averaged to obtain the macroscopic thermophysical properties.
2. Monte Carlo simulations, in which for a statistical ensemble with some fixed variables, configurations of a system of particles are generated by a Markov chain process. Thermophysical properties of system are obtained by taking the configurational averages .

In Monte Carlo simulations, there are two approaches for the calculation of the phase equilibria: direct and indirect. In the direct approach, thermophysical properties of both phases are determined simultaneously. Indirect simulation methods are mainly based on the calculations of the chemical potentials. For a series of state points, the chemical potentials are calculated; a phase coexistence point is determined by the intersection of vapor and liquid branches in the pressure-chemical potential projection diagram.

A direct simulation method was introduced by Panagiotopoulos, which consists of setting up two boxes, each box represents a homogeneous phase within periodic boundary conditions. Three (or more) Monte Carlo moves are performed to fulfill the equilibrium requirements. The technique has been widely used to study a large variety of systems.

A sufficient knowledge of intermolecular interactions is necessary for the simulation of a system. Until now, mostly empirical potentials have been exclusively used in simulations. These potentials have usually simple

analytical forms with few empirical parameters whose numerical values are determined from experimental data. The usefulness of these potentials is evident, however, there are limitations attached to them. First, the parameters are valid in the range of experiments only to which they have been fitted. Second, in the case of mixtures, mixing rules must be used which may not be accurate. Third, the potential energy surface may not contain any detailed informations of anisotropy of molecules. On the other hand, the *ab initio* calculation of the interaction potentials is possible by a standard quantum chemistry method and a suitable choice of basis sets. With the present computational resources, it is possible to calculate the interaction energies for the small and medium sized molecules with high accuracy.

A combination of quantum mechanics and molecular simulation is possible in the framework of *ab initio* simulation, in which at each simulation step, a complete *ab initio* calculation of the energy (or force in molecular dynamics) for the whole configuration of molecules is done. At present, such calculations are performed in *ab initio* molecular dynamics according to the so-called Car–Parrinello method. Such calculations, which are quite time consuming, have been used successfully for the systems including strong intermolecular interactions (like hydrogen bonds). However, this type of calculations fails for complexes interacting with dispersion forces.

In the framework of global simulations, combination of quantum mechanics and molecular simulation is possible in a simpler way, in which the potential energy surface between two molecules for a sufficient number of configurations is calculated by a standard *ab initio* method. The resulting potential surface is fitted to an analytical form and finally used in simulations. The method is useful especially in the case of van der Waals fluids, for which Car–Parrinello molecular dynamics is not applicable.

For several reasons, noble gases have been the subject of many studies in simulations. First of all, their interaction potentials are spherical. It means that the potential energy is a function of interatomic distance only. Second, for most of them accurate empirical potentials are available. The quality of the *ab initio* potentials can be compared with these empirical potentials. Third, the phase equilibria are well known for all of them. And finally, for most of them, the potential energy surface can be calculated with high accuracy using *ab initio* methods. For the first three noble gases,

accurate *ab initio* potentials have already been reported in literature. A fully occupied d-shell in the krypton atom makes the *ab initio* calculations very expensive (if high accuracy is important). The *ab initio* calculations for xenon atom (or generally for massive atoms) is done with the use of frozen core orbitals. Moreover, a relativistic treatment for the *ab initio* calculation of xenon atom is needed.

In the present work the central idea of global simulations was used to calculate the phase equilibria of noble gases and their binary mixtures. In this way, effects of three-body interactions on the phase equilibria were also studied.

The material of Chapter 2 introduces different simulation techniques for the calculations of phase equilibria.

Chapter 3 discusses the calculations of van der Waals interactions.

Chapter 4, a description of the **gemc** program is presented. the program was developed for the calculations of phase equilibria using the Gibbs Ensemble Monte Carlo simulations of pure and binary mixtures. In this chapter, details of the simulations are also viewed.

The results of the present work are presented in chapter 5.

Chapter 6 offers the conclusions.

## **Chapter 2**

# **Simulation of Phase Equilibria**

## 2.1 Introduction

Knowledge of the phase equilibria of fluids is essential for many industrial and scientific fields. Over the last century significant experimental efforts have been made toward the determination of phase diagrams [1]. Phase equilibria have also been the topic of many theoretical studies such as the integral equations theories [3] and equation of states [4]. Molecular simulation has become an important tool in the study of fluid phase equilibria and several new techniques have been developed [5].

In this chapter, we briefly discuss different Monte Carlo techniques for simulations of the phase equilibria.

## 2.2 Simulations including a direct interface

The technique is physically meaningful and straightforward for a system with two phases and an explicit interface in between. However, there are difficulties concerning the setting up and equilibration of such a system. The natural choice of the interface needs to select a large number of particles which in fluids with low vapor pressures for any reasonable system size, very few particles can be found in the gas phase. Even for simple spherically symmetric potentials, a typical simulation of this kind needs a large amount of CPU time for equilibration.

## 2.3 *NPT* plus test particle method

The central idea of the method [6] is simply to specify the phase equilibrium from the intersection of the vapor and liquid branches in the chemical potential-pressure projection diagram; in other words, simulations are performed for each phase separately. An alternative method is to use an equation of states to calculate the chemical potentials of the gaseous branch [7].

Chemical potentials in simulations are often calculated using Widom's theorem [8]:

$$\beta\mu = -\ln \left\langle \exp(-\beta U^\dagger) \right\rangle + \ln \rho \quad (2.1)$$

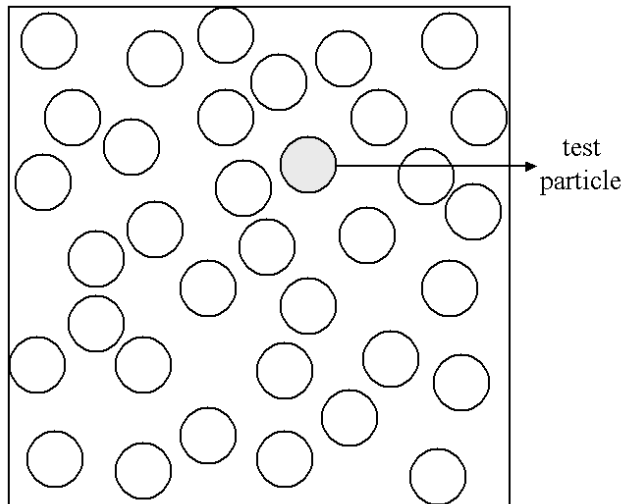


Figure 2.1: Widom test particle method.

where  $\mu$  is the chemical potential of a species in a system,  $U^\dagger$  is the interaction energy of a test particle with the other particles in the simulation box, and  $\rho$  is the density. Figure 2.1 shows the test particle (dashed circle) interacting with real particles (full circles) of a fluid.

The same method can be applied to find fluid phase equilibria using Grand Canonical Monte Carlo (GCMC) simulation. In such ensemble, temperature  $T$ , volume  $V$ , and chemical potential  $\mu$  are kept constant. Creation and annihilation of particles are performed to obtain the equilibrium density at a given  $\mu VT$ .

Figure 2.2 represents the searching method for finding the phase coexistence pressure and corresponding chemical potential in *NPT* plus test particle method or GCMC simulations for a one component system. The coexistence point is calculated as intersection of the two branches. The liquid branch (at far enough from the critical point) is almost horizontal and a small number of simulations requires to span a wide range of pressures. Möller and Fischer [6] used the same idea to determine the coexistence properties of the pure Lennard-Jones fluid with a very high accuracy.

While this method is useful for simple one-component systems, an excessively large number of simulations are required to determine the fluid

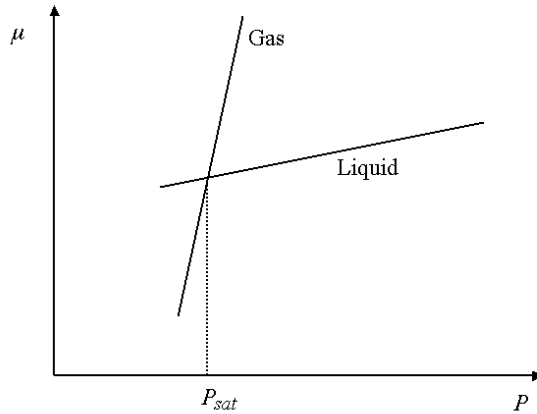


Figure 2.2: Determination of  $P_{\text{sat}}$  in  $NPT$  plus test particle method.

phase equilibria for a binary or multicomponent systems. For high-density fluids or solids and for multisegment large molecules, the technique fails due to overlap of test particle with other particles.

## 2.4 Gibbs Duhem integration

Gibbs-Duhem integration is simply a thermodynamic integration along a coexistence curve. A comprehensive review of this technique is available somewhere else [9]. The mathematical basis of Gibbs-Duhem integration can be described by writing the Clapeyron equation for a one component fluid,

$$\frac{dP}{d\beta} = -\frac{h^{\text{I}} - h^{\text{II}}}{\beta(v^{\text{I}} - v^{\text{II}})} \quad (2.2)$$

where  $h$  and  $v$  stand for molar enthalpy and volume, respectively, and superscripts I and II denote the phases. Kofke [10] showed that the equation 2.2 can be integrated numerically using Monte Carlo simulation. An initial point (physical condition) must be known; such a point can be calculated by means of other simulation techniques (for instance Gibbs ensemble)



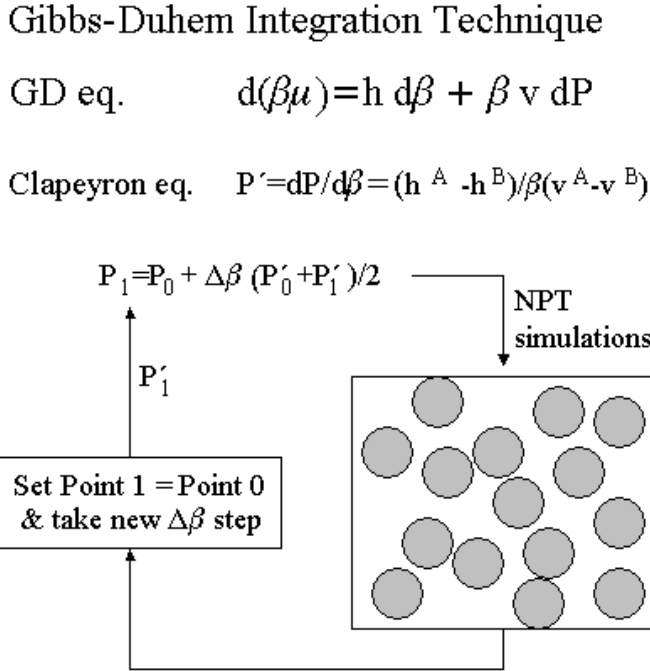


Figure 2.3: Gibbs-Duhem integration method in *NPT* ensemble.

or can be selected from experimental data. A proper statistical mechanical ensemble (for example isobaric-isothermal ensemble) can be applied to estimate the  $dP/d\beta$  term using a standard numerical integration (e.g., trapezoid). The most appealing aspect of this method is that, for pure systems, there is no need to calculate the chemical potential of the component and as a result avoiding the difficulties of particle insertion technique. Figure 2.3 shows the Gibbs-Duhem integration technique between two phase points along the vapor-liquid coexistence curve based on *NPT* simulations.

It is possible to implement the Gibbs-Duhem integration technique to the grand canonical ensemble simulations [12]. In this case, the Gibbs-

Duhem equation must be solved for chemical potential derivatives,

$$\frac{d\mu}{d\beta} = \frac{v^I h^I - v^{II} h^{II}}{v^I - v^{II}} \quad (2.3)$$

While this technique excels in calculations of solid-fluid coexistence, it suffers from propagation of errors in initial conditions resulting from uncertainties in the coexistence properties [10]. Such errors typically increase when approaching the critical point. Extensions of the method to calculations of multicomponent systems have been reported [11], however, for such a case, the method cannot avoid costly particle transfer.

## 2.5 Gibbs ensemble simulation

The Gibbs ensemble Monte Carlo simulation [13, 14] is a powerful technique to study fluid phase equilibria in fluids. These kind of simulations are performed in two (or more) separate regions, each of them representing a small part of a homogeneous phase. Conventional periodic boundary conditions [15] are implemented in each region to avoid dealing with a direct interface. Figure 2.4 shows the selection of simulation boxes from two phases far from the interface, in this technique.

While for pure systems, the total number of particles  $N$ , total volume  $V$ , and temperature  $T$ , are kept constant ( $NVT$ -Gibbs ensemble), for mixtures, the total number of each species  $\{N_A, N_B, \dots\}$ , pressure  $P$ , and temperature  $T$ , are kept constant ( $NPT$ -Gibbs ensemble). Three different Monte Carlo trial moves are needed to obtain the fluid phase equilibria, namely, particle displacements, volume changes and particle transfers between the two regions. The equilibrium conditions are assured by equality of pressures and chemical potentials of different species in each region. A schematic diagram of Gibbs ensemble methodology is given in Figure 2.5.

### 2.5.1 The formulation of technique

Originally, Panagiotopoulos derived the approximate mathematical formulation of Gibbs ensemble simulations from fluctuation theory [13]. Subsequently, the exact expressions of the acceptance criteria were reported [14], which resulted in a difference in the acceptance criteria for the

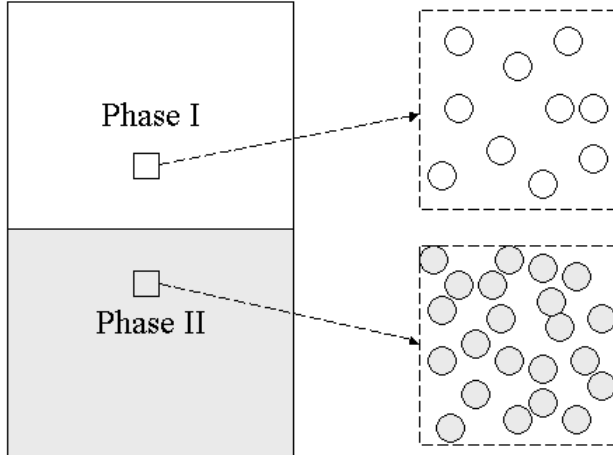


Figure 2.4: Selection of simulation boxes in Gibbs ensemble technique. Dotted lines represent the periodic boundary conditions.

particle transfer proportional to  $1/N$ . A detailed description of the statistical mechanics of the technique was reported by Smith and Frenkel [16].

According to the statistical mechanical relations, the thermodynamic properties of a statistical ensemble can be calculated, if the partition function for that ensemble is available [17]. The Gibbs ensemble partition function for a one-component system at constant temperature  $T$ , total volume  $V$ , and total number of particles  $N$ , in which the system consists of two subsystems with corresponding volumes  $V_I$  and  $V_{II}$  and number of particles  $N_I$  and  $N_{II}$ , is

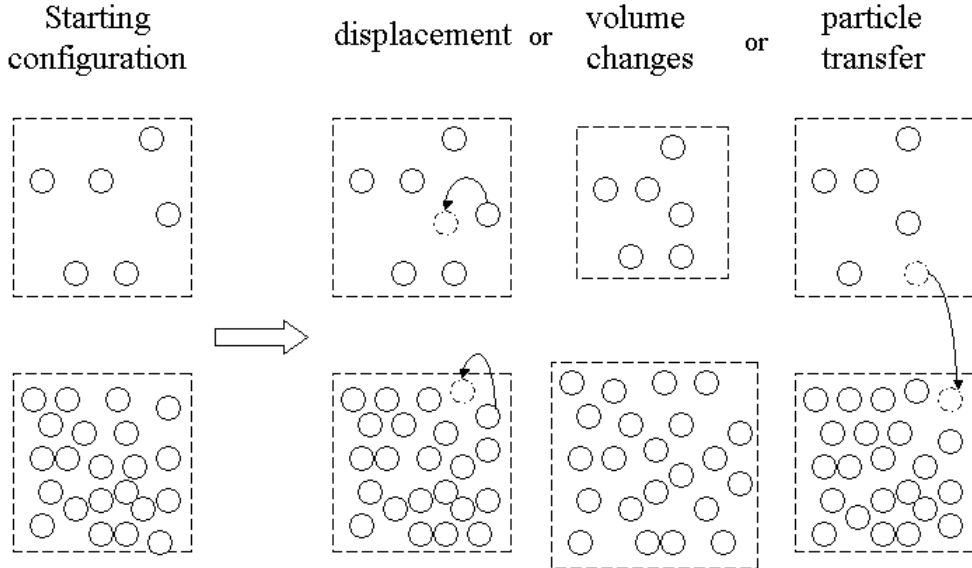


Figure 2.5: Schematic representation of the Gibbs ensemble Monte Carlo simulation technique.

$$Q_{NVT} = \frac{1}{\Lambda^{3N} N!} \sum_{N_I=0}^N \binom{N}{N_I} \int_0^V dV_I V_I^{N_I} V_{II}^{N_{II}} \int d\xi_I^{N_I} \exp\{-\beta U_I(N_I)\} \times \int d\xi_{II}^{N_{II}} \exp\{-\beta U_{II}(N_{II})\}, \quad (2.4)$$

where  $\Lambda$  is the thermal de Broglie wavelength,  $\beta = 1/(k_B T)$ ,  $\xi_I$  and  $\xi_{II}$  are the scaled coordinates of the particles in the first and second regions, respectively,  $U_I$  and  $U_{II}$  are the total energy of the  $N_I$  interacting particles in the first region and  $N_{II}$  interacting particles in the second region, respectively. The corresponding probability density for the partition function of Equation 2.4 is given by

$$\varphi(N_I, V_I; N, V, T) \propto \frac{N!}{N_I!N_{II}!} \exp\{N_I \ln V_I + N_{II} \ln V_{II} - \beta U_I(N_I) - \beta U_{II}(N_{II})\} \quad (2.5)$$

The acceptance criteria for the three type of trial moves can be derived from Equation 2.5,

1. *Particle displacement.*

For this trial move the acceptance criteria is simply

$$\wp_{\text{move}} = \min[1, \exp(-\beta\Delta U)] \quad (2.6)$$

where  $\Delta U$  is the energy difference between new and old configurations due to particle displacement. Equation 2.6 is the familiar acceptance criteria in constant- $NVT$  ensemble.

2. *Volume change.*

During this type of trial move, the volume of region I is increased by  $\Delta V$  at the expense of decreasing the same volume of region II. The probability of acceptance for this trial move is

$$\wp_{\text{volume}} = \min\left[1, \exp\left(-\beta\Delta U_I - \beta\Delta U_{II} + N_I \ln \frac{V_I + \Delta V}{V_I} + N_{II} \ln \frac{V_{II} - \Delta V}{V_{II}}\right)\right] \quad (2.7)$$

3. *Particle transfer.*

The trial move of transferring a particle from region II to region I is accepted by the following criteria

$$\wp_{\text{transfer}} = \min\left[1, \frac{N_{II}V_I}{(N_I + 1)V_{II}} \exp(-\beta\Delta U_I - \beta\Delta U_{II})\right] \quad (2.8)$$

For multicomponent mixtures, the formulations are easily generalized. For such systems, pressure and temperature are fixed in advance and simulations are performed in  $NPT$ -Gibbs ensemble in which the probability density is proportional to

$$\wp(N_I, V_I; N, P, T) \propto \frac{N!}{N_I! N_{II}!} \exp\{N_I \ln V_I + N_{II} \ln V_{II} - \beta U_I(N_I) - \beta U_{II}(N_{II}) - \beta P(V_I + V_{II})\} \quad (2.9)$$

The only change in algorithm is that in  $NPT$ -Gibbs ensemble technique each of simulation regions has its own independent volume changes. Acceptance criteria for three types of trial moves are

1. *Particle displacement.*

The probability for this kind remains the same as Equation 2.6.

2. *Volume change.*

For this type of trial move, the criteria is slightly different from Equation 2.7. The first and second regions have  $\Delta V_I$  and  $\Delta V_{II}$  changes in their volumes, respectively. The trial move is accepted by the following criteria

$$\wp_{\text{volume}} = \min\left[1, \exp\left(-\beta\Delta U_I - \beta\Delta U_{II} + N_I \ln \frac{V_I + \Delta V_I}{V_I} + N_{II} \ln \frac{V_{II} - \Delta V_{II}}{V_{II}} - \beta P(\Delta V_I + \Delta V_{II})\right)\right] \quad (2.10)$$

3. *Particle transfer.*

For multicomponent mixtures, the selection of species must be done with a fixed probability to fulfill the microscopic reversibility. Then the acceptance criteria is the same as Equation 2.11, except for  $N_I$  and  $N_{II}$  being replaced by  $N_{I,j}$  and  $N_{II,j}$  for the  $j$ 'th component, respectively.

## 2.5.2 Chemical potential

A big advantage of the Gibbs ensemble simulations is that the calculations of fluid phase equilibria do not require any knowledge of chemical potentials of components in the system. However, the intrinsic particle creation and annihilation processes in this technique provides a method (like

Widom test particle method in Equation 2.1) for calculation of chemical potentials. The equality of chemical potentials of all components in liquid and gas phases is a useful information to test the convergence of simulations. In this way, the chemical potential of component  $i$  in the region  $I$  for Gibbs ensemble simulation is given by [16]

$$\mu_i = -kT \ln \left\langle \frac{V_I}{N_{I,1} + 1} \exp(-\beta \Delta U_1^\dagger) \right\rangle \quad (2.11)$$

where  $U_1^\dagger$  is the configuration energy to transfer a particle of component  $i$  to the first region.

### 2.5.3 Determination of critical points

Near the critical region, the free energy differences between two phases are small and as a result, Gibbs ensemble simulations become unstable as well as most of other simulation techniques. Under such conditions, finite-size effects are present and results are sensitive to the number of the particles in each region. The finite-size effects in Gibbs ensemble simulation have been studied in details [18, 19, 20]. The following conclusion is taken from [18]: “The lesson seems to be that it may be quite difficult to use GEMC to obtain quantitative information concerning the critical behavior . . .” While such finite-size effects can lead to serious errors in computer simulations of critical point parameters, scaling laws provide a method to estimate the approximate location of critical point using the simulations results far from the critical region. The theoretical basis of this approach is weak; however, the resulting critical points are in good agreement with the results of the more accurate methods. A comprehensive study on fluid critical behavior in computer simulations can be found elsewhere [21].

According to the scaling law, in the case of Gibbs ensemble simulations, the critical temperature is evaluated by fitting the calculated  $\rho - T$  coexistence data [22]

$$\rho_l - \rho_g = b(T_c - T)^\beta \quad (2.12)$$

where  $\beta \approx 0.32$  is the non-classical critical exponent, and  $b$  and the critical temperature  $T_c$  are calculated from the fit. Subsequently, the critical

density  $\rho_c$  can be determined using a fit based on the law of rectilinear diameters [22]

$$\frac{\rho_l + \rho_g}{2} = \rho_c + A(T - T_c) \quad (2.13)$$

where  $A$  and critical density  $\rho_c$  are calculated from the fit.

### 2.5.4 Variations of the technique

A very useful extension of the technique is to combine the semigrand canonical [23] and Gibbs ensemble simulations [20]. The semigrand canonical ensemble technique aims at calculating the phase equilibria for a multicomponent mixture based on changing the identity of different species (rather than insertion-deletion of species) in the system to obtain the convergence.

The schematic representation of the technique is illustrated in Figure 2.6 for a binary mixture. Let us consider that the larger component is  $B$  and the smaller one is  $A$ . According to this algorithm, the smaller component is transferred between two regions via conventional Gibbs ensemble method. For the component  $B$ , particle transfer is not efficient, especially when the differences in the size of the components are high. In such case, changing a component of type  $A$  into one of type  $B$  in one region and a simultaneous reverse change in the other region increases the efficiency of the simulation. This type of trial move is accepted with the following probability

$$\wp_{\text{exchange}} = \min\left[1, \frac{N_{\text{II}}^A N_{\text{I}}^B}{(N_{\text{I}}^A + 1)(N_{\text{II}}^B + 1)} \exp(-\beta\Delta U_{\text{I}} - \beta\Delta U_{\text{II}})\right] \quad (2.14)$$

where  $\Delta U_{\text{I}}$  is the energy difference due to the particle identity exchange of type  $B$  to  $A$  in the first region and  $\Delta U_{\text{II}}$  is the energy difference for the reverse change in the second region.

This algorithm can be generalized to multicomponent systems.

For multisegment molecules (like a  $n$ -alkane), the particle transfer step in the Gibbs ensemble simulation fails due to the large overlap of the molecules. A combination of configurational bias technique and Gibbs



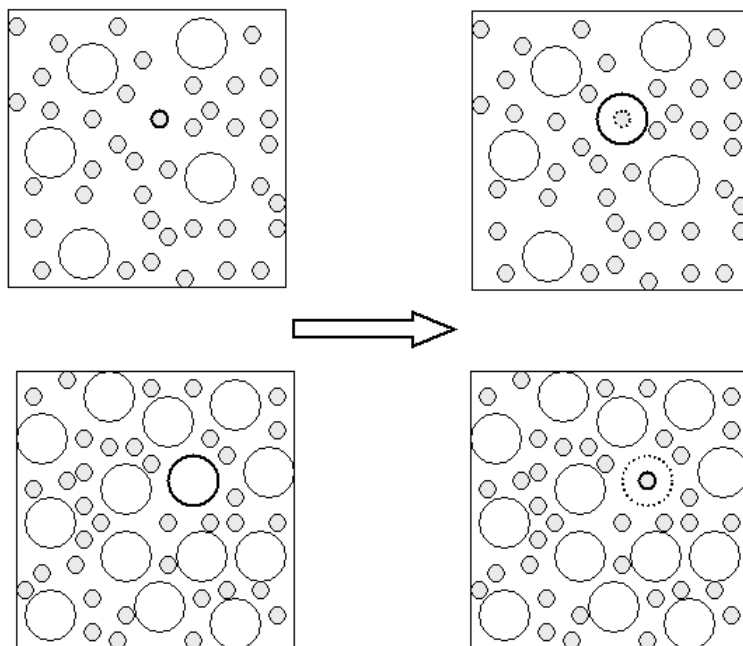


Figure 2.6: Particle identity exchange mechanism.

ensemble method [24] provides a powerful algorithm to improve the particle transfer step for such large orientation-dependent molecules. According to this method, the particle transfer for multisegment molecules are performed in a segment-by-segment mechanism. One molecule is selected randomly and then one segment of the molecule is transferred in a random position into the other box. The next segment is transferred by selecting  $m$  trial directions for growth. The same mechanism is repeated until the last segment has been inserted.



## Chapter 3

# Van der Waals Interactions

### 3.1 Introduction

There are four types of fundamental interactions in nature, strong, electromagnetic, weak, and gravitational. The strong and weak interactions occur between neutrons, protons, electrons and other elementary particles. These two types of forces have short range action ( $\approx 10^{-5}$  nm and smaller). Electromagnetic interactions are forces between charged elementary particles at larger distances ( $\approx 10^{-1}$  nm and larger). Gravitational interactions act between all systems having mass. The ratio of these four types of forces are shown in Table 3.1.

Table 3.1: Four types of fundamental interactions and their ratios.

force	strong	electromagnetic	weak	gravitational
ratio	1	$10^{-3}$	$10^{-15}$	$10^{-40}$

Chemists deal with electromagnetic forces, exclusively. This type of interaction can be divided into two types of forces. Chemical bonds (intramolecular forces) which are usually short-ranged (1-2 Å) and govern the formation of atoms and molecules via covalent bonds, metallic bonds, etc. Physical bonds (intermolecular forces) which are long-ranged ( $> 2$  Å) act between separate particles. While most of the chemical properties (like corrosivity, toxicity, structure, reactivity, etc.) of substances are results of chemical bonds, many physical properties (like boiling point, compressibility etc.) are due to the presence of intermolecular forces. Figure 3.1 shows the classification of intermolecular forces according to the presence of ionic species, polar species and hydrogen atoms bound to oxygen, nitrogen or fluorine atoms (to form hydrogen bonds).

Our basic knowledge of chemical and physical bonds is owed to the development of quantum mechanics in the early decades of the previous century. The quantum mechanical treatment of chemical bonds is inevitable, whereas, development of empirical relations for description of intermolecular forces has rendered help to simplify the statistical thermodynamical relations (like in radial distribution function, virial coefficients, partition functions etc.).

Let us consider a system of  $N$  interacting particles. The total configurational energy for such a system can be calculated by a sum over separate

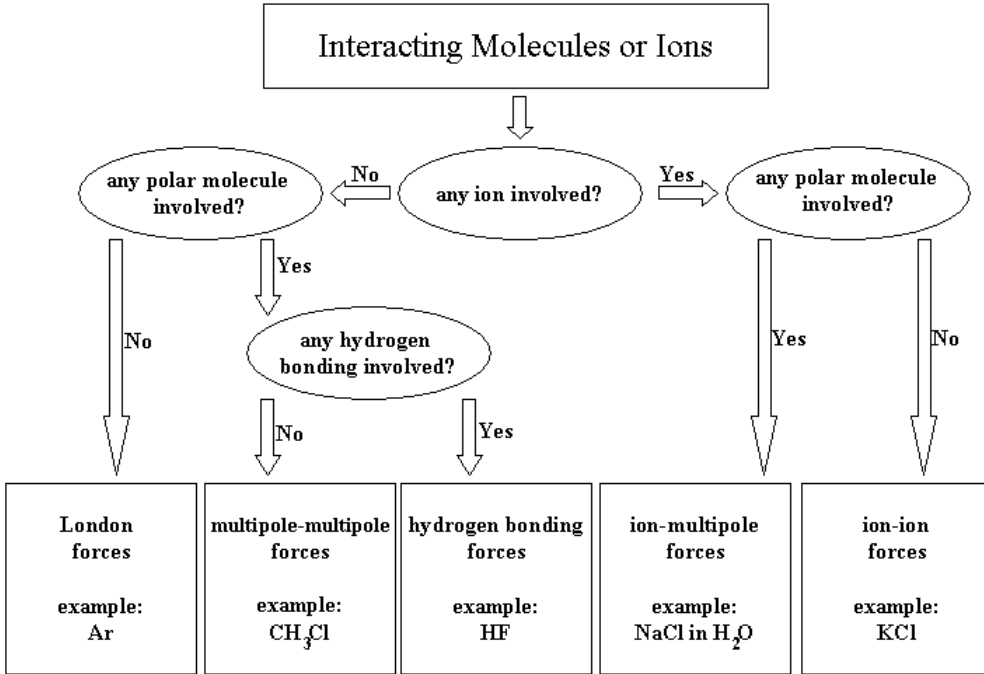


Figure 3.1: Different types of intermolecular forces.

contributions of all possible pairs  $ij$ , all possible triplets  $ijk$ , up to the simultaneous interaction of all  $N$  particles

$$u = \sum_{i < j} \phi_{ij} + \sum_{i < j < k} \Delta\phi_{ijk} + \sum_{i < j < k < l} \Delta\phi_{ijkl} + \dots \quad (3.1)$$

where  $\phi_{ij}$  is the pair interaction energy of particle  $i$  and  $j$  in vacuum,  $\Delta\phi_{ijk}$  is the three-body nonadditivity arising from the changes in interaction potential of pair  $i$  and  $j$  while the third particle is located at  $k$  and so on. These terms are decreasing in magnitude.

$$\sum_{i < j} \phi_{ij} > \sum_{i < j < k} \Delta\phi_{ijk} > \sum_{i < j < k < l} \Delta\phi_{ijkl} > \dots \quad (3.2)$$

The total energy of a system is said to be pairwise additive when only first term in the right hand side of equation 3.1 is nonvanishing. Such an

assumption simplifies the statistical thermodynamical relations, however, it will cause some error at higher densities. For example, nonadditivity contribution to the internal energy of liquid argon at triple point is approximately 5 to 10 percent [1].

As one part of the present work is the *ab initio* calculation of van der Waals forces of noble gases, we restrict ourselves to review van der Waals type of interactions. There are standard books in intermolecular forces for more detailed studies [25, 26]

## 3.2 Empirical models

Quantum mechanical calculations of potential energy surfaces suffer from two major disadvantages. First, such calculations are subject to physical as well as mathematical approximations. Second, they are usually expensive, especially for large molecules and when high accuracy is important. On the other hand, uncertainties of the theoretical approximations can be condensed into few empirical parameters of which the numerical values can be determined from experimental data. All the classical bulk properties which are related to the molecular level interactions can be used. The second virial coefficients provide a source of data to determine the empirical potential parameters and is given by the following expression

$$B_2(T) = -2\pi \int_0^\infty \left[ \exp\left(-\frac{\phi(r)}{k_B T}\right) r^2 dr \right] \quad (3.3)$$

where  $k_B$  denotes Boltzmann's constant,  $T$  is the temperature and  $\phi$  is the pair potential. For light atoms at low temperatures the quantum effects become important and the contributions of these effects on the second virial coefficient must be included [36].

Transport properties, i.e. the viscosity, thermal conductivity and self-diffusion coefficients can be used to determine the empirical potential parameters. While the parameters obtained from this method for weakly anisotropic species are similar to those parameters obtained from the second virial coefficients, there are discrepancies for strongly anisotropic systems [37].

The most commonly used interaction model is the Lennard-Jones (LJ)

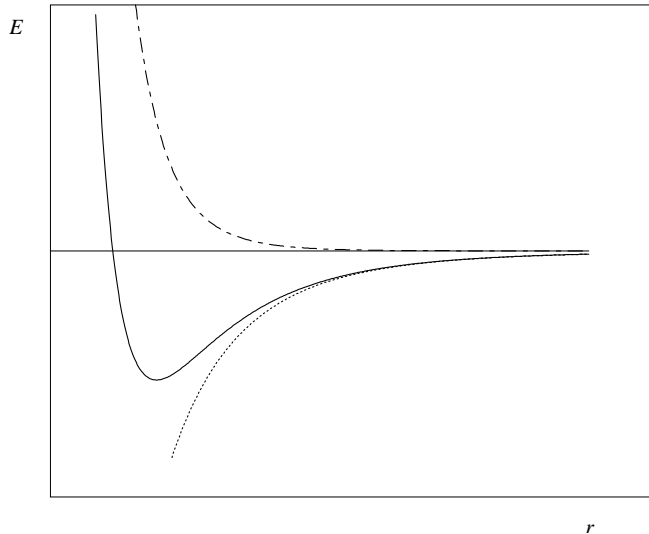


Figure 3.2: Lennard-Jones potential (solid line), the repulsion component (dashed line) and the attraction component (dotted line).

potential, which is given by the expression

$$\phi_{\text{LJ}}(r) = 4\epsilon \left[ \left( \frac{\sigma}{r} \right)^{12} - \left( \frac{\sigma}{r} \right)^6 \right] \quad (3.4)$$

where  $r$  is the distance between two particles,  $\epsilon$  is the well-depth of potential and  $\sigma$  is the distance in which  $\phi_{\text{LJ}}$  is zero. Figure 3.2 shows the LJ potential. This potential comprises both repulsion and attraction parts.

The term  $1/r^{12}$  models the repulsion between particles which is dominating at short distances (dashed line in Figure 3.2). When two particles are brought very close to each other, according to Pauli's principle the electronic clouds surrounding the particles overlap and the energy increases dramatically.

The term  $1/r^6$  constitutes the attraction part which is dominating at large distances (dotted line in Figure 3.2). This term is caused by the van der Waals dispersion forces. The parameters  $\epsilon$  and  $\sigma$  are determined via fitting the experimental data (like second virial coefficient and viscosity).

There is a huge body of simulation studies in a variety of different systems (such as solids, fluids, surfaces, clusters etc.) based on the LJ potential. Regardless of the ability of the LJ potential to model real systems,

Table 3.2: Critical parameters of LJ fluids.

$r_c^*$	$T_c^*$	$\rho_c^*$	Reference
none	$1.316 \pm 0.003$	$0.304 \pm 0.006$	Smith [35]
none	1.310	0.314	Lotfi <i>et al.</i> [7]
5	$1.281 \pm 0.005$	$0.32 \pm 0.01$	Panagiotopoulos [27]
2.5	$1.176 \pm 0.008$	$0.33 \pm 0.01$	Panagiotopoulos [27]
2	$1.061 \pm 0.005$	$0.32 \pm 0.01$	Panagiotopoulos [27]

one can say that this potential is a *standard* model.

Fluid phase equilibria of the LJ fluid has been studied extensively by many different simulation methods. While there is a good agreement between different simulation results for coexistence phases, there are some uncertainties with respect to the exact location of the critical point. Panagiotopoulos [27] reported a comprehensive study for the phase behavior of LJ fluid close to the critical point using Gibbs ensemble simulations for different cutoff radius ( $r_c^*$ ). Table 3.2 shows the results of simulations for critical properties of LJ fluid. Simulation results of Lotfi *et al.* [7] which are based on *NPT* plus test particle method (cf. section 2.3) show good agreement with results of Smith [35]. Both used the full potential in their simulations. Simulation results of Panagiotopoulos [27] show the importance of cutoff radius in determination of critical parameters.

Fluid phase behavior of LJ binary mixtures have been studied [29] with size parameter ratios between 1 and 2, and energy parameter ratios between 1 and 2 using *NPT*-Gibbs ensemble simulation. Lorentz–Berthelot rules were used to calculate unlike parameters. An excellent agreement between simulation results and results of Nicolas *et al.* [30] equation of state was found.

The LJ potential can estimate fairly well the effective pair potential between normal molecules (i.e. non-polar, non-ionic etc.) fluids at normal conditions. However, at extreme conditions the usefulness of the LJ potential is doubtful. For example, in supercritical fluids at very high pressure, the repulsive interaction between molecules is much softer than that given by the LJ potential. It is well known that under such conditions an exp-6 potential provides a more reliable description of intermolecular interactions. The exp-6 potential is given by the following expression



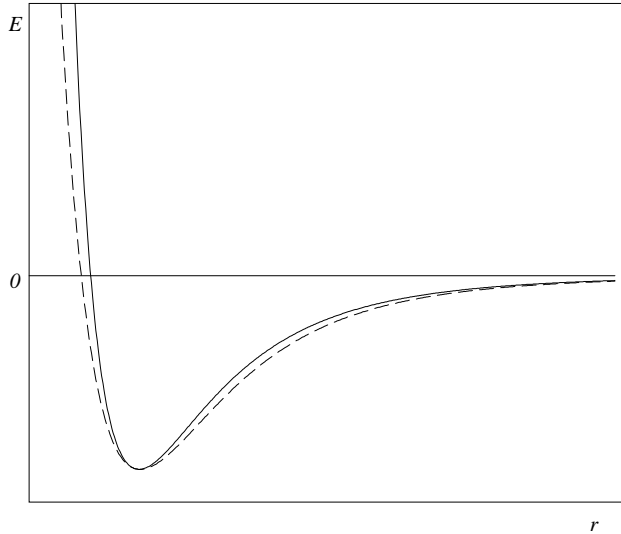


Figure 3.3: Comparison of the exp-6 potential with  $\alpha = 11$  (dash line) with the LJ potential (solid line).

$$\begin{aligned} \phi(r) &= \frac{\epsilon}{1 - \frac{6}{\alpha}} \left\{ \frac{6}{\alpha} \exp \left[ \alpha \left( 1 - \frac{r}{r_m} \right) \right] - \left( \frac{r_m}{r} \right)^6 \right\} & r \geq r_{\max}, \\ &= \infty & r < r_{\max} \end{aligned} \quad (3.5)$$

where  $\epsilon$  determines the depth of the potential minimum which is located at  $r_m$  and  $\alpha$  is the softness of the repulsion. Figure 3.3 compares the exp-6 potential ( $\alpha = 11$ ) with LJ potential.

The repulsive contribution of exp-6 potential is softer than of the LJ potential and this characteristic makes the exp-6 potential a more realistic model for fluids at high pressures. Wu and Sadus [31] reported the Gibbs ensemble simulation of phase equilibria for atomic binary mixtures of noble gases using the LJ and exp-6 potentials. They studied the type III behavior of atomic binary mixtures of noble gases and concluded that exp-6 is a useful potential for such systems. In a more complex case, Errington *et al.* [32] investigated the fluid phase equilibria for the mixtures of water-methane and water-ethane using Gibbs ensemble simulations and exp-6 potential. Their results of simulations show that the exp-6 model is a

reliable potential which can capture the very complex phase behavior of water-ethane mixture at 623 K.

A large number of studies in simulations on a variety of model fluids have been reported. There are relevant references for more detailed studies elsewhere [33, 34].

### 3.3 *Ab initio* calculation of van der Waals forces

While the usefulness of the empirical potentials is evident, there are some limitations on working with them. First, the potential parameters are valid in the range of experiments only. Second, predictions of mixture properties from those of pure species require usually the use of mixing rules which may not be accurate. Third, the potential surface might be highly averaged and does not contain any detailed informations of anisotropy of molecules (like an effective one-dimensional potential curve which is obtained from the second virial coefficient data for molecule–molecule systems [35]).

A combination of quantum mechanics and molecular simulation is possible in the framework of *ab initio* simulation in which at each simulation step, a complete *ab initio* calculation of the energy (or force in molecular dynamics) for the whole configuration of molecules is done. At present, such calculations are performed in *ab initio* molecular dynamics according to the so-called Car-Parrinello method [38]. Such calculations, which are quite time consuming, have been used successfully for the systems including strong intermolecular interactions (like hydrogen bonds [39]). However, this type of calculations fails for complexes interacting with dispersion forces [40].

A simpler way of using *ab initio* calculations in molecular simulations is possible via global simulation [41, 42], in which the potential energy surface between two molecules for sufficient number of configurations is calculated by a standard *ab initio* method and suitable choice of basis sets, then the results are fitted to a proper analytical form and finally used in simulations.

After seminal papers of London [43, 44], four basic components of the van der Waals interaction energies have been known: electrostatic, induction, dispersion, and exchange energies. Since then the general interpreta-

tion of weak interactions has remained the same and most of the studies have been devoted to make this interpretation more rigorous and to find quantitative applications of intermolecular potential surfaces.

In quantum mechanics, there are two approaches to calculate intermolecular interactions: the perturbation approach and the supermolecular approach. While in the perturbation approach, the interaction energy is evaluated using the perturbation theory [45], in supermolecular approach, the interaction energy is calculated as the difference between total energy of complex and the energy of monomers [40]. As the interaction energy is quite small in comparison to the total energy, the supermolecule approach has to be of high accuracy.

### 3.3.1 Perturbation approach

According to the Rayleigh-Schrödinger perturbation theory (RSPT) to the intermolecular interaction, the total Hamiltonian of a system of two molecules,  $a$  and  $b$ , is decomposed into

$$\begin{aligned} H &= H^0 + V \\ H^0 &= H_a + H_b \end{aligned} \quad (3.6)$$

where  $H_a$  and  $H_b$  denote the Hamiltonians of  $a$  and  $b$ , respectively and  $V$  denotes the intermolecular interaction terms. We assume that  $\phi(A)$  and  $\epsilon(A)$  are the eigenfunction and eigenvalue of Hamiltonian  $H_a$ , respectively and the same notation will be used for molecule  $b$ . The total energy  $E^{ab}$  of the complex is then given by

$$E^{ab} = \underbrace{\epsilon(A) + \epsilon(B)}_{E^{(0)}} + \sum_{i=1} E^{(i)} \quad (3.7)$$

where  $E^{(0)}$  is the sum of the unperturbed energies of the monomers and  $E^{(i)}$  are corrections contributions to the energy.

The wavefunction of the form  $\phi(A)\phi(B)$  does not satisfy the antisymmetric condition with respect to the exchange of electrons of  $A$  and  $B$ . This assumption does not disturb reproducing the long-range contribution

of the interaction energy, however, it fails to show the exchange effects [47]. The electrostatic (Coulomb) interaction energy is a first-order energy correction of equation 3.7

$$E_{\text{elstat}}^{(1)} = \langle \phi(A)\phi(B) | V | \phi(A)\phi(B) \rangle \quad (3.8)$$

The second-order energy corrections yield the induction and dispersion terms

$$E^{(2)} = \underbrace{E_{\text{ind}}^{(2)}(a \rightarrow b) + E_{\text{ind}}^{(2)}(b \rightarrow a)}_{E_{\text{ind}}^{(2)}} + E_{\text{disp}}^{(2)} \quad (3.9)$$

where

$$E_{\text{ind}}^{(2)}(a \rightarrow b) = - \sum_{B' \neq B} \frac{|\langle \phi(A)\phi(B) | V | \phi(A)\phi(B') \rangle|^2}{\Delta\epsilon(B')} \quad (3.10)$$

$$E_{\text{disp}}^{(2)} = - \sum_{B' \neq B} \sum_{A' \neq A} \frac{|\langle \phi(A)\phi(B) | V | \phi(A')\phi(B') \rangle|^2}{\Delta\epsilon(A') + \Delta\epsilon(B')} \quad (3.11)$$

an expression is obtained from equation 3.10 for  $E_{\text{ind}}^{(2)}(b \rightarrow a)$  by interchanging A and B. In these formulas,  $\phi(A')$  and  $\phi(B')$  are the wavefunctions for the first excited state of molecule  $a$  and  $b$ , respectively,  $\Delta\epsilon(A')$  and  $\Delta\epsilon(B')$  are the excitation energies for transition  $A \rightarrow A'$  in molecule  $a$  and  $B \rightarrow B'$  in molecule  $b$ , respectively.

As we wish to calculate the intermolecular interaction energy function in terms of the physical properties of monomers (like intermolecular distances, orientations of molecules, permanent multipole moments and ...), the potential interaction  $V$  is expanded into of spherical harmonics [36]. The electrostatic term in equation 3.8 comprises the interactions between the permanent multipole moments of monomers. The interaction energy between permanent and induced multipole moments is given by the induction energy in equation 3.10. This kind of interaction can be expressed as

the monomer multipole moment and polarizabilities. The dispersion energy arises from the interaction between instantaneous multipole moments and can be expressed as monomer dynamic polarizabilities [48].

The multipole expansion of the different contributions to the energy may be written in a general form

$$E = \sum_{m=k} C_m X_m R^{-m} \quad (3.12)$$

where  $k$  depends on the particular interaction contribution,  $C_m$  are  $R$ -independent which are calculated from the properties of the isolated monomers, and  $X_m$  are coefficients which depend on mutual orientation of molecule  $a$  and  $b$ . Equation 3.12 is valid for large values of  $R$ , but fails to describe the interaction potential at finite  $R$ .

RSPT has been successful to calculate the long-range part of the intermolecular interaction. Many efforts have been made to circumvent the exchange problem in perturbation theory.

At the self-consistent field (SCF) level of theory, which provides a fairly good approximation of wave functions, it is possible to include the second perturbation term,  $W$ , which accounts for the fluctuation potentials of the monomers. For the case of intermolecular interaction Hamiltonian of the system has the form

$$H = F^0 + W + V \quad (3.13)$$

where  $F^0$  is a sum over the monomer Fock operators. For this equation, the total energy of the complex can be expressed as [49]

$$E^{ab} = \sum_{i=0} \sum_{j=0} E^{(ij)} \quad (3.14)$$

With this formalism it is possible to include the exchange effects [50].

The problem of the exchange effects in perturbation theory has been solved in the framework of SAPT by introducing an antisymmetrizer operator which changes the symmetry of the wavefunctions. According to this theory the first-order energy is given by

$$E_{\text{SAPT}}^{(1)} = \frac{\langle \phi(A)\phi(B) | V \mathcal{A} | \phi(A)\phi(B) \rangle}{\langle \phi(A)\phi(B) | \mathcal{A} | \phi(A)\phi(B) \rangle} \quad (3.15)$$

where  $\mathcal{A}$  is the total antisymmetrizer for the complex. While equation 3.15 uses the  $\phi(A)\phi(B)$  (which does not satisfy the antisymmetric condition of the wave function), it includes the electrostatic interaction as well as the exchange repulsion energy. Exchange induction and dispersion can be calculated using higher order terms [51].

### 3.3.2 Supermolecular approach

The supermolecular approach uses the following relation to calculate the interaction energy

$$\Delta E = E^{ab} - (\epsilon(A) + \epsilon(B)) \quad (3.16)$$

This approach has some benefits over the perturbation theories:

- The convergence problems are avoided.
- Any *ab initio* method can be used to estimate the energies.
- The intermolecular interaction hypersurface is treated uniformly.

However, there are some flaws attached to the supermolecular approach. First of all, the approach has to be methodological consistent, which means that both the monomer and the complex must be treated at the same level of theory. Even so, the numerical consistency problem is not avoided. This drawback arises from the fact that in the calculations of the dimer energy, the individual monomers take advantage of the basis set of the whole complex rather than their own ones. This problem is called basis set superposition error (BSSE). The other limitation of the supermolecular approach is that equation 3.16 yields only a single number and that physical decomposition of the interaction potential is difficult especially at the correlated level [52].

There are three major methods in supermolecular approach to account for the exchange effects: configuration interaction (CI) methods, Möller–Plesset perturbation (MP) methods and coupled-cluster (CC) methods.

The full CI method (FCI) uses a wave function with all possible electron excitations and hence grows combinatorially

$$\phi_{\text{FCI}} = \phi_0 + \sum_{i,a} C_i^a \phi_i^a + \sum_{\substack{i,a \\ j,b}} C_{i,j}^{a,b} \phi_{i,j}^{a,b} + \dots \quad (3.17)$$

where  $\phi_0$  is the wave function of the ground state and the next terms represent the wave functions of the electronic excitations. FCI yields the exact solution to the electronic Schrödinger equation; however, its evaluation is feasible for small molecules with modest basis sets only. For larger molecules and basis sets, the FCI expansion of equation 3.17 is truncated to include only a certain number of important excitations. The most commonly used truncated CI is CI singles and doubles (CISD) which uses only the first three terms in above expansion.

Like CI, the coupled-cluster method is based on the wave function expansion; however, the CC wave function is written in an exponential form

$$\begin{aligned} \phi_{\text{CC}} &= \exp(T)\phi_0 = (1 + T + T^2/2! + T^3/3! + \dots)\phi_0 \\ T &= T_1 + T_2 + T_3 + \dots \end{aligned} \quad (3.18)$$

where  $T_i$  is an operator generating all  $i$ -fold electron excitations. The CC wave function can be truncated on the basis of the maximum excitations, like CI method. From these truncations different methods of CC are generated like CCD, CCSD, etc.

### 3.3.3 Basis set

There are two main problems with respect to the basis sets in *ab initio* calculations of intermolecular forces. First, there is no universal basis set for all applications, but the choice of the basis sets is highly dependent on the chemical constitution of the interacting species. For example, in hydrogen-bonded complexes, the major contribution to the interaction energy is the electrostatic energy, which requires a proper description of

the lowest multipole moments, while in a dimer of rare gases the dispersion term is the major attractive contribution, which is usually difficult to reproduce since it is due to correlation effects only.

Second, the problem of BSSE in the supermolecule approach causes a serious error in calculation of intermolecular interactions. The usual way to correct for BSSE is based on a method proposed by Boys and Bernardi [55], which is called counterpoise (CP) scheme. According to this method, the corrected interaction energy of equation 3.16 can be defined as

$$\Delta E^{\text{CP}} = E^{ab} - (\epsilon^a(AB) + \epsilon^b(AB)) \quad (3.19)$$

where  $\epsilon^a(AB)$  and  $\epsilon^b(AB)$  are the energies of the monomers calculated by the whole supermolecular basis sets.

The size of the basis sets is affected by the accuracy needs for the property under study. On the other hand, by choosing the larger basis sets, the computational costs increase rapidly. A compromise between the size of the basis sets and computational costs is up necessary. By increasing the capabilities of computers, it is possible to calculate the intermolecular interactions with larger basis sets and higher accuracy. Woon [53] showed that the MP4 level of theory and *aug-cc-pVQZ* basis set give the excellent result for noble gas dimers. Cybulski and Toczyłowski [54] reported *ab initio* potentials for helium, neon, argon and their binary cross interactions using the CCSD(T) level of theory and several correlation consistent basis sets. The accuracy of their results are comparable with the empirical potentials and in some cases even more reliable.

### 3.3.4 Many-body interactions

Many studies in simulations that have been reported so far are based on the assumption of pairwise additivity, however, in the study of dense fluids and solids, higher order terms in the series of equation 3.1 become important. An exact examination of higher order terms demands highly accurate experimental as well as theoretical methods.

Several experimental techniques have been used to study many-body effects, like measurements of crystal structures [56] and virial coefficients [36]. During the last decade, the spectroscopy of van der Waals molecules has become a very important tool in the study of many-body effects [57].



In the examination of many-body forces, quantum-mechanical calculations have been applied since the 1940s when Axilrod and Teller [58] used the third order perturbation theory to calculate the three-body triple-dipole dispersion energy for spherical atoms

$$E_{\text{AT}} = \nu \frac{1 + 3 \cos \alpha \cos \beta \cos \gamma}{R_{12}^3 R_{23}^3 R_{31}^3} \quad (3.20)$$

where  $\nu$  is the non-additivity coefficient which can be calculated based on the properties of the monomers ( $\nu \approx 9/16Va^3$  in which  $V$  and  $a$  are the atomic ionization potential and polarizability, respectively);  $R_{12}$ ,  $R_{23}$ , and  $R_{31}$  are the length of the sides; and  $\alpha$ ,  $\beta$  and  $\gamma$  are the angles of the triangle formed by the monomers. The evaluation of the angular part of the above relation reveals that  $E_{\text{AT}}$  is negative for collinear geometries while it is positive for equilateral triangle geometries. After the leading work of Axilrod and Teller, in 1970 Bell [59] generalized the long-range nonadditivity third-order interactions in a series in which the AT expression of equation 3.20 is the first term

$$E_{\text{three-body}} = E_{\text{AT}} + E_{\text{DDQ}} + (E_{\text{DQQ}} + E_{\text{DDO}}) + \dots \quad (3.21)$$

where  $D$ ,  $Q$ , and  $O$  represent dipole, quadrupole, and octopole moments, respectively. Many studies have been devoted to evaluate the importance of different terms in above equation [60].

A comprehensive investigation of complete *ab initio* treatment of three-body nonadditivity has been tractable by recent developments in SAPT framework [61]. This theory provides a detailed study in decomposition of three-body nonadditivity to the different short-range and long-range contributions. In a recent study, Bukowski and Szalewicz [62] analyzed the average contributions of various components of three-body nonadditivity to the thermodynamic properties of fluid argon using the Gibbs ensemble simulation. They showed that cancellations between different contributions make the resulting three-body interaction very close to the Axilrod-Teller triple-dipole potential.

### 3.3.5 Extrapolation and fitting the potential surfaces

Many attempts have been made to compute the interaction energies of weakly bound molecular complexes at the basis set limit using correlation-consistent basis sets and an extrapolation scheme [63, 64, 65]. The method is based on the extrapolation of the interaction energies by a proper formula in terms of the cardinal number  $X$  of the correlation-consistent basis set aug-cc-pVXZ (with  $X=D(2)$ ,  $T(3)$ ,  $Q(4)$ ,  $5$ ,  $6$ ). The exponential formula have been used exclusively [66, 67, 68]

$$E(X) = E(\infty) + A \exp(-BX) \quad (3.22)$$

where  $E(X)$  is the energy (Hartree-Fock or correlation or total) with the basis set of cardinal number  $X$ , and  $E(\infty)$  is the energy of complete basis set limit. The recent investigations showed that the exponential formula 3.22 decays too quickly, and accordingly, several new extrapolation schemes have been suggested, which usually use a simple polynomial form of  $1/X$  [69, 70]. Among all, the extrapolation of successive correlation-consistent energies with basis set cardinal number  $X$  has been shown to be quite effective in calculation of the basis set limit energies [71]. It is known that the energies obey the law

$$E(X) = E(\infty) + A/X^3 \quad (3.23)$$

The formula is valid for larger basis sets such as aug-cc-pVQZ and -pV5Z; for the smaller basis sets the extrapolation formula 3.23 should be modified [72].

The *ab initio* calculations of PES are usually performed for a finite number of configurations. Many applications (such as in statistical thermodynamics, simulations etc.), require that these PES are expressed with a suitable mathematical representation. The most common methods involve least-square fitting to an analytical form, which is the usual technique for simple one-dimensional PES. However, for multi-dimensional PES, more sophisticated schemes involving complex functional forms are needed. A recent review is available elsewhere [73].

For the simple case of one-dimensional PES, it is convenient to use an analytical form which consists of a repulsion part, an attraction part,

and a damping function to attenuate the long-range asymptotic term(s) at small distances. For example, Koronal *et al.* [74] used an analytical representation for helium dimers which includes a repulsive exponential component and an attractive damped dispersion component of the form

$$\phi(R) = Ae^{-\alpha R + \beta R^2} + \sum_{n=3}^8 f_{2n}(R, b) \frac{C_{2n}}{R^{2n}} \quad (3.24)$$

where  $A$ ,  $\alpha$ ,  $\beta$  and  $b$  denote adjustable parameters,  $C_{2n}$  denotes a dispersion coefficient, and  $f_{2n}$  is the damping function of Tang and Toennies [75]

$$f_{2n}(R, b) = 1 - e^{-bR} \sum_{k=0}^{2n} \frac{(bR)^k}{k!} \quad (3.25)$$



# Chapter 4

## The gemc Program

## 4.1 Introduction

In the present work, fluid phase equilibria for pure neon, argon, krypton and binary mixtures neon–argon and argon–krypton were calculated based on the GEMC simulations and *ab initio* potentials. For pure and binary mixture fluids, new computer codes according to the standard Gibbs ensemble simulation algorithms were developed. In this chapter, the details of these new codes are presented.

## 4.2 The program gemc

The program `gemc` (which stands for Gibbs ensemble Monte Carlo) were developed in C programming language according to the *NVT*-Gibbs ensemble algorithm for pure fluids and the *NPT*-Gibbs ensemble algorithm for the fluid mixtures. Figure 4.1 shows the schematic representation of the `gemc` program.

### 4.2.1 Initialization

In this part of the program, the initial positions of the particles in each region are randomly generated, and also any value which is used in the next steps (such as the number of the particles in each box, parameters of the interaction potentials, the initial densities of each box, etc.) are assigned to different variables of a structure, namely `box`. The initialization is performed by the very first function of the program, namely `opening_function()`. The initial densities are chosen so that, after equilibrium, there is a reasonable number of particles in both regions. Some trial and error may be required to find the proper initial states.

### 4.2.2 The `main()` function

In this part of the program, the three types of the Monte Carlo moves are performed, with fixed probabilities. The relative ratio of the three types of moves depends on the thermodynamic conditions of the state point. The ratio is set to give the best simulation efficiency. Before performing any trial move, the total energy and virial of the system are cal-

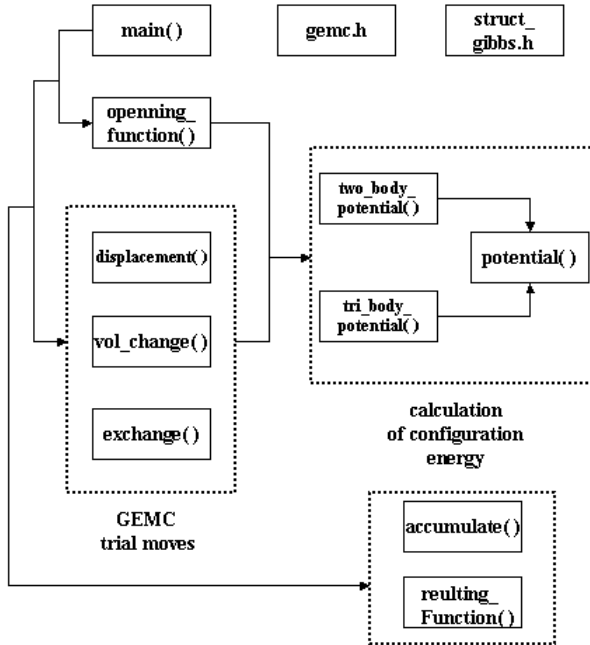


Figure 4.1: Schematic representation of the `gemc` program.

culated by invoking the `two_body_potential()`, `tri_body_potential()`, and `cutoff_corrector()` functions. These functions calculate respectively the total energy of two-body, three-body contributions and the cutoff corrections of potentials using the standard relations [15].

A selection of a trial move is done randomly, and a proper function is invoked afterwards:

The particle displacements are performed using the `displacement()` function. The choices of the box, particle index, particle species (for mixtures), and new position of particles are made randomly. The maximum displacement of the particles are adjusted to give acceptance ratios of about 50%.

The volume rearrangements are implemented by calling the `vol_change()` function. The choice of the box to be altered is made randomly and the maximum changes in volume are tuned to give almost 40% of the accep-

tance ratios.

The function `exchange()` is applied to transfer the particles between two simulation boxes. Selections of the box, particle species (for mixtures), and particle index are done randomly. By any particle insertion attempt, function `mu()` is invoked to calculate the chemical potential according to the Widom test particle method (cf. section 2.5).

After each Monte Carlo step, function `accumulate()` is called to evaluate the accumulates of the thermodynamic properties (like energy, enthalpy, pressure ...). A function namely, `resulting_function()` has been devised to report the results of the simulations after a predefined number of Monte Carlo steps.

### 4.2.3 Analysis of results

After the system has reached equilibrium, the accumulated properties are collected into several files. After a successful simulations, a program (`mean` for pure systems and `st_dev_mix` for mixtures) is used to calculate the mean and standard deviations of the resulting data. The program is set to read the M number of data from each input file and divide them into N blocks, the algebraic mean of each block is calculated and finally the standard deviations of the block averages are estimated.

## 4.3 Simulation details

### 4.3.1 Pure fluids

Standard *NVT*-Gibbs ensemble simulations were used to calculate the fluid phase properties of pure neon, argon, and krypton. Simulations were performed with two-body and two-body plus AT three-body potentials in 5000 cycles to achieve the equilibrium and further 5000 cycles were used to collect the averages. Total number of 500 atoms were used in simulations with the standard periodic boundary conditions and minimum image convention. The cutoff ratio for the two-body potential was equal to the half of the box length, and the long-range corrections were computed according to the standard relations [15]. The cutoff ratio for the three-body potential was set to the quarter of the box length.



### 4.3.2 Binary mixture fluids

Standard *NPT*-Gibbs ensemble simulations were applied to obtain the fluid phase equilibria for neon–argon and argon–krypton binary mixtures. Simulations were performed with two-body for the total number of 900 atoms and two-body plus AT three-body potentials for the total number of 600 atoms. To achieve the equilibrium conditions, 10000 Monte Carlo cycles were used and additional 5000 cycles were used to calculate the averages. Standard periodic boundary conditions and the minimum image convention were applied. The two-body and three-body potential cutoff corrections were treated like in the case of pure fluids.



# Chapter 5

## Results and discussion

## 5.1 Neon

### 5.1.1 Potentials

A comprehensive study is reported on the calculations of fluid phase equilibria for pure neon based on the GEMC simulations using two-body *ab initio* potentials, two-body plus AT three-body potentials, and also an equation of state with and without quantum corrections. For the *ab initio* potentials, the available data in the literature were used. Cybulski and Toczyłowski [54] reported *ab initio* potential energy curves for three homonuclear (He–He, Ne–Ne, Ar–Ar) and three heteronuclear (He–Ne, He–Ar, Ne–Ar) rare gas dimers using the CCSD(T) level of theory and several correlation consistent basis sets. In the present work, results of the aug-cc-pVQZ (avqz) and aug-cc-pV5Z (av5z) basis sets were used to obtain the basis set limit (av45z) of the interaction energies according to the  $1/X^3$  method (cf. section 3.3.5). The *ab initio* potentials resulting from the avtz+(332) (denoting aug-cc-pVTZ+(3s3p2d)), av5z, and av45z basis sets which were used in simulations are given in Table A.1. The potentials are plotted in Figure 5.1 and compared with empirical potential of Aziz and Slaman [77]. It can be seen that the av5z potential is more repulsive at the repulsive wall and less attractive at about well depth and dispersion parts than the empirical potential, while the agreement of the av45z potential is very good in the whole range of attractive and repulsive regions. The quality of the avtz+(332) potential lies between other two *ab initio* potentials.

Table 5.1: Characteristic properties of the neon–neon potentials.

Property	avtz+(332) [54]	av5z [54]	av45z This work	Grochola <i>et al.</i> [78]	Aziz and Slaman [77]
$R_e$ (Å)	3.114	3.125	3.097	3.131	3.091
$\epsilon$ ( $\mu E_h$ )	125.83	117.51	130.95	122.34	133.80

Grochola *et al.* [78] developed another *ab initio* potential for neon dimer using the MP4(SDTQ) level of theory and Gaussian atomic basis sets. For the sake of comparison, Table 5.1 collects the well depth,  $\epsilon$ , and well

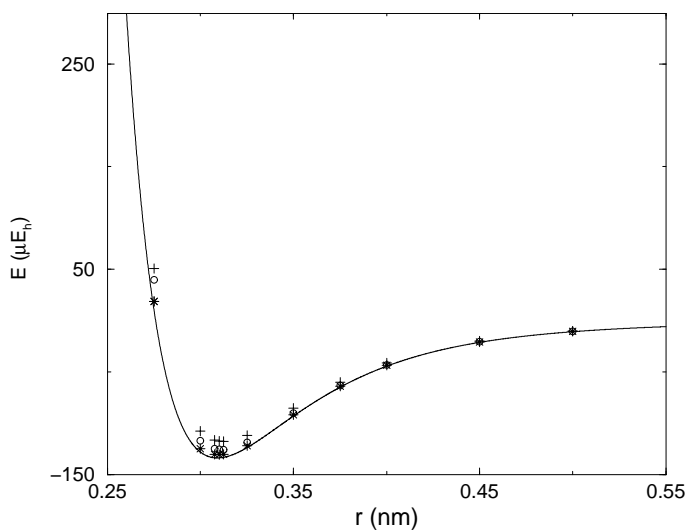


Figure 5.1: Potential energy surface of the neon dimer: the av5z potential [54] (+); the avtz+(332) potential [54] (o); the av45z potential (this work) (\*); the empirical potential of Aziz and Slaman [77] (solid line).

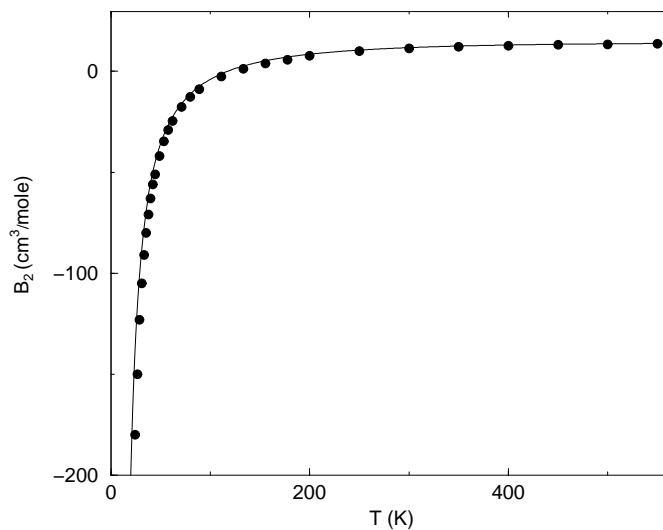


Figure 5.2: Second virial coefficients of neon: calculations with the av45z *ab initio* potential (solid line); experiment [78] ( $\bullet$ ).

position,  $R_e$ , for the avtz+(332), av5z, and av45z potentials and compares them with the corresponding values for empirical potential and another *ab initio* potential for neon.

A comparison of the characteristic properties of the potentials in Table 5.1 reveals that the location of the well position,  $R_e$ , for the av45z potential is almost exact and the value of well depth is only about 2.13% less than the corresponding value for the empirical potential. The MP4 potential has a well depth 8.5% less than empirical value and the position of  $R_e$  is shifted about 1.29% toward higher interatomic distances. The quality of avtz+(332) potential is better than MP4 potential (for the avtz+(332) potential,  $R_e$  and  $\epsilon$  are 0.74% and 5.96% less than corresponding values for the empirical potential). The well depth of the av5z potential is the worst in this series of *ab initio* potentials: it amounts to only 87.83% of the experimental well depth, while the well position is 1.10% less than the empirical value, it is still better than the well position for MP4 potential.

The above comparison between different *ab initio* potentials (especially between av5z and av45z potentials) shows that the extrapolation scheme of  $1/X^3$  provides a powerful method to develop high quality potentials from successive correlation consistent basis sets.

The mathematical representation of equation 3.24 was used to fit the *ab initio* potential surfaces resulting from the av45z, av5z, and avtz+(332) basis sets. The fitting parameters are given in Table A.2. Figure 5.1 represents the different *ab initio* potentials.

A two-body potential should predict the second virial coefficients according to the equation 3.3. It can be seen in Figure 5.2 that the calculated second virial coefficients based on the av45z potential are in good agreement with experiments [78] except for very low temperatures where quantum corrections must be included [36].

In the simulations including AT potential, the three-body nonadditivity coefficient was set to 12.02 Hartree (Bohr)<sup>9</sup> for neon [79].

### 5.1.2 Simulations

The details of simulations were given in section 4.3. Simulations were performed along the vapor pressure curve from just above the triple point up to near the critical region. For the av45z and avtz+(332) potentials, simulations were performed with two-body, and two-body plus AT poten-

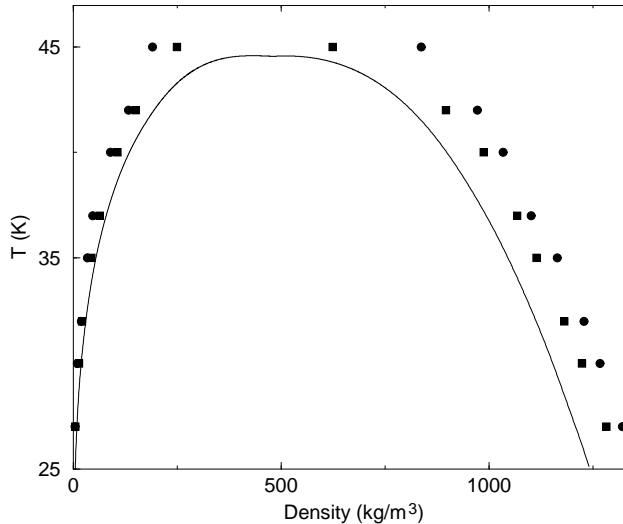


Figure 5.3: Comparison of densities of the coexisting phases for neon: GEMC simulation results with the av45z potential ( $\bullet$ ); GEMC simulation results with the avtz+(332) potential ( $\blacksquare$ ); experiments [93] (solid line).

tials, while the simulations for the av5z potential were performed only with two-body potentials. The results are given in Tables A.3 to A.7 for the simulations with the av45z, av45z plus AT, avtz+(332), avtz+(332) plus AT, and av5z potentials, respectively. The simulation results for the densities of coexisting phases resulting from the two-body *ab initio* potentials (av45z and avtz+(332)) are given in Figure 5.3 and compared with experimental data [93]. The results of the same simulations for the vapor pressure are given in Figure 5.4. Figure 5.5 shows the simulation results for the two-body potentials (av45z and avtz+(332)) plus AT, simulation results for av5z potential, and experiments [93]. The results for the vapor pressure of the same simulations are given in Figure 5.6.

The critical parameters were calculated using the relations 2.12 and 2.13. Table 5.2 collects the critical temperatures and densities for the avtz+(332) plus AT, av5z plus AT, av45z potentials, and experiment [89].

It can be seen in Figures 5.5 and 5.6 that the inclusion of AT potential to the energy improves the simulation results of av45z potential. However, there are still large discrepancies between the simulation results and experimental data. The predicted critical temperature (46.10 K) and

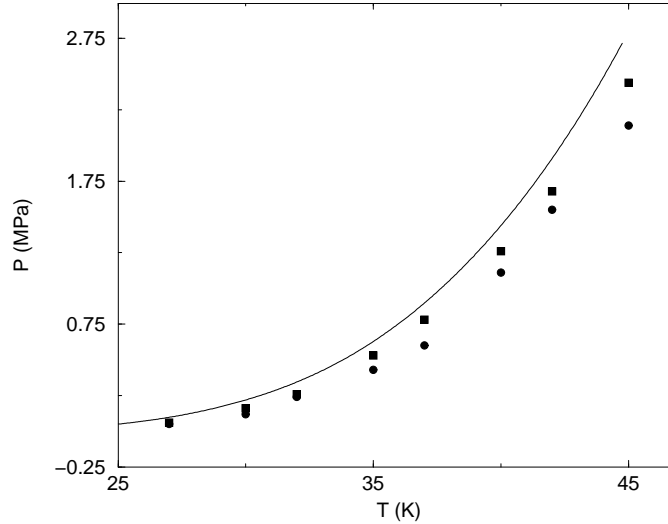


Figure 5.4: Comparison of the vapor pressures for neon: GEMC simulation results with the av45z potential ( $\bullet$ ); GEMC simulation results with the avtz+(332) potential ( $\blacksquare$ ); experiments [93] (solid line).

density ( $493.6 \text{ kg/m}^3$ ) for the av45z plus AT potentials are too large by 3.62% and 2.43% with respect to the corresponding experimental values. The simulation results of the avtz+(332) basis set plus AT potentials are quite satisfactory in the gaseous branch; the vapor pressure, and also the predicted critical parameters are in excellent agreement with experiments, but there are still discrepancies in the liquid branch. The predicted critical temperature and density by the same simulations are only 0.25% and 0.58% above the experimental values, respectively. On the other hand, the simulation results of the av5z potential show a fairly good agreement with experiments at low temperatures, and the potential is a good effec-

Table 5.2: Critical properties for neon.

Parameter	avtz+(332) plus AT	av5z	av45z plus AT	experiment
$T_c$ (K)	44.60	41.98	46.10	44.49
$\rho_c$ ( $\text{kg/m}^3$ )	484.7	492.1	493.6	481.9



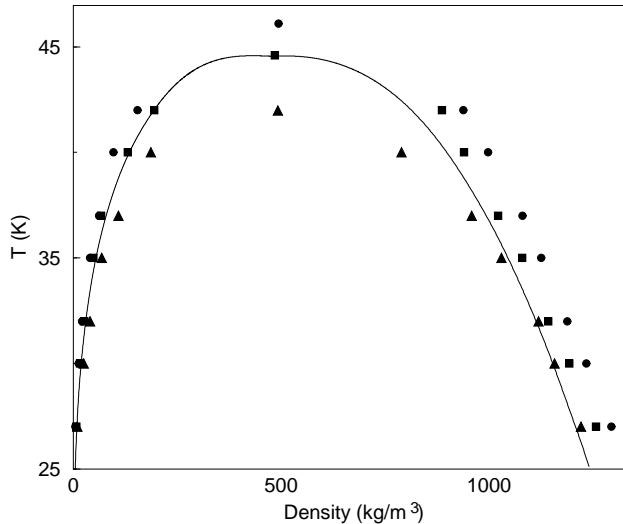


Figure 5.5: Comparison of densities of coexisting phases for neon: GEMC simulation results with the av45z plus AT potentials (●); GEMC simulation results with the avtz+(332) plus AT potentials (■); GEMC simulation results with the av5z potential (▲); experiments [93] (solid line).

tive two-body potential for this region. However, the agreement at higher temperatures and also the predicted critical properties are poor.

None of the models was able to calculate the fluid phase equilibria for neon with sufficient accuracy, in the present work. Leonhard and Deiters [42] developed an *ab initio* potential using the MP4 level and correlation consistent basis sets. They used the resulting *ab initio* potentials with and without AT potentials in the GEMC simulations of neon. An excellent agreement with experiment was reported in the complete range of temperatures from just slightly above the triple point up to near the critical region showing that the quantum effects in the fluid phase properties of neon are negligible.

It has been shown that neon is a near-classical system which shows non-negligible quantum effects at low temperatures [80]. Different approaches have been applied in computer simulations to calculate quantum effects, like path-integral Monte Carlo [81], semiclassical simulations based on the Wigner–Kirkwood asymptotic expansion in powers of  $\hbar$  (where  $\hbar = h/2\pi$  and  $h$  is Planck’s constant) [82] etc. Alternatively, in the present work, an

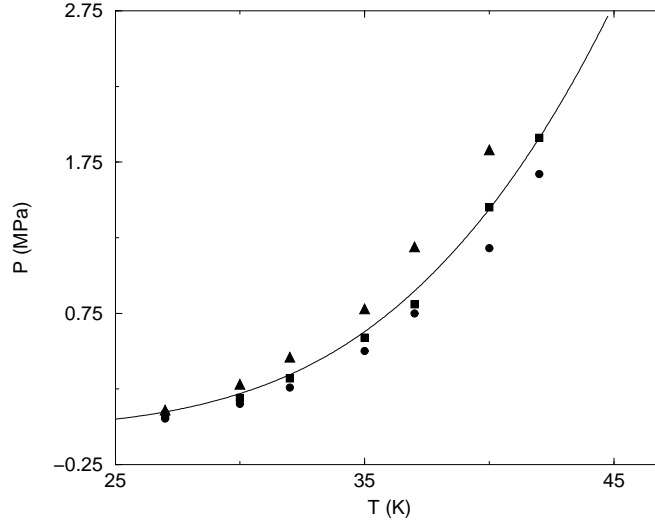


Figure 5.6: Comparison of the vapor pressure for neon: GEMC simulation results with the av45z plus AT potentials ( $\bullet$ ); GEMC simulation results with the avtz+(332) plus AT potentials ( $\blacksquare$ ); GEMC simulation results with the av5z potential ( $\blacktriangle$ ); experiments [93] (solid line).

equation of state and a newly developed correction function were used to show that the discrepancies in our simulation results of neon are mainly due to the quantum effects.

### 5.1.3 Quantum corrections

In quantum fluids, the assumption of continuity of energy levels is no longer valid. The discontinuity occurs at low temperatures and high densities for systems containing light atoms or molecules.

A cubic cell model [83] has been developed to estimate the quantum effects in fluids. The model is based on the assumption that each molecule is restricted to a cubic cell formed by its neighbors, with a size depending on the free volume. The model can be applied to any van der Waals type equation of state, which can be separated into a repulsion part ( $p_{\text{rep}}$ ) and an attraction ( $p_{\text{att}}$ ) part

$$p = p_{\text{rep}} + p_{\text{att}} \quad (5.1)$$

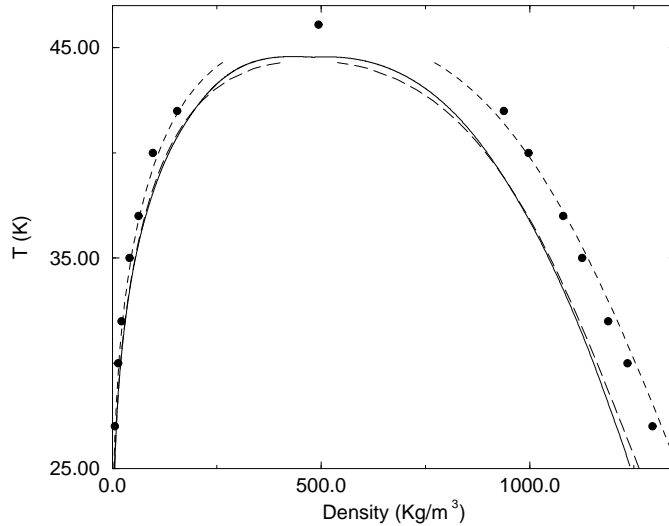


Figure 5.7: Comparison of densities of the coexisting phases for neon: GEMC simulation results with the av45z plus AT potentials ( $\bullet$ ); the Deiters equation of state (dashed line); the Deiters equation of state with quantum corrections (long dashed line); experiment [93] (solid line).

The cubic cell model can predict the quantum effects fairly well at high densities, however, the corrections for low densities are overestimated. Recently, a new cell model was developed for the estimation of quantum effects in fluids, namely the “spherical cell model” [84]. The model is more realistic and can be applied to any van der Waals type equation of state which satisfies equation 5.1. A correction function was applied to correct the overestimations of quantum corrections at low densities and high temperatures.

Deiters [85,86,87] proposed a three-parameter van der Waals type equation of state for square-well fluids by deriving a semiempirical approximation of the radial distribution function, including corrections for molecular shape, soft repulsive potential, and three-body effects. The empirical parameters are determined from critical properties. The equation has the ability of reproducing the  $PVT$  data in a very large range of pressures. While the results for the large noble gases (argon, krypton, and xenon) are in excellent agreement with experiments, there are deviations from the law of corresponding states for the smaller noble gases (neon and helium)

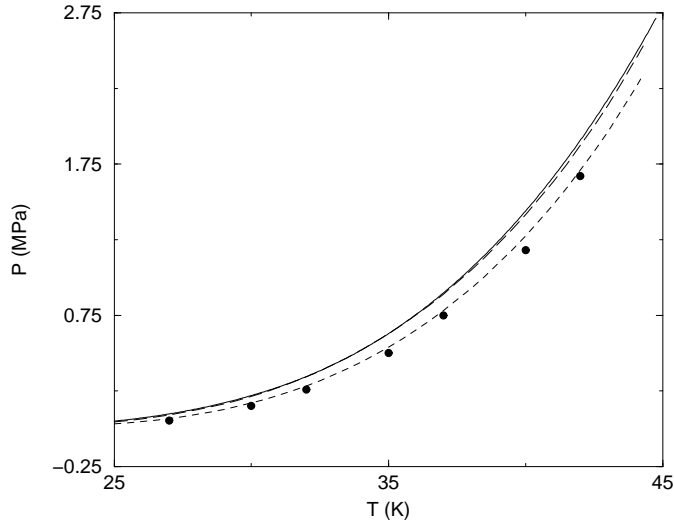


Figure 5.8: Comparison of the vapor pressures for neon: GEMC simulation results with the av45z plus AT potentials (●); the Deiters equation of state (dashed line); the Deiters equation of state with quantum corrections (long dashed line); experiment [93] (solid line)

due to quantum effects. In the present work, the Deiters equation of state was used to calculate the fluid phase equilibria for neon. The spherical cell model was applied to the equation of state to estimate the quantum effects in vapor–liquid equilibria.

Figure 5.7 shows the results of Deiters equation of state (with and without quantum corrections), simulation results of the av45z plus AT potentials, and of experiments for density of the coexisting phases. The results of the same equation of state and simulations for the vapor pressure are plotted in Figure 5.8. From these figures it can be seen that the agreement of the results of the Deiters equation of state with experiments especially in the liquid branch is poor, however, inclusion of the correction function yields an excellent agreement with experiments. On the other hand, there is a fairly good agreement between the results of Deiters equation of state (without quantum corrections) and simulation results (av45z plus AT). These facts confirm that the discrepancies between results of the simulations and experiments are mainly due to the quantum effects.

## 5.2 Argon

### 5.2.1 Potentials

The calculations of high quality *ab initio* potentials for argon are more difficult than for neon, but still possible with the available computer resources. In the present work, the *ab initio* potentials available in literature [54] were used which are resulting from the CCSD(T) level of theory and correlation consistent basis sets. Following the successful application of the  $1/X^3$  extrapolation method for neon potentials, the results of two successive correlation consistent basis sets, avqz and av5z were used to calculate the basis set limit (av45z) of the interaction energies for argon. The resulting potentials of the extrapolations and the results of the av5z basis set are given in Table A.8.

Table 5.3: Characteristic properties of argon–argon potentials.

	av5z	av45z	Aziz
Property	[54]	This work	[94]
$R_e$ (Å)	3.798	3.770	3.757
$\epsilon$ ( $\mu E_h$ )	413.49	451.99	453.60

Figure 5.9 represents the av5z and av45z potentials and compares them with empirical potential for argon of Aziz [94]. It can be seen in the figure that the *ab initio* potential resulting from the av5z basis set is more repulsive at the repulsive wall and less attractive at large distances than the empirical potential; however, the resulting potential from the av45z basis set is in excellent agreement with the empirical potential over the whole range of intermolecular distances. The well depth,  $\epsilon$ , and well position,  $R_e$ , of the *ab initio* and empirical potentials are given in Table 5.3. Surprisingly, the well depth and well position of the av45z potential are only about 0.35% smaller than the corresponding values of the empirical potential, while the well depth and well position of the av5z potential are about 8.8% and 1.1% smaller than the corresponding values of the empirical potential, respectively. The parameters for the avqz potential have even larger deviations from the empirical values.

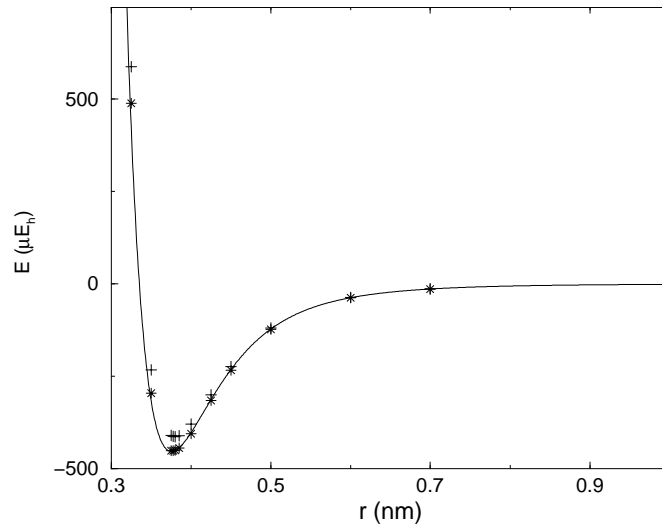


Figure 5.9: Potential energy surface of the argon dimer: the av5z potential (+); the av45z potential (\*); the empirical potential of Aziz [94].

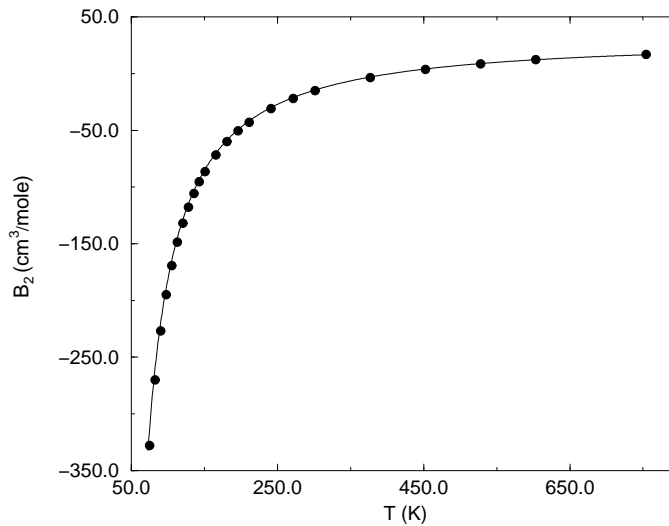


Figure 5.10: Second virial coefficients of argon: calculations with the av45z *ab initio* potential (solid line); experiment [95] (●).

The analytical form of equation 3.24 was used to fit the *ab initio* po-

tential energy surfaces resulting from the av5z and av45z basis sets. Table A.9 shows the parameters of fitting.

The av45z potential was used to calculate the second virial coefficients using relation 3.3. The results are compared with experiments [95] in Figure 5.10. The agreement is very good over the whole range of temperatures confirming that the *ab initio* potential is of high accuracy.

In the simulations including AT potential, the three-body nonadditivity coefficient for argon was set to 517.4 Hartree (Bohr)<sup>9</sup> [79].

### 5.2.2 Simulations

The resulting fitted potentials in previous section were applied in simulations of argon using the GEMC simulation technique. The details of the simulations have already been given in section 4.3. Simulations were performed for the av45z potential using two-body and two-body plus AT potentials, while for the av5z potential simulations were performed for two-body potentials only. The results of the simulations for the av45z, av45z plus AT, and av5z potentials are given in Tables A.10 to A.12, respectively.

In section 3.3.4 it was noted that a natural decomposition of three-body nonadditivity in SAPT provides a great opportunity to investigate the balance between different components. In this way, Lotrich and Szalewicz [61] reported a comprehensive study on three-body nonadditivity of argon. Afterwards, the results of them were used in the simulations of argon to test the effects of different nonadditivity components on the fluid phase of argon in the GEMC simulations [62]. The empirical potential of Aziz [94] was used in their simulations as two-body potential. Their results of simulations are compared with results of the present work.

Results of the simulations for the densities of coexisting phases with the av45z potential of the present work, the empirical potential [62] of Aziz [94], and experimental data [89] are shown in Figure 5.11. Results of the same simulations for the vapor pressure are given in Figure 5.12 and compared with experiments [89]. Figure 5.13 shows the simulation results with the av5z potential, av45z plus AT potentials of the present work, the empirical potential of Aziz [94] plus SAPT three-body potential [62], and experiments [89]. The results of the same simulations for the vapor pressure are illustrated in Figure 5.14 and compared with experiments [89].

Figures 5.11 and 5.12 show that the simulation results with two-body

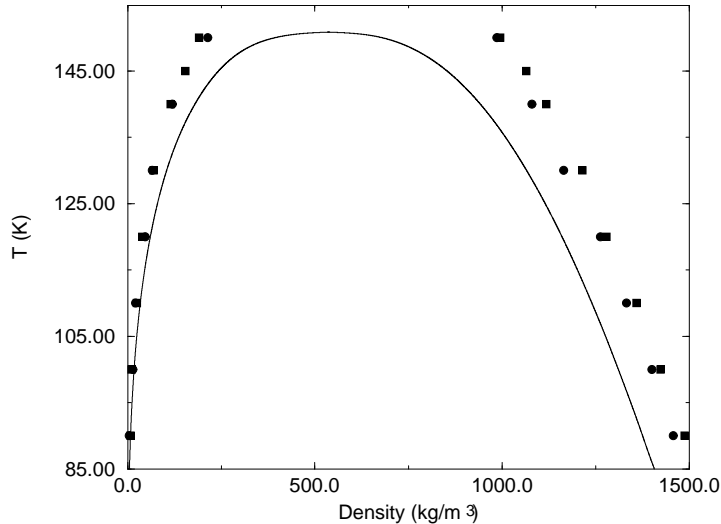


Figure 5.11: Comparison of the density of the coexisting phases for argon: GEMC simulation results with the av45z potential ( $\bullet$ ); GEMC simulation results [62] using the empirical potential of Aziz [94] ( $\blacksquare$ ); experiment [89] (solid line).

potentials (av45z and empirical) are not sufficient to reproduce the fluid phase equilibria for argon, correctly. From the same figures it can also be found that there is a fairly good agreement between two simulation results of the present work and [62]. On the other hand, Figures 5.13 and 5.14 show that the inclusion of three-body interactions (AT plus av45z potential in the present work and SAPT three-body plus Aziz empirical potentials in [62]) leads to good agreements with experiments. From the same figures, a fairly good agreement between the simulation results of the present work and of [62] can be found. Results of the simulations with the av5z potential show a fairly good agreement with experiment especially at low temperatures (Figures 5.13 and 5.14). In section 5.1.2, it was shown that the av5z potential is a good effective potential for neon at low temperatures. The well depth of the av5z potential is lower in comparison with av45z potential (cf. Figures 5.9 and 5.1) leads to an effective two-body potential for neon and argon which includes to some extent the many-body effects. The simulation results for argon reveal that the av5z potential is also a good effective potential at low temperatures. However, the results at upper temperatures have poor agreement with



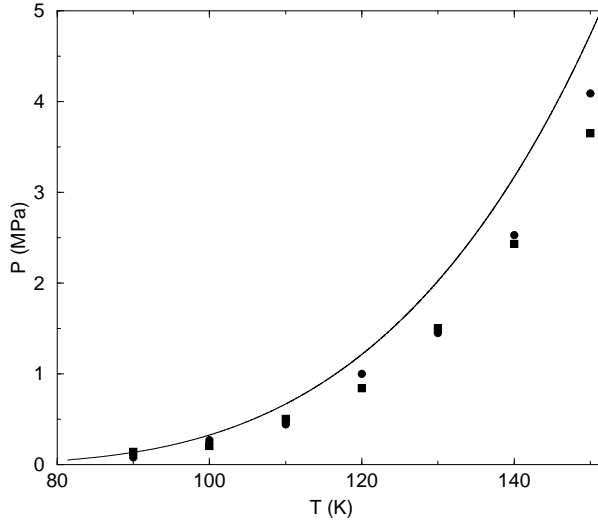


Figure 5.12: Comparison of the vapor pressure for argon: GEMC simulation results with the av45z potential ( $\bullet$ ); GEMC simulation results [62] using the empirical potential of Aziz [94] ( $\blacksquare$ ); experiments [89] (solid line).

experiment.

The results of the simulations with the av45z plus AT and with the av5z potentials were used to calculate the critical properties of argon by means of the equations 2.12 and 2.13. The resulting critical parameters from the present work, the results in [62] and of experiments [89] are shown in Table 5.4. While the predicted critical temperature from the simulation results of av45z plus AT is almost exact (150.89 K), there are about 1.21% overestimations in the prediction of the critical density by the same simulation results. On the other hand, the predicted critical density by the simulation results of empirical potential plus SAPT three-body interactions [62]

Table 5.4: Critical properties for argon (3B in table stands for three-body).

Parameter	av5z	av45z plus AT	Aziz [94] plus SAPT 3B [62]	Experiment [89]
$T_c$ (K)	146.12	150.89	152.10	150.86
$\rho_c$ (kg/m <sup>3</sup> )	550.24	542.07	536.0	535.6

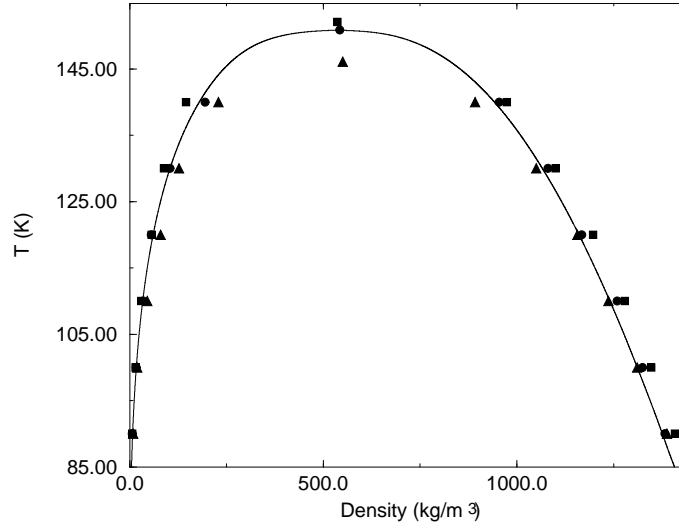


Figure 5.13: Comparison of density of the coexisting phases for argon: GEMC simulation results with the av45z plus AT potentials ( $\bullet$ ); GEMC simulation results using the empirical potential of Aziz [94] plus three-body SAPT potentials [62] ( $\blacksquare$ ); GEMC simulation results with the av5z potential ( $\blacktriangle$ ); experiments [89] (solid line).

is almost exact ( $536.0 \text{ kg/m}^3$ ), however, an overestimation of about 0.82% is observed in the predicted critical temperature by the same simulation results. The predicted critical parameters by the simulation results of the av5z potential have the minor quality, an underestimation of about 3.14% in the predicted critical temperature and an overestimation of about 2.73% in predicted critical density are observed. These figures confirm that the applications of the av45z plus AT potentials in the GEMC simulations are sufficient to reproduce the fluid phase data of argon, correctly. The authors in [62] showed that in the simulations of argon with Aziz empirical potential plus SAPT three-body interactions, the cancellations between different terms make the total three-body potential very similar to the AT term.

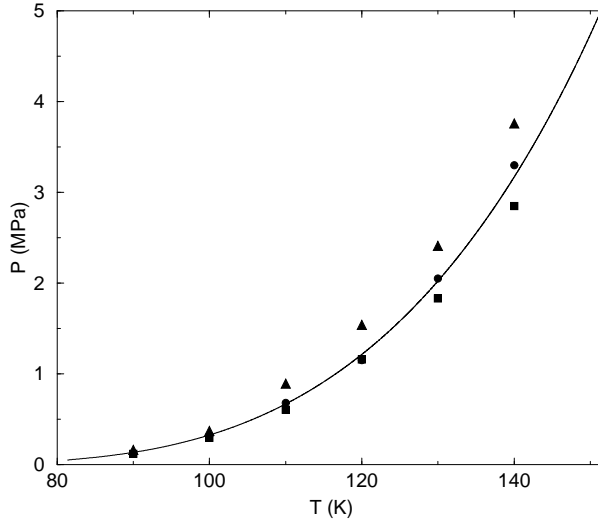


Figure 5.14: Comparison of the vapor pressures for argon: GEMC simulation results with the av45z plus AT potentials (●); GEMC simulation results using the empirical potential of Aziz [94] plus three-body SAPT potentials [62] (■); GEMC simulation results with the av5z potential (▲); experiments [89] (solid line).

## 5.3 Krypton

### 5.3.1 Potentials

Accurate calculations of the interaction potentials for krypton dimer are more difficult than for argon dimer, because of the existence of the fully occupied d-shell in the krypton atom. As a result, the high level *ab initio* calculations for the interaction potentials of krypton dimer in the literature are scarce, and up to our knowledge the only one is the report of Tao [90]. In that report, the frozen-core MP4 level of theory and different basis sets including bond functions were used. Their best results were obtained applying the  $4d3f\text{-}\{2d1f\}$  denoting  $[9s7p4d3f]\text{-}\{3s3p2d1f\}$  basis set (abbreviations are according to [90]) which produced a well depth of  $617 \mu\text{Hartree}$ .

In the present work, new *ab initio* potentials were developed for the interactions of krypton dimer using the CCSD(T) level of theory and two

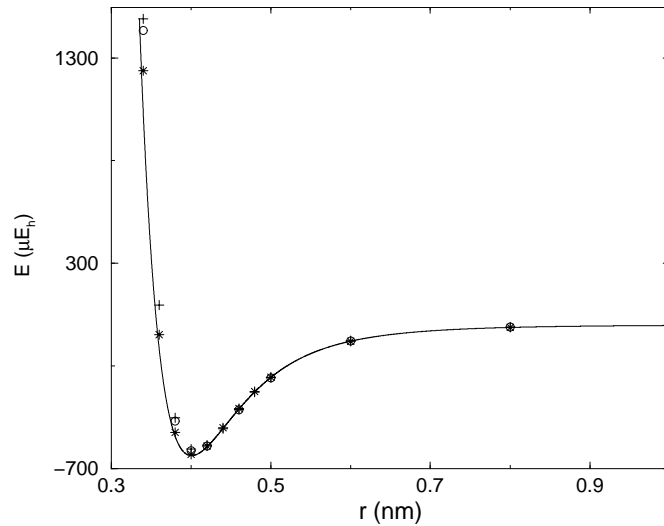


Figure 5.15: Potential energy surface of the krypton dimer: the *av34z* potential (this work) (\*); the  $4d3f\text{-}\{2d1f\}$  potential [90] ( $\circ$ ); the  $4d2f\text{-}\{2d1f\}$  potential [90] (+); the empirical potential of Aziz and Slaman [88] (solid line).

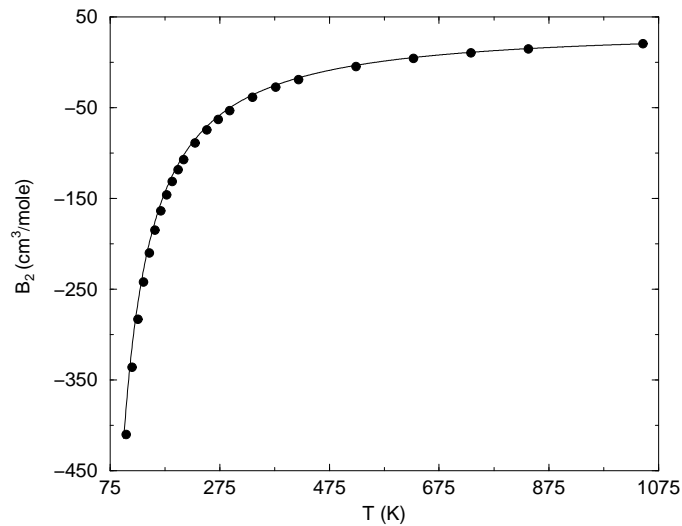


Figure 5.16: Second virial coefficients of krypton: calculations with the *av34z* *ab initio* potential (solid line); and experiment [95] ( $\bullet$ ).

successive correlation-consistent basis sets, avtz and avqz. The calculations were done at 14 different interatomic distances from 3.0 to 10.0 Å. Basis set superposition error were corrected using the counterpoise method of Boys and Bernardi [55]. The  $1/X^3$  extrapolation method of equations 2.12 and 2.13 were applied to calculate the basis set limit (av34z) of the interaction energies. The resulting potentials and the results of Tao [90] (with the frozen-core MP4 level and  $4d2f-\{2d1f\}$  and  $4d3f-\{2d1f\}$  basis sets) are given in Table A.13. Figure 5.15 illustrates the potentials of Table A.13 and compares them with Aziz [88] empirical potential for krypton. Both MP4 potentials are more repulsive at the repulsive wall than Aziz potential and also more attractive at slightly larger distances at well depth. On the other hand, the overall agreement of the av34z potential with the empirical potential is better than both MP4 potentials at the repulsive and attractive parts. The well depth and well position of different *ab initio* potentials are collected in Table 5.5. The well position of the av34z potential is only about 0.22% more than well position of empirical potential and the well depth shows only about 0.88% underestimations. These figures confirm that the av34z potential is of high quality and that the  $1/X^3$  extrapolation method is a powerful scheme to estimate the basis set limit. The MP4 potentials have more deviations in well depths and well positions than the av34z potential in comparison with empirical potential.

Table 5.5: Characteristic properties of krypton–krypton potentials.

	CCSD(T) av34z	MP4 $4d2f-\{2d1f\}$	MP4 $4d3f-\{2d1f\}$	Aziz and Slaman
$R_e$ (Å)	4.017	4.078	4.058	4.008
$\epsilon$ ( $\mu E_h$ )	631.56	609.80	617.00	637.17
Reference	This work	Tao [90]	Tao [90]	[88]

The av34z potential was used to calculate the second virial coefficient for krypton from 100 K up to 1050 K using equation 3.3. The resulting second virial coefficients are compared with experimental data [95] in Figure 5.16. The overall agreement of the calculated and experimental second virial coefficients is very good over the whole range of temperatures confirming that the *ab initio* potential is of high accuracy.

The mathematical form of equation 3.24 was used to fit the *ab initio* potentials of the av34z basis set of the present work and the  $4d2f\text{-}\{2d1f\}$  basis set potential of Tao. In the next section, it is shown that the recent potential is an excellent effective potential for krypton. The fitting parameters are collected in Table A.14.

In the simulations including the AT potential, the three-body nonadditivity coefficient for krypton was set to 1554 Hartree (Bohr)<sup>9</sup> [79].

### 5.3.2 Simulations

Simulation details were given in section 4.3. Simulations were performed slightly above the triple point up to near the critical region. Two *ab initio* potentials, av34z and  $4d2f\text{-}\{2d1f\}$  were used in the simulations to reproduce the fluid phase equilibria for krypton. For the av34z potential, simulations were performed with two-body and two-body plus AT potentials, while for  $4d2f\text{-}\{2d1f\}$  potential, simulations were performed only with two-body potential. The results of the simulations are given in Tables A.15 to A.17 for the av34z, av34z plus AT, and  $4d2f\text{-}\{2d1f\}$  potentials, respectively. Figures 5.17 and 5.18 show the results of the same simulations for density of the coexisting phases and vapor pressures, respectively and compare the results with experimental data [89]. Equations 2.12 and 2.13 were used to calculate the critical properties of krypton from the simulation results. The critical properties are given in Table 5.6 and compared with experimental data.

Table 5.6: Critical properties of krypton.

Parameter	av34z plus AT	$4d2f\text{-}\{2d1f\}$	experiments [89]
$T_c$ (K)	207.62	207.42	209.48
$\rho_c$ (kg/m <sup>3</sup> )	952.80	932.43	908.40

The simulation results of av34z potential show that the two-body potential is not sufficient to calculate the fluid phase equilibria for krypton, while the inclusion of the AT potential to the configuration energy improves the results and leads to a very good agreement with experimental data. The same conclusions were done in the simulation of argon using av45z basis set with and without AT potential in the section 5.2.2 and also

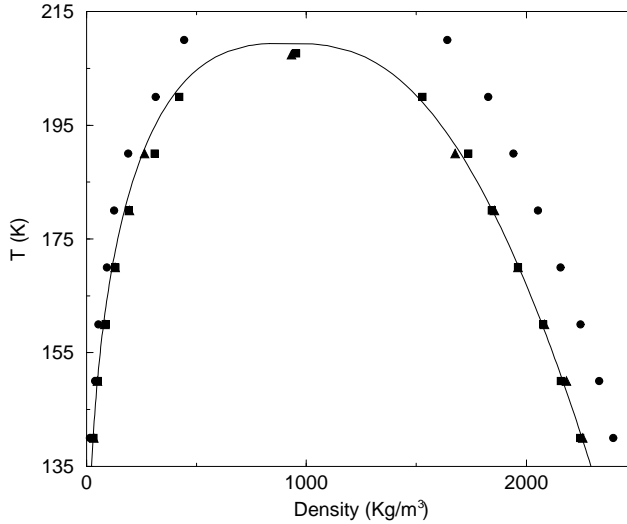


Figure 5.17: Comparison of density of the coexisting phases for krypton: GEMC simulation results with the av34z potential ( $\bullet$ ); GEMC simulation results with the av34z plus AT potentials ( $\blacksquare$ ); GEMC simulation results with the  $4d2f\text{-}\{2d1f\}$  potential ( $\blacktriangle$ ); experiments [89] (solid line).

the same conclusions were made in the simulations of argon, krypton, and xenon using accurate empirical potentials with and without AT [91], also in the simulations of argon using accurate empirical potential with and without AT [92].

The predicted critical temperature from the simulation results of the av34z plus AT potential is only 0.89% less than the experimental value and the predicted critical density by the same simulations shows 4.89% overestimations. The predicted critical temperature by the simulation results of the MP4 potential is very close to the predicted temperature by the other potential, but the predicted critical density has less deviations (2.65%) than the other potential from the experimental value.

The simulation results of this section show that the av34z potential is of high accuracy. On the other hand, the ability of predictions of densities of the coexisting phases, vapor pressures, and critical parameters of krypton using the  $4d2f\text{-}\{2d1f\}$  potential confirms that, the potential is an excellent effective two-body potential for krypton. The effects of many-body interactions in the fluid phase properties of krypton are canceled by

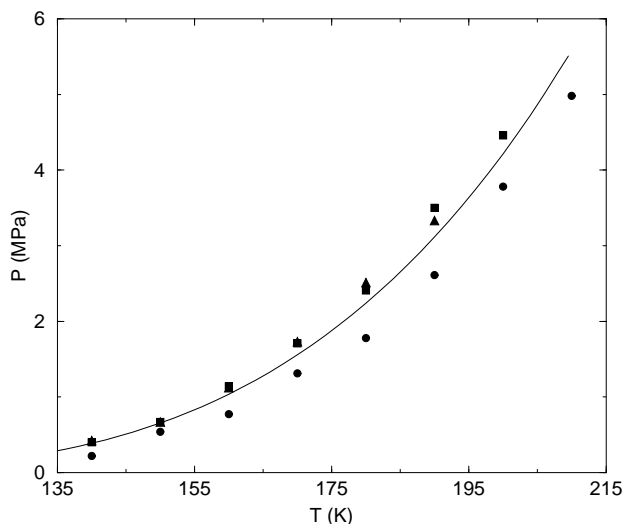


Figure 5.18: Comparison of the vapor pressures of krypton: GEMC simulation results with the av34z potential (●); GEMC simulation results with the av34z plus AT potentials (■); GEMC simulation results with the  $4d2f\text{-}\{2d1f\}$  potential (▲); experiments [89] (solid line).

the approximations in the calculations of the interaction potential by the  $4d2f\text{-}\{2d1f\}$  basis set at MP4 level. It was shown in previous sections that the av5z potentials give fairly good effective two-body potentials for neon and argon (especially at low temperatures).

## 5.4 The binary mixture neon–argon

### 5.4.1 Potentials

For simulations of neon–argon binary mixtures, three pair potentials have to be known: two like pairs, namely neon–neon, argon–argon, and one unlike pair, namely neon–argon. For the like pairs, we used the same *ab initio* potentials which were applied in the simulations of pure neon and argon (av5z and av45z potentials). For the unlike pair, following the application of  $1/X^3$  extrapolation method for neon and argon pair potentials, the same method was used to develop new *ab initio* potential for



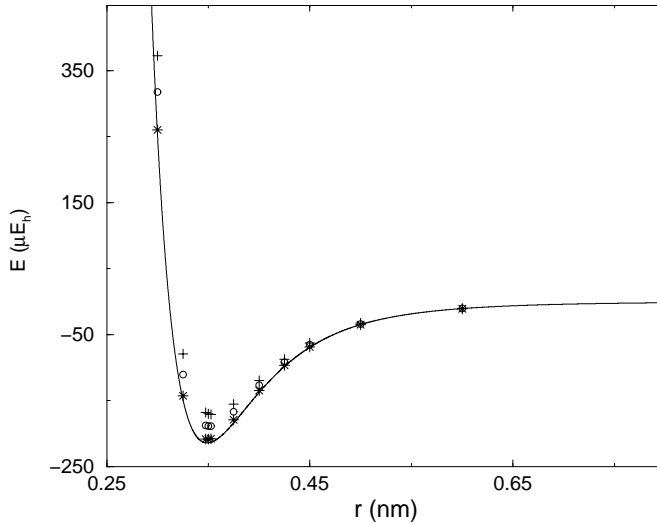


Figure 5.19: Potential energy surface of the neon–argon dimer: the avqz potential [54] (+); the av5z potential [54] (o); the av45z potential (this work) (\*); the empirical potential of Barrow and Aziz [96] (solid line).

neon–argon interactions. The avqz and av5z potentials required for the extrapolation were taken from the same report [54]. The resulting potentials from the avqz, av5z, and av45z basis sets for the neon–argon interactions are given in Table A.18. The *ab initio* potentials of Table A.18 are plotted in Figure 5.19 and compared with the empirical potential of Barrow and Aziz [96] for neon–argon. It can be seen in the figure that both the avqz and av5z potentials are much more repulsive at repulsive wall and less attractive in the potential well and also in the dispersion parts than the empirical potential. On the other hand, the av45z potential shows a good agreement with the empirical potential over the whole range of interatomic distances.

Table 5.7 shows the characteristic properties of the *ab initio* potentials and compares with the corresponding values of the empirical potential of Barrow and Aziz [96]. Surprisingly, the well position of the av45z potential is exact and the well depth of the potential is only 2.54% less than the empirical value (however, according to the recent spectroscopic results of Grabow *et al.* [97], the well depth of the av45z potential is exact). The well position of the avqz and av5z potentials are respectively 1.69% and 0.83%

Table 5.7: Characteristic properties of the neon–argon potentials.

	avqz	av5z	av45z	Barrow and
Property	[54]	[54]	This work	Aziz [96]
$R_e$ (Å)	3.548	3.518	3.490	3.489
$\epsilon$ ( $\mu E_h$ )	170.95	188.65	208.61	214.05

higher than the empirical value, while the well depth of these potentials show 20.14% and 11.87% underestimations with respect to the corresponding empirical value. These figures confirm that the extrapolation method  $1/X^3$  is an efficient method and also confirm that the resulting potential av45z is of high accuracy.

The mathematical form of equation 3.24 was used to fit the *ab initio* potential surfaces resulting from the av5z and av45z basis sets. The fitting parameters are given in Table A.19.

Table 5.8: Cross second virial coefficients of neon–argon.

	$-B_{12}$ (cm <sup>3</sup> /mol)	$-B_{12}$ (cm <sup>3</sup> /mol)
$T$ (K)	This work	Shamma and Rigby [98]
84.42	44.3	45.2
87.42	41.1	41.7
92.84	35.9	35.5
95.82	33.4	35.2
101.94	28.8	30.1
110.78	23.1	25.4
121.34	17.7	20.3
129.93	14.0	17.3
137.83	11.1	16.1

For mixtures it is difficult to measure the cross second virial coefficients accurately, especially at low temperatures. As a result, experimental data are scarce in the literature. The av45z potential was used to calculate the cross second virial coefficients of neon–argon. The results are shown in Table 5.8 and compared with experimental data [98]. It can be seen that the calculated second virial coefficients are in good agreement with exper-

iments at low temperatures, as the temperature goes up, the agreement deteriorates and also the uncertainties in the experiments increase [98].

Table 5.9: Like and unlike three-body nonadditivity coefficients of neon and argon trimers.

Interaction	This work	Leonard and Barker [79]
Ne-Ne-Ne	12.02	
Ne-Ne-Ar	42.13	40.49
Ar-Ar-Ar	517.40	
Ar-Ar-Ne	147.63	142.50

In the simulations of neon-argon mixture including the AT potentials, the unlike three-body nonadditivity coefficients were calculated from a geometrical mean of the like coefficients

$$\begin{aligned}\nu_{\text{Ne-Ne-Ar}} &= \sqrt[3]{\nu_{\text{Ne}}\nu_{\text{Ne}}\nu_{\text{Ar}}} \\ \nu_{\text{Ne-Ar-Ar}} &= \sqrt[3]{\nu_{\text{Ne}}\nu_{\text{Ar}}\nu_{\text{Ar}}}\end{aligned}\tag{5.3}$$

where  $\nu_{\text{Ne-Ne-Ar}}$  and  $\nu_{\text{Ne-Ar-Ar}}$  are the three-body nonadditivity coefficients for trimers formed by two neon and one argon atoms, and one neon and two argon atoms, respectively.

Table 5.9 shows the three-body nonadditivity coefficients of the like and unlike interactions which were used in the simulations of neon-argon binary mixtures as well as those by Leonard and Barker [79]. For the noble gases, geometrical means are good approximations for the unlike three-body nonadditivity coefficients.

## 5.4.2 Simulations

Details of the simulations were given in section 4.3. For the av45z potentials, simulations were performed with two-body and two-body plus AT potentials along four isotherms: 101.94 K, 110.78 K, 121.36 K, and 129.93 K. For the av5z potentials, simulations were performed only with two-body potentials along three isotherms: 95.82 K, 101.94 K, and 110.78

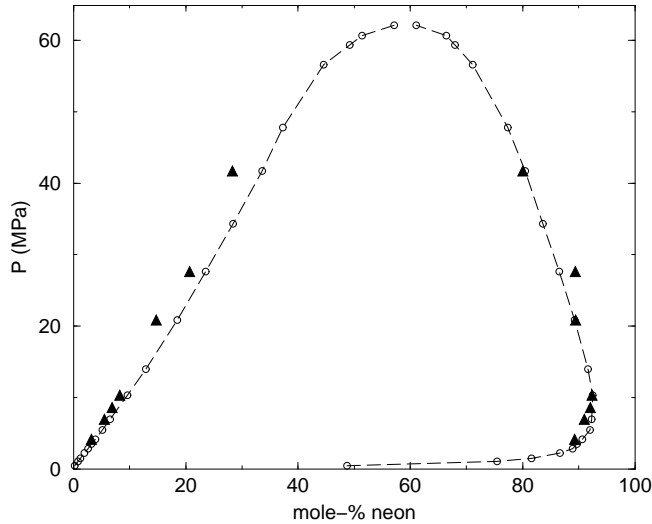


Figure 5.20: Pressure-composition diagram for the neon–argon mixture at 95.82 K: GEMC simulation results with the av5z potential (▲); experiments [99,100] (o-solid line).

K. Results of the simulations with the av45z potential are given in Tables A.20 to A.23 and the results of the simulations with the av45z plus AT potentials are collected in Tables A.24 to A.27. Results of the simulations with the av5z potential are given in Tables A.30 to A.30. Results of the simulations with the av45z with and without AT potentials are plotted in Figures 5.21 to 5.24 for four isotherms from 101.94 K up to 129.93 K, respectively. In two Figures 5.21 and 5.22, simulation results with the av5z potential are also illustrated. In Figure 5.20 simulation result of the av5z potential along the isotherm 95.82 K are plotted. At each isotherm, results of the simulations are compared with experiments [99,100].

In the simulations of pure neon with the av45z potential, it was shown that quantum effects are present and affect the thermodynamic properties of neon especially at low temperatures. However, the lowest isotherm in the simulations of neon–argon mixture is high enough to assume that these quantum effects are negligible.

At low temperatures and higher pressures, much higher computational efforts are needed to reach the equilibrium. Under such conditions, the particle transfer trial moves are difficult to perform, especially for the larger

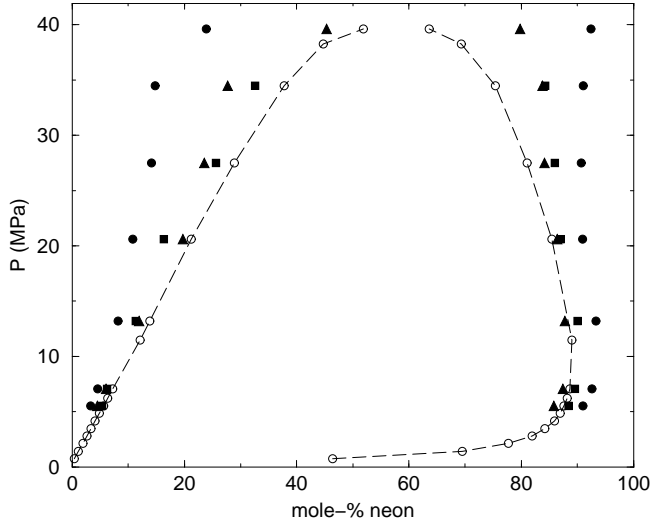


Figure 5.21: Pressure-composition diagram for the neon-argon mixture at 101.94 K: GEMC simulation results with the av5z potential ( $\blacktriangle$ ); GEMC simulation results with the av45z potential ( $\bullet$ ); GEMC simulation results with the av45z plus AT potentials ( $\blacksquare$ ); experiments [99, 100] ( $\circ$ -solid line).

atom (argon in this case). Although the difference in sizes of neon and argon atoms is not large, it is advantageous to use the particle identity exchange technique (cf. section 2.5.4) in order to increase the efficiency of the simulations. At very low temperatures and high pressures as well as in the vicinity of critical region, the results of the simulations are sensitive to the details of the potentials, and the deviations from the experiments increase. The results of the simulations were almost independent of the initial densities of each boxes, although, the initial compositions were chosen to be approximately the same as the experimental compositions of both phases in order to have a fast equilibration.

Results of the simulations with the av45z potentials in Figures 5.21 to 5.24 show that at each isotherm there is a fairly good agreement with experiments at low pressures; however, at higher pressures, the deviations increase. The same figures show that the inclusion of the AT potential into the total configuration energy improves the results. The same effects were observed in the case of pure noble gases (see the previous sections), however, these effects in mixtures are more pronounced. Far from the

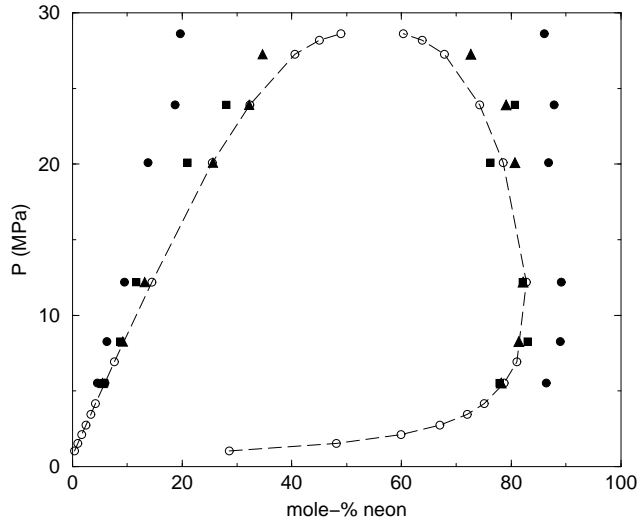


Figure 5.22: Pressure-composition diagram for the neon–argon mixture at 110.78 K: GEMC simulation results with the av5z potential ( $\blacktriangle$ ); GEMC simulation results with the av45z potential ( $\bullet$ ); GEMC simulation results with the av45z plus AT potentials ( $\blacksquare$ ); experiments [99,100] ( $\circ$ -solid line).

critical region the densities of the gas phase in mixtures are much higher than in a pure system and as a result the AT potentials contribute more to the configurational energies in the case of mixtures.

Simulation results with the av5z potential in Figures 5.20 to 5.22 are in good agreement with experimental data. It was shown in sections 5.1.2 and 5.2.2 that the av5z potential is a good effective potential for pure neon and argon. The results of this section show that the av5z potential is also a good effective two-body potential for the neon–argon interactions. As the simulations with two-body potentials demand less computational efforts, the simulations of neon–argon mixtures with the av5z potential were performed for the low isotherm 95.82 K where the simulations with the av45z plus AT potentials are quite expensive.

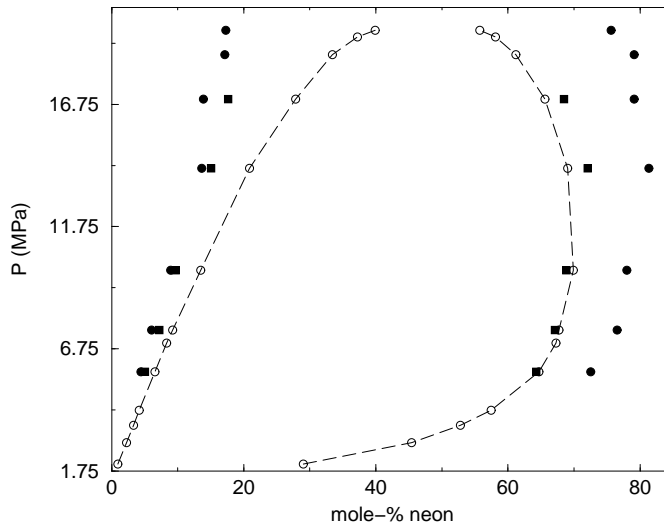


Figure 5.23: Pressure-composition diagram for the neon–argon mixture at 121.36 K: GEMC simulation results with the av45z potential ( $\bullet$ ); GEMC simulation results with the av45z plus AT potentials ( $\blacksquare$ ); experiments [99, 100] ( $\circ$ -solid line).

## 5.5 The binary mixture argon–krypton

### 5.5.1 Potentials

Simulations of the argon–krypton binary mixtures require knowledge of three pair potentials, i.e., two for the like pair interactions argon–argon and krypton–krypton and one for the unlike pair interaction argon–krypton. For the argon–argon pair interactions, the av45z potential (cf. section 5.2.2) was used and for the krypton–krypton pair interactions, the av34z potential (cf. section 5.3.2) was applied. For the unlike pair interaction argon–krypton, new *ab initio* potentials were developed. The CCSD(T) level of theory and two correlation consistent basis sets avtz, avqz were used to calculate the interaction energies at 14 different interatomic distances from 3.0 to 10.0 Å. The counterpoise method of Boys and Bernardi [55] was used to correct the basis set superposition error. The  $1/X^3$  method was applied to estimate the basis set limit (av34z) of the interaction energies. Results of the calculations for the *ab initio* potentials avtz, avqz, and av34z

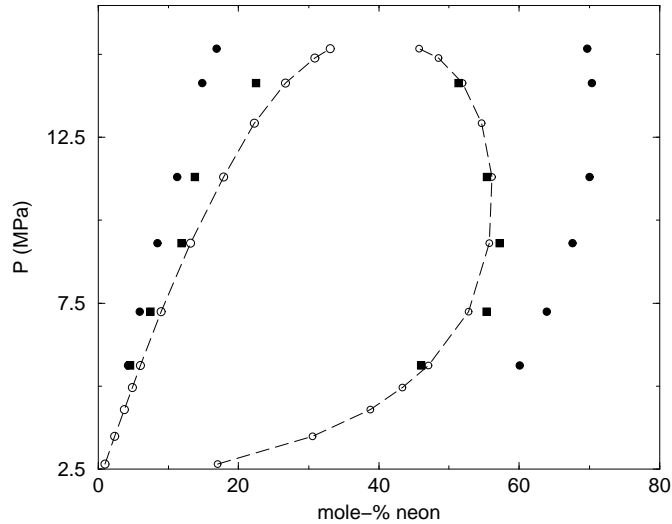


Figure 5.24: Pressure-composition diagram for the neon–argon mixture at 129.93 K: GEMC simulation results with the av45z potential ( $\bullet$ ); GEMC simulation results with the av45z plus AT potentials ( $\blacksquare$ ); experiments [99, 100] ( $\circ$ -solid line).

are collected in Table A.31. Figure 5.25 shows the argon–krypton *ab initio* potentials of Table A.31. It can be seen that, the av34z potential is less repulsive at the repulsive wall and also is more attractive at the dispersion part than the other two *ab initio* potentials.

For the sake of comparison, characteristic properties of the *ab initio* potentials avtz, avqz, and av34z are shown together with the empirical values of Kestin *et al.* [101] and also with the results of a newly developed theory in Table 5.10. McLure *et al.* [102] proposed a theory based on the nonconformality of intermolecular interactions which gives accurate interaction potentials for simple fluids.

The value of  $\sigma$  (a distance where interaction energy is zero) for the avtz, avqz, and av34z potentials show 4.47%, 2.27%, and 0.66% overestimation over the corresponding empirical value [101], respectively. The well position  $R_e$  for the avtz, avqz, and av34z potentials is 5.54%, 3.47%, and 1.72% larger than the corresponding value of nonconformal theory [102]. The well depth of the avtz is too shallow in comparison with the empirical value and is too small by 28.51%. The corresponding value for the avqz



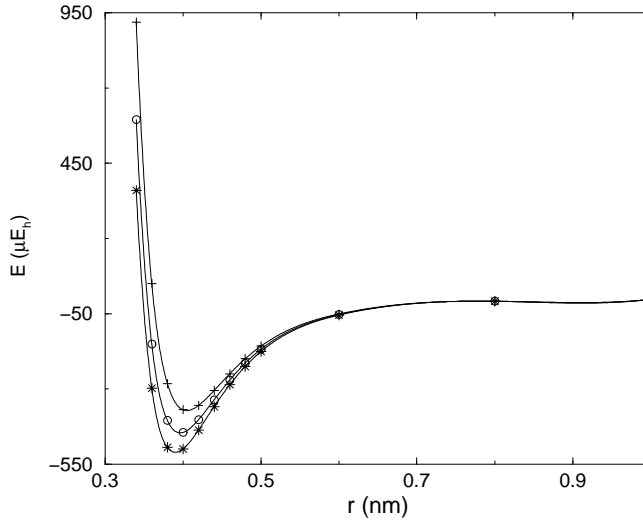


Figure 5.25: Potential energy surfaces for the argon–krypton dimer: avtz potential (+-solid line); avqz potential (o-solid line); av34z potential (\*-solid line).

potential is 14.72% less than the empirical value. The av34z potential can reproduce about 97.32% of the empirical well depth. These figures show that the av34z potential is of high accuracy.

Equation 5.3 was used to calculate the unlike three-body nonadditivity coefficients in trimers of argon–krypton. Table 5.11 summarizes the nonadditivity coefficients for the like and unlike trimers which were used in the simulations of argon–krypton mixture and compares the calculated unlike coefficient of equation 5.3 with the corresponding values of Leonard

Table 5.10: Characteristic properties of argon–krypton potentials.

Property	avtz potential	avqz potential	av34z potential	Kestin <i>et al.</i> [101]	McLure <i>et al.</i> [102]
$\sigma$ (Å)	3.6190	3.5425	3.4868	3.464	3.4570
$R_e$ (Å)	4.0475	3.9682	3.9008		3.8350
$\epsilon$ ( $\mu E_h$ )	371.80	445.95	511.04	525.06	537.50

Table 5.11: Like and unlike three-body nonadditivity coefficients of argon and krypton trimers.

Interaction	This work	Leonard and Barker [79]
Ar-Ar-Ar	517.4	
Ar-Ar-Kr	746.5	744.6
Kr-Kr-Kr	1554.0	
Kr-Kr-Ar	1077.1	1074.0

and Barker [79]. It can be seen that the geometrical mean is an excellent approximation for calculation of the unlike coefficients.

## 5.5.2 Simulations

Simulations were performed with the av45z potential of argon–argon, the av34z potential of krypton–krypton and argon–krypton with and without

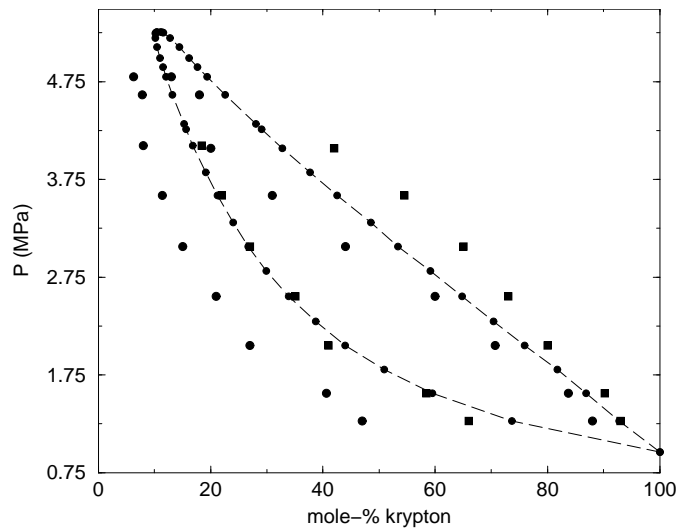


Figure 5.26: Pressure-composition diagram for the argon–krypton system at 158.15 K: GEMC simulation results with two-body potentials ( $\bullet$ ); GEMC simulation results with two-body plus AT potentials ( $\blacksquare$ ); experiments [103] ( $\circ$ -solid line).

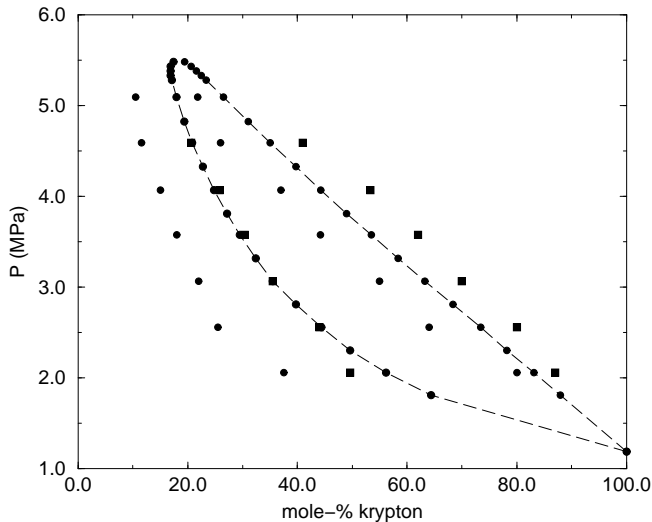


Figure 5.27: Pressure-composition diagram for the argon–krypton system at 163.15 K: GEMC simulation results with two-body potentials (●); GEMC simulation results with two-body plus AT potentials (■); experiments [103] (○-solid line).

the AT three-body interactions along for the four isotherms 158.15 K, 163.15 K, 177.38 K, and 193.15 K. The results of the simulations for two-body potentials are given in Tables A.33 to A.36 and for two-body plus AT potentials are given in Tables A.37 to A.40. Figures 5.26 to 5.29 show the results of the simulations along for the isotherms and compare with experimental data [103].

Qualitatively, the system argon–krypton shows the behavior of a nearly ideal binary mixture. Over the whole range of composition, the liquid branch is nearly a straight line; the gas branch has a parabolic form. Like the simulations for the neon–argon mixtures, along each isotherm, at high pressures especially near the critical region more computational efforts were needed to reach the equilibrium conditions. However, as the difference in sizes of the argon and krypton atoms is not large, the particle transfer Monte Carlo moves were performed efficiently even along the lowest isotherm.

In the simulations of pure argon (cf. section 5.2.2), it was shown that the av45z potential is of high accuracy. In section 5.3.2, it was also shown

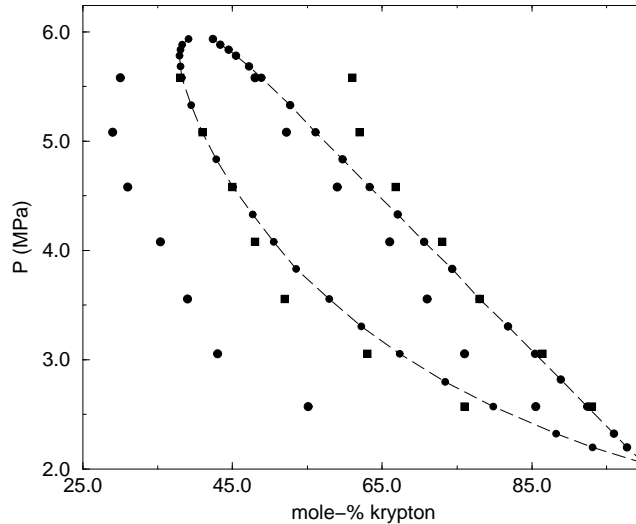


Figure 5.28: Pressure-composition diagram for the argon–krypton system at 177.38 K: GEMC simulation results with two-body potentials ( $\bullet$ ); GEMC simulation results with two-body plus AT potentials ( $\blacksquare$ ); experiments [103] ( $\circ$ -solid line).

that the *av34z* potential gives good results in the simulations of pure krypton. In previous section, the quality of *av34z* potential for the unlike pair interaction of argon–krypton was studied, and comparisons with accurate potentials showed that it is also of high accuracy. As a result, it was expected to reproduce the fluid phase behavior of argon–krypton mixture with a good accuracy.

The results of the simulations in Figures 5.26 to 5.29 show that the two-body *ab initio* potentials are not sufficient to calculate the fluid phase of the argon–krypton binary mixtures correctly. At each isotherm, in both phases, there are underestimations in the calculations of krypton molar percentage. However, the geometries of the fluid phases along the all isotherms are almost correct; the liquid branches are approximately straight and the gas branches are almost parabolic. Extrapolations of the predicted fluid phases to the pure krypton (100% krypton in the figures) give pressures which are less than the corresponding experimental values. The same phenomena was observed for the calculations of the vapor pressures of pure krypton (cf. section 5.3.2): simulations with the *av34z* potential give the

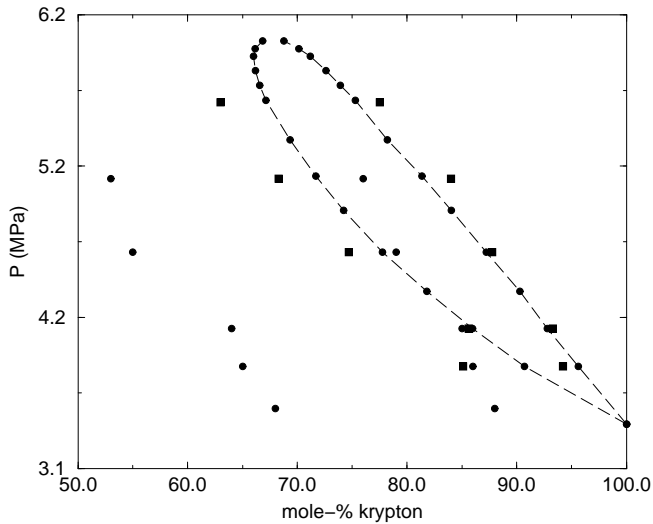


Figure 5.29: Pressure-composition diagram for the argon–krypton system at 193.15 K: GEMC simulation results with two-body potentials ( $\bullet$ ); GEMC simulation results with two-body plus AT potentials ( $\blacksquare$ ); experiments [103] ( $\circ$ -solid line).

pressures below the experimental values.

On the other hand, the same figures show that the inclusions of the AT potentials to the configuration energies lead to better agreement with experimental data. The same conclusions were observed in the simulations of the neon–argon mixture (section 5.4.2). At each isotherm, additions of the AT potentials lead to a good agreement in the gas branch, however, the agreement in the liquid branch is poor and results for the krypton mole fraction are always above the experimental data. The geometries of the phase diagram is still correct, the approximate straight lines of the liquid branch and almost parabolic shape of gas branch. In the simulations of pure krypton it was shown that the inclusion of the AT potentials to the energy leads to overestimations in the calculations of vapor pressure (see Figure 5.18).



# Chapter 6

# Conclusion

The adequacy of *ab initio* pair potential plus Axilrod–Teller (AT) three-body interaction for description of macroscopic properties of pure and binary mixtures of noble gases in simulations was examined. Three pure systems, and two binary mixtures were studied. New computer programs were developed to perform standard *NVT*-Gibbs ensemble simulations for pure systems and *NPT*-Gibbs ensemble simulations for binary mixtures.

An investigation of prediction methods of phase equilibria of pure neon was reported. Three *ab initio* potentials with and without AT three-body interactions were applied in simulations, however, none of them was able to predict the phases equilibria of neon accurately. An equation of state and a newly developed correction function which accounts for quantum effects were applied to show that the discrepancies in the simulations are mainly due to quantum effects.

Two *ab initio* potentials were used in simulations of pure argon. The predicted phase diagrams and critical properties with accurate *ab initio* potential plus AT interaction are in excellent agreement with experimental measurements. The results of the simulation with the second *ab initio* potential are in good agreement with experimental data especially at low temperatures, suggesting that the potential is a good effective two-body potential for argon.

For krypton new high quality *ab initio* potentials were developed. The results of the simulations with *ab initio* plus AT potentials are in excellent agreement with experimental data in temperature–density projection diagram, however, the results of the same simulations for the vapor pressures show slightly overestimations at higher temperatures. Another *ab initio* potential (which was taken from literature) was used in simulations. The predicted phase diagrams and critical properties are in excellent agreement with experimental data confirming that the potential is an excellent effective two-body potential for the krypton dimer.

The central idea of global simulations was extended to the system of binary mixtures. Two sets of *ab initio* potentials were applied in the simulations of neon–argon mixtures. The first set consists of the highly accurate potentials. The results of the simulations show that the inclusion of AT potential leads to better agreement with experimental measurements. For each isotherm the agreement at low pressures is excellent, however, at high pressures especially near critical region the results of the simulations show



deviations from experimental data. The predicted phase envelope with the second set of *ab initio* potentials are in good agreement with experimental measurements, which suggests that these potentials are good effective ones for the system.

For the heteronuclear interaction of argon–krypton new high-quality *ab initio* potentials were calculated. Predicted phase diagrams with accurate two-body potentials for the argon–krypton binary mixture show large deviations from experimental data in both liquid and gas branches. Addition of the AT potential to the total configuration energy leads to an excellent agreement in the gas phase. However, the deviations from experiment were observed in the liquid branch. The shape of the phase diagrams along all isotherms were predicted accurately: an almost straight line in liquid branch and a parabolic shape in gas branch.

The results of the simulations for above systems (except for neon which shows non-negligible quantum effects) show that the accurate two-body potentials are not sufficient to reproduce the phase equilibria. On the other hand, the addition of AT potential to the energy leads to an excellent agreement with experimental data for pure systems. For binary mixtures, the agreement is not as good as for pure systems. For most of the above systems two-body effective potentials were introduced. The approximations in the *ab initio* calculations of these potentials lead to a (accidental) cancellations of many-body effects. The importance of deriving effective two-body potentials are evident from the fact that accounting for the three-body interactions requires considerably more computing resources than for the pair interaction.



# Bibliography

- [1] J. S. Rowlinson and F. S. Swinton, *Liquids and Liquid Mixture* 3rd edn (London: Butterworth Scientific, 1982).
- [2] K. E. Gubbins, “Application of molecular theory to phase equilibrium predictions” Chapter 6 in *Thermodynamic Modeling*, Sandler, S. I. Ed., (Marcel Dekker: NY, 1992).
- [3] L. L. Lee, *Molecular Thermodynamics of Nonideal Fluids* (Butterworth, Heinemann, 1988).
- [4] S. I. Sandler, *Modeling Vapor-Liquid Equilibria : Cubic Equations of State and their Mixing Rules* (Cambridge University Press, 1988).
- [5] A. Z. Panagiotopoulos, *J. Phys.: Condens. Matter* **12**, R25 (2000).
- [6] D. Müller and J. Fischer, *Mol. Phys.* **69**, 463 (1990).
- [7] A. Lotfi, J. Vrabec and J. Fischer, *Mol. Phys.* **76**, 1319 (1992).
- [8] B. Widom, *J. Chem. Phys.* **39**, 2808 (1963).
- [9] D. A. Kofke, *Adv. Chem. Phys.* **105**, 405 (1999).
- [10] D. A. Kofke, *J. Chem. Phys.* **98**, 4149 (1993).
- [11] M. Mehta and D. A. Kofke, *Chem. Eng. Sci.* **49**, 2633 (1994).
- [12] F. A. Escobedo and J. J. de Pablo, *J. Chem. Phys.* **106**, 2911 (1997).
- [13] A. Z. Panagiotopoulos, *Mol. Phys.* **61**, 813 (1987).

- [14] A. Z. Panagiotopoulos, N. Quirke, M. Stapleton and D. J. Tildesley, *Mol. Phys.* **63**, 527 (1988).
- [15] M. P. Allen and D. J. Tildesley, *Computer Simulation of Liquids* (Oxford: Oxford University Press, 1987).
- [16] B. Smith and D. Frenkel, *Mol. Phys.* **68**, 951 (1989).
- [17] D. A. McQuarrie *Statistical mechanics* (Harper and Row, New York, 1976).
- [18] J. P. Valleau, *J. Chem. Phys.* **108**, 2962 (1998).
- [19] A. D. Bruce, *Phys. Rev. E* **55**, 2315 (1997).
- [20] A. Z. Panagiotopoulos, *Int. J. Thermophys.* **10**, 447 (1989).
- [21] N. B. Wilding, *J. Phys.: Condens Matter* **9**, 585 (1997).
- [22] B. Smith and D. Frenkel, *Understanding Molecular Simulation* (Academic, New York, 1996)
- [23] D. A. Kofke and E. D. Glandt, *Mol. Phys.* **64**, 1105 (1988).
- [24] G. C. A. M. Mooij, D. Frenkel, and B. Smith, *J. Phys. Condens. Matter* **4**, L255 (1992).
- [25] G. Maitland, M. Rigby, E. Smith and W. Wakeham, *Intermolecular Forces: Their Origin and Determination* (Oxford University Press, New York, 1981).
- [26] H. Margenau and N. R. Kestner, *Theory of Intermolecular Forces* (Pergamon, Oxford, 1971).
- [27] A. Z. Panagiotopoulos, *Int. J. Thermophys.* **1**, 1057 (1994).
- [28] B. Smith, *J. Chem. Phys.* **96**, 8639 (1992).
- [29] V. I. Harismiadis, N. K. Koutras, D. P. Tassios and A. Z. Panagiotopoulos, *Fluid Phase Equil.* **65**, 1 (1991).

- [30] J. J. Nocolas, K. E. Gubbins, W. B. Streett and D. J. Tildesley, *Mol. Phys.* **37**, 1429 (1979).
- [31] G. Wu and R. J. Sadus, *Fluid Phase Equil.* **170**, 269 (2000).
- [32] J. R. Errington, G. C. Boulougouris, I. G. Economou, A. Z. Panagiotopoulos and D. N. Theodorou, *J. Phys. Chem. B* **102**, 8865 (1998).
- [33] D. Levesque and J. J. Weis, in *Monte Carlo Methods in Condensed Matter Physics*, edited by K. Binder (Springer-Verlag, Berlin Heidelberg, 1992), Vol. 71.
- [34] *Adv. Chem. Phys.* **105**, (1999).
- [35] E. B. Smith and A. R. Tindell, *Faraday Discuss. Chem. Soc.* **73**, 221 (1982).
- [36] K. Lucas, *Applied Statistical Thermodynamics* (Springer-Verlag, Berlin Heidelberg, 1991).
- [37] G. C. Maitland, M. Mustafa, V. Vesovic and W. A. Wakeham, *Mol. Phys.* **57**, 1015 (1986).
- [38] R. Car and M. Parrinello, *Phys. Rev. Lett.* **55**, 2471 (1985).
- [39] P. L. Silvestrelli and M. Parrinello, *Phys. Rev. Lett.* **82**, 3308 (1999).
- [40] P. Hobza, *Ann. Rep. Prog. Phys. Chem.* **93**, 257 (1997).
- [41] R. Eggenberger, S. Gerber, H. Huber and M. Welcker, *Mol. Phys.* **82**, 689 (1994).
- [42] K. Leonhard and U. K. Deiters, *Mol. Phys.* **98**, 1603 (2000).
- [43] F. London, *Z. Phys. Chem. (B)* **11**, 222 (1930).
- [44] F. London, *Trans. Faraday Soc.* **33**, 8 (1937).
- [45] A. D. Buckingham, *Adv. Chem. Phys.* **12**, 107 (1967).
- [46] B. Jeziorski, R. Moszynski and K. Szalewicz, *Chem. Rev.* **94**, 1887 (1994).

- [47] P. Claverie, *Int. J. Quant. Chem.* **5**, 273 (1971).
- [48] H. B. G. Casimir and D. Polder, *Phys. Rev.* **73**, 360 (1948).
- [49] B. Jeziorski and M. van Hemert, *Mol. Phys.* **31**, 713 (1976).
- [50] K. Szalewicz and B. Jeziorski, *Mol. Phys.* **38**, 191 (1979).
- [51] K. Szalewicz and B. Jeziorski, *Symmetry-Adapted Perturbation Theory of Intermolecular Interactions*, in S. Scheiner (Ed.), *Molecular Interactions* (Wiley, New York, 1997).
- [52] M. Gutowski, F. B. van Duijneveldt, G. Chalasinski and L. Piela, *Mol. Phys.* **61**, 233 (1987).
- [53] D. E. Woon, *J. Chem. Phys.* **100**, 2838 (1994).
- [54] S. M. Cybulski and R. R. Toczyłowski, *J. Chem. Phys.* **111**, 10520 (1999).
- [55] S. F. Boys and F. Bernardi, *Mol. Phys.* **19**, 553 (1970).
- [56] J. A. Venables and B. L. Smith, In *Rare Gas Solids*; M. L. Klein and J. A. Venables, Eds. (Academic: London, 1976); chapter 10.
- [57] *Chem. Rev.* **100**, (2000).
- [58] B. M. Axilrod and E. Teller, *J. Chem. Phys.* **11**, 299 (1943).
- [59] R. J. Bell, *J. Phys. B* **3**, 751 (1970).
- [60] M. J. Elrod and R. J. Saykally, *Chem. Rev.* **94**, 1975 (1994).
- [61] V. F. Lotrich and K. Szalewicz, *J. Chem. Phys.* **106**, 9688 (1997).
- [62] R. Bukowski and K. Szalewicz, *J. Chem. Phys.* **114**, 9518 (2001).
- [63] D. E. Woon and T. H. Dunning, Jr., *J. Chem. Phys.* **98**, 1358 (1993).
- [64] D. E. Woon and T. H. Dunning, Jr., *J. Chem. Phys.* **100**, 2975 (1994).
- [65] D. E. Woon and T. H. Dunning, Jr., *J. Chem. Phys.* **103**, 4572 (1995).

- [66] D. Feller, *J. Chem. Phys.* **96**, 6104 (1992).
- [67] K. A. Peterson, *J. Chem. Phys.* **102**, 262 (1995).
- [68] J. S. Lee and Y. Park, *J. Chem. Phys.* **112**, 230 (2000).
- [69] A. Wilson and T. H. Dunning, *J. Chem. Phys.* **106**, 8718 (1997).
- [70] W. Klopper, *Mol. Phys.* **99**, 481 (2001).
- [71] T. Helgaker, W. Klopper, H. Koch, and J. Noga, *J. Chem. Phys.* **106**, 9639 (1997).
- [72] D. G. Truhlar, *Chem Phys. Lett.* **294**, 45 (1998).
- [73] T. Hollebeek, T. Ho, and H. Rabitz, *Annu. Rev. Phys. Chem.* **50**, 537 (1999).
- [74] T. Korona, L. Williams, R. Bukowski, B. Jeziorski, and K. Szalewicz, *J. Chem. Phys.* **106**, 5109 (1997).
- [75] K. T. Tang and J. P. Toennies, *J. Chem. Phys.* **80**, 3726 (1984).
- [76] G. Marcelli and R. J. Sadus, *J. Chem. Phys.* **111**, 1533 (1999).
- [77] R. A. Aziz and M. J. Slaman, *Chem. Phys.* **130**, 187 (1989).
- [78] G. Grochola, S. Russo, and I. Snook, *Mol. Phys.* **95**, 471 (1998).
- [79] P. J. Leonard and J. A. Barker, *Theoret. Chem., Adv. Perspect.* **1**, 117 (1975).
- [80] L. M. Sese, *Mol. Phys.* **78**, 1167 (1993).
- [81] K. Singer and W. Smith, *Mol. Phys.* **64**, 1215 (1988).
- [82] J. P. Hansen and J. J. Weis, *Phys. Rev. A* **36**, 2440 (1987).
- [83] U. K. Deiters, *Fluid. Phase Equil.* **10**, 173 (1983).
- [84] R. Laghaei and U. K. Deiters, in preparation.
- [85] U. K. Deiters, *Chem. Eng. Sci.* **36**, 1139 (1981).

- [86] U. K. Deiters, Chem. Eng. Sci. **36**, 1146 (1981).
- [87] U. K. Deiters, Chem. Eng. Sci. **37**, 855 (1982).
- [88] R. A. Aziz and M. J. Slaman, Mol. Phys. **58**, 679 (1986).
- [89] N. B. Vargaftik, *Tables on the Thermophysical Properties of Liquids and Gases in Normal and Dissociated States* (Wiley, New York, 1975).
- [90] F. Tao, J. Chem. Phys. **111**, 2407 (1999).
- [91] G. Marcelli and R. J. Sadus, J. Chem. Phys. **111**, 1533 (1999).
- [92] J. A. Anta, E. Lomba, and M. Lombardero, Phys. Rev E **55**, 2707 (1997).
- [93] Lnadolt-Börnstein, II. Band, 2. Teil (a) (Berlin: Springer Verlag, 1960), pp. 4, 10, 186.
- [94] R. A Aziz, J. Chem. Phys. **99**, 4518 (1993).
- [95] K. R. Hall, (editor in chief), TRC, h-71,91, *Thermodynamic Tables-Non-Hydrocarbons*, (The Texas A and M University:Thermodynamic Research Center, 1972).
- [96] D. A. Barrow and R. A. Aziz, J. Chem. Phys. **89**, 6189 (1988).
- [97] J. U. Grabow, A. S. Pine, T. Fraser, F. J. Lovas, R. D. Suenram, T. Emilsson, E. Arunan, and H. S. Gutowski, J. Chem. Phys. **102**, 1181 (1995).
- [98] O. Shamma and M. Rigby, J. Chem. Soc. Faraday Trans. **78**, 689 (1982).
- [99] W.B. Streett, J. Chem. Phys. **42**, 500 (1965).
- [100] W.B. Streett, J. Chem. Phys. **46**, 3282 (1967).
- [101] J. Kestin, K. Knierim, E. A. Mason, B. Najafi, S. T. Ro, and M. Waldman, J. Phys. Chem. Ref. Data **13**, 229 (1984).



- [102] I. A. McLure, J. E. Ramos, and F. del Rio, *J. Phys. Chem. B* **103**, 7019 (1999).
- [103] J. A. Schouten, A. Deerenberg, and N. J. Trappeniers, *Physica* **81A**, 151 (1975).



# Appendix A

## Tables

Table A.1: *ab initio* potentials ( $\mu E_h$ ) for the neon dimer.

R ( $\text{\AA}$ )	avtz+(332)	avqz	av5z	av45z
2.250	3561.42	3635.34	3502.53	3363.19
2.500	789.26	854.25	787.66	717.80
2.750	39.72	81.52	50.78	18.53
3.000	-117.02	-91.51	-107.72	-124.73
3.075	-124.81	-102.80	-116.27	-130.40
3.100	-125.58	-104.59	-117.34	-130.72
3.125	-125.67	-105.50	-117.63	-130.36
3.250	-118.53	-102.22	-111.79	-121.83
3.500	-90.25	-79.24	-85.35	-91.76
3.750	-63.29	-56.11	-59.92	-63.92
4.000	-43.29	-38.87	-41.19	-43.62
4.500	-20.59	-18.96	-19.84	-20.76
5.000	-10.46	-9.78	-10.20	-10.64

Table A.2: Parameters of fitting for the neon-neon potentials.

Parameter	avtz+(332)	av5z	av45z
A ( $E_h$ )	78.52	68.59	75.40
$\alpha$ ( $a_0^{-1}$ )	2.13371	2.09504	2.16774
$\beta$ ( $a_0^{-2}$ )	-.035	-.040	-.027
b ( $a_0^{-1}$ )	1.88	1.65	1.86
$C_6$ ( $E_h a_0^6$ )	6.96	6.01	6.08
$C_8$ ( $E_h a_0^8$ )	49.87	9.80	114.08
$C_{10}$ ( $E_h a_0^{10}$ )	2393.96	6832.96	2008.32

Table A.3: GEMC simulation results for neon using the av45z potential.

T/K	$\rho/\text{kgm}^{-3}$	U/Jmol <sup>-1</sup>	p/MPa	$\mu/\text{Jmol}^{-1}$	H/Jmol <sup>-1</sup>
27(g)	4.4(8)	-10(2)	0.048(8)	-2201(35)	209(4)
27(l)	1321(7)	-1869(12)	0.46(24)	-1718(130)	-1862(9)
30(g)	10.0(1)	-22(3)	0.12(1)	-2297(26)	216(5)
30(l)	1267(8)	-1771(13)	0.09(27)	-2134(152)	-1770(11)
32(g)	20(2)	-41(3)	0.24(2)	-2319(22)	202(5)
32(l)	1228(4)	-1699(6)	0.37(31)	-2241(88)	-1693(5)
35(g)	35(2)	-68(4)	0.43(2)	-2439(11)	187(6)
35(l)	1164(5)	-1592(8)	0.78(29)	-2436(31)	-1579(10)
37(g)	47(4)	-88(7)	0.60(5)	-2528(20)	172(10)
37(l)	1101(4)	-1493(6)	0.58(27)	-2543(23)	-1483(9)
40(g)	89(5)	-161(7)	1.11(4)	-2622(10)	90(12)
40(l)	1034(8)	-1385(12)	1.17(32)	-2627(21)	-1363(8)
42(g)	133(11)	-228(20)	1.55(7)	-2698(11)	8(29)
42(l)	972(10)	-1294(16)	1.50(30)	-2725(14)	-1264(22)
45(g)	191(13)	-306(21)	2.1(1)	-2850(5)	-79(29)
45(l)	837(26)	-1115(32)	2.2(2)	-2869(16)	-1064(30)

Table A.4: GEMC simulation results of neon using the av45z plus AT potentials.

T/K	$\rho/\text{kgm}^{-3}$	U/Jmol <sup>-1</sup>	p/MPa	$\mu/\text{Jmol}^{-1}$	H/Jmol <sup>-1</sup>
27(g)	5.0(4)	-10(9)	0.053(4)	-2175(17)	208(3)
27(l)	1294(4)	-1796(7)	0.17(32)	-1849(103)	-1794(8)
30(g)	13(1)	-29(3)	0.15(2)	-2241(23)	206(5)
30(l)	1234(10)	-1692(17)	-0.002(458)	-2127(93)	-1693(19)
32(g)	21(3)	-45(7)	0.26(3)	-2304(29)	196(11)
32(l)	1188(7)	-1614(11)	0.31(16)	-2285(61)	-1609(12)
35(g)	40(3)	-78(6)	0.50(3)	-2407(17)	172(9)
35(l)	1126(7)	-1513(10)	0.64(16)	-2385(39)	-1502(9)
37(g)	62(6)	-116(11)	0.75(6)	-2473(18)	130(16)
37(l)	1080(4)	-1440(7)	0.77(20)	-2484(26)	-1426(6)
40(g)	97(4)	-173(7)	1.18(3)	-2608(7)	73(13)
40(l)	997(12)	-1320(19)	1.22(27)	-2603(14)	-1296(18)
42(g)	155(4)	-267(7)	1.67(3)	-2676(5)	-49(10)
42(l)	938(17)	-1237(23)	1.82(36)	-2708(29)	-1199(24)

Table A.5: GEMC simulation results of neon using the avtz+(332) potential.

T/K	$\rho/\text{kgm}^{-3}$	U/Jmol <sup>-1</sup>	p/MPa	$\mu/\text{Jmol}^{-1}$	H/Jmol <sup>-1</sup>
27(g)	5(1)	-11(3)	0.06(1)	-2170(47)	208(4)
27(l)	1282(7)	-1783(12)	0.23(29)	-1864(236)	-1780(11)
30(g)	14(2)	-30(3)	0.16(1)	-2223(24)	204(4)
30(l)	1223(8)	-1678(13)	0.03(29)	-2104(66)	-1678(13)
32(g)	21(4)	-42(8)	0.26(5)	-2306(42)	203(11)
32(l)	1181(8)	-1608(13)	0.30(39)	-2259(79)	-1603(12)
35(g)	44(2)	-82(3)	0.53(3)	-2386(9)	164(3)
35(l)	1114(10)	-1498(16)	0.55(20)	-2385(18)	-1489(16)
37(g)	64(6)	-116(12)	0.78(5)	-2462(18)	132(18)
37(l)	1068(12)	-1425(16)	0.73(22)	-2473(34)	-1412(14)
40(g)	107(7)	-182(11)	1.26(5)	-2586(10)	58(17)
40(l)	987(16)	-1303(22)	1.48(29)	-2614(22)	-1274(23)
42(g)	150(14)	-251(23)	1.68(9)	-2674(9)	-24(31)
42(l)	896(14)	-1178(17)	1.58(26)	-2712(4)	-1143(17)
45(g)	250(33)	-383(43)	2.44(12)	-2815(11)	-182(58)
45(l)	624(99)	-864(110)	2.40(23)	-2825(11)	-765(134)

Table A.6: GEMC simulation results of neon using the avtz+(332) plus AT potentials.

T/K	$\rho/\text{kgm}^{-3}$	U/Jmol <sup>-1</sup>	p/MPa	$\mu/\text{Jmol}^{-1}$	H/Jmol <sup>-1</sup>
27(g)	8(1)	-17(3)	0.08(1)	-2084(35)	198(6)
27(l)	1257(5)	-1716(7)	0.12(24)	-1941(68)	-1714(10)
30(g)	17(1)	-36(3)	0.19(1)	-2187(16)	195(5)
30(l)	1193(4)	-1607(7)	0.08(34)	-2161(67)	-1607(9)
32(g)	27(1)	-53(1)	0.32(1)	-2252(5)	183(1)
32(l)	1143(7)	-1526(13)	0.28(18)	-2257(44)	-1521(13)
35(g)	49(3)	-91(6)	0.59(3)	-2364(11)	151(9)
35(l)	1079(7)	-1427(11)	0.75(9)	-2376(24)	-1414(12)
37(g)	67(4)	-120(7)	0.81(4)	-2452(11)	125(11)
37(l)	1021(6)	-1340(8)	0.65(26)	-2477(22)	-1328(12)
40(g)	131(11)	-221(19)	1.45(7)	-2556(9)	2(27)
40(l)	940(11)	-1223(15)	1.52(27)	-2578(11)	-1192(17)
42(g)	195(4)	-317(6)	1.91(3)	-2645(5)	-119(10)
42(l)	886(30)	-1150(38)	1.97(47)	-2710(23)	-1108(39)

Table A.7: GEMC simulation results of neon using the av5z potential.

T/K	$\rho/\text{kgm}^{-3}$	U/Jmol <sup>-1</sup>	p/MPa	$\mu/\text{Jmol}^{-1}$	H/Jmol <sup>-1</sup>
27(g)	10(1)	-21(2)	0.11(1)	-2027(18)	192(4)
27(l)	1221(8)	-1574(13)	-0.23(19)	-1964(47)	-1578(12)
30(g)	26(3)	-48(6)	0.28(3)	-2098(24)	176(10)
30(l)	1158(4)	-1472(8)	0.05(28)	-2077(34)	-1472(11)
32(g)	41(2)	-73(3)	0.46(2)	-2161(9)	155(7)
32(l)	1119(6)	-1413(9)	0.30(37)	-2168(18)	-1408(7)
35(g)	69(7)	-115(6)	0.78(6)	-2288(18)	115(19)
35(l)	1029(19)	-1282(25)	0.63(31)	-2295(35)	-1271(24)
37(g)	109(5)	-176(10)	1.19(4)	-2355(6)	45(15)
37(l)	958(13)	-1183(17)	0.84(14)	-2382(15)	-1166(20)
40(g)	187(10)	-284(16)	1.83(3)	-2488(4)	-85(28)
40(l)	790(69)	-972(77)	1.89(22)	-2522(10)	-922(87)

Table A.8: *ab initio* potentials ( $\mu E_h$ ) for the argon dimer.

R ( $\text{\AA}$ )	avqz	av5z	av45z
3.000	3312.11	3156.12	2992.46
3.250	680.99	587.03	488.45
3.500	-172.64	-232.91	-296.14
3.750	-371.62	-410.57	-451.44
3.775	-375.72	-412.82	-451.75
3.800	-378.04	-413.57	-450.85
3.850	-378.32	-410.74	-444.75
4.000	-355.59	-380.09	-405.80
4.250	-285.52	-300.51	-316.24
4.500	-215.09	-224.33	-234.02
5.000	-115.93	-119.57	-123.39
6.000	-36.41	-37.05	-37.72
7.000	-13.72	-13.87	-14.03

Table A.9: Parameters of fitting for the argon–argon potentials.

Parameter	av5z	av45z
A ( $E_h$ )	57.33	56.21
$\alpha$ ( $a_0^{-1}$ )	1.31322	1.31938
$\beta$ ( $a_0^{-2}$ )	-.0552	-.050
$b$ ( $a_0^{-1}$ )	1.45	1.70
$C_6$ ( $E_h a_0^6$ )	61.01	60.98
$C_8$ ( $E_h a_0^8$ )	1906.53	1941.02
$C_{10}$ ( $E_h a_0^{10}$ )	68755.80	62960.00



Table A.10: GEMC simulation results of argon using the av45z potential.

T/K	$\rho/\text{kgm}^{-3}$	U/Jmol <sup>-1</sup>	p/MPa	$\mu/\text{Jmol}^{-1}$	H/Jmol <sup>-1</sup>
90(g)	4(1)	-30(10)	0.08(2)	-9969(161)	701(16)
90(l)	1457(7)	-6360(43)	0.21(55)	-7574(680)	-6356(46)
100(g)	14(1)	-95(11)	0.27(3)	-10345(73)	685(16)
100(l)	1401(13)	-6044(73)	-0.07(39)	-9569(429)	-6048(63)
110(g)	21(3)	-134(24)	0.44(6)	-11151(115)	710(44)
110(l)	1333(7)	-5677(40)	0.31(49)	-10864(199)	-5670(46)
120(g)	47(6)	-282(35)	1.0(1)	-11650(84)	569(54)
120(l)	1263(6)	-5304(28)	1.39(29)	-11628(107)	-5262(33)
130(g)	66(2)	-363(16)	1.45(5)	-12460(25)	527(25)
130(l)	1164(7)	-4842(23)	1.55(77)	-12405(66)	-4791(40)
140(g)	119(12)	-626(51)	2.53(17)	-13088(56)	-229(78)
140(l)	1080(18)	-4445(73)	2.49(46)	-13092(65)	-4356(61)
150(g)	214(3)	-1077(18)	4.1(1)	-13771(21)	-310(14)
150(l)	986(34)	-4037(125)	4.2(5)	-13773(84)	-3871(131)

Table A.11: GEMC simulation results of argon using the av45z plus AT potentials.

T/K	$\rho/\text{kgm}^{-3}$	U/Jmol <sup>-1</sup>	p/MPa	$\mu/\text{Jmol}^{-1}$	H/Jmol <sup>-1</sup>
90(g)	7(1)	-49(13)	0.12(2)	-9688(143)	670(20)
90(l)	1382(11)	-5783(58)	0.11(39)	-8985(661)	-5782(65)
100(g)	17(2)	-116(17)	0.32(4)	-10214(91)	654(29)
100(l)	1325(7)	-5479(31)	0.18(66)	-10012(55)	-5476(23)
110(g)	34(5)	-217(34)	0.68(8)	-10815(97)	583(54)
110(l)	1259(7)	-5153(40)	0.55(36)	-10768(90)	-5138(36)
120(g)	56(2)	-324(4)	1.15(3)	-11532(17)	509(11)
120(l)	1167(8)	-4724(39)	0.84(49)	-11555(99)	-4697(32)
130(g)	104(19)	-571(115)	2.05(24)	-12194(85)	226(166)
130(l)	1080(23)	-4338(88)	1.96(30)	-12207(107)	-4268(89)
140(g)	195(24)	-997(121)	3.30(24)	-12890(37)	-306(166)
140(l)	954(6)	-3816(25)	3.27(32)	-12932(55)	-3681(34)

Table A.12: GEMC simulation results of argon using the av5z potential.

T/K	$\rho/\text{kgm}^{-3}$	U/Jmol <sup>-1</sup>	p/MPa	$\mu/\text{Jmol}^{-1}$	H/Jmol <sup>-1</sup>
90(g)	9(1)	-57(9)	0.15(2)	-9509(102)	660(15)
90(l)	1387(5)	-5669(27)	-0.15(70)	-8581(245)	-5675(25)
100(g)	19(1)	-119(11)	0.37(2)	-10095(50)	649(18)
100(l)	1311(12)	-5272(63)	0.25(46)	-9899(198)	-5266(56)
110(g)	45(4)	-260(24)	0.89(6)	-10596(58)	520(38)
110(l)	1236(10)	-4901(48)	1.04(52)	-10616(110)	-4870(37)
120(g)	80(8)	-423(43)	1.54(9)	-11276(51)	350(73)
120(l)	1156(10)	-4533(44)	2.03(19)	-11296(69)	-4465(39)
130(g)	127(9)	-639(49)	2.41(12)	-12009(33)	121(69)
130(l)	1050(18)	-4071(74)	2.43(59)	-12062(73)	-3982(63)
140(g)	229(16)	-1099(95)	3.76(9)	-12719(22)	-438(142)
140(l)	892(15)	-3442(47)	3.91(28)	-12932(47)	-3269(52)

Table A.13: *ab initio* potentials ( $\mu E_h$ ) for the krypton dimer.

R (Å)	CCSD(T) avtz	CCSD(T) avqz	CCSD(T) av34z	MP4 [90] 4d2f- $\{2d1f\}$	MP4 [90] 4d3f- $\{2d1f\}$
3.0	12463.2	11316.8	10480.2	11092.4	10905.2
3.2	5578.2	4783.0	4202.7	4607.2	
3.4	2172.5	1632.0	1237.6	1491.3	1433.9
3.6	567.7	211.2	-47.2	96.0	
3.8	-129.4	-357.1	-523.3	-452.5	-468.5
4.0	-384.9	-527.2	-631.0	-604.6	-612.8
4.2	-437.6	-525.7	-590.0	-585.8	-590.0
4.4	-405.9	-461.0	-501.2	-505.3	
4.6	-346.1	-381.5	-407.3	-412.7	-414.2
4.8	-283.5	307.0	-324.2	-328.0	
5.0	-227.5	-243.7	-255.5	-257.4	-258.2
6.0	-74.7	-77.5	-79.5	-77.0	-77.8
8.0	-12.2	-12.3	-12.4	-11.0	-11.0
10.0	-3.1	-3.1	-3.1	-2.7	-2.7

Table A.14: Parameters of fitting for the krypton–krypton potentials.

Parameter	av34z	$4d2f\text{-}\{2d1f\}$
A ( $E_h$ )	109.66	106.83
$\alpha$ ( $a_0^{-1}$ )	1.32512	1.36966
$\beta$ ( $a_0^{-2}$ )	-.0404	-.028
$b$ ( $a_0^{-1}$ )	1.40	1.45
$C_6$ ( $E_h a_0^6$ )	120.14	90.95
$C_8$ ( $E_h a_0^8$ )	3565.02	5776.58
$C_{10}$ ( $E_h a_0^{10}$ )	364467.00	487994.80

Table A.15: GEMC simulation results of krypton using the av34z potential.

T/K	$\rho/\text{kgm}^{-3}$	U/Jmol $^{-1}$	p/MPa	$\mu/\text{Jmol}^{-1}$	H/Jmol $^{-1}$
140(g)	16(1)	-87(8)	0.22(2)	-16984(75)	1032(7)
140(l)	2396(20)	-8265(86)	-0.23(96)	-16529(576)	-8276(70)
150(g)	40(5)	-210(25)	0.54(6)	-17343(128)	926(37)
150(l)	2331(31)	-7972(131)	-0.7(66)	-16892(457)	-7977(124)
160(g)	55(9)	-270(42)	0.77(11)	-18280(162)	919(69)
160(l)	2247(18)	-7632(66)	0.37(89)	-18279(242)	-7621(60)
170(g)	94(8)	-448(33)	1.3(1)	-18943(81)	730(51)
170(l)	2156(7)	-7244(29)	1.0(5)	-18864(97)	-7209(43)
180(g)	125(16)	-574(83)	1.8(2)	-19861(118)	626(122)
180(l)	2052(25)	-6836(92)	1.7(4)	-19849(79)	-6771(96)
190(g)	189(24)	-841(116)	2.6(2)	-20660(101)	320(171)
190(l)	1941(36)	-6425(114)	2.5(5)	-20685(118)	-6320(116)
200(g)	314(20)	-1358(93)	3.8(1)	-21433(32)	-346(129)
200(l)	1827(18)	-5994(65)	3.6(8)	-21501(90)	-5834(87)
210(g)	444(15)	-1782(71)	5.0(1)	-22347(13)	-837(110)
210(l)	1641(38)	-5368(129)	4.6(7)	-22433(93)	-5140(11)

Table A.16: GEMC simulation results for krypton using the av34z plus AT potentials.

T/K	$\rho/\text{kgm}^{-3}$	U/Jmol <sup>-1</sup>	p/MPa	$\mu/\text{Jmol}^{-1}$	H/Jmol <sup>-1</sup>
140(g)	31(3)	-174(17)	0.40(3)	-16324(86)	898(25)
140(l)	2244(9)	-7369(33)	0.02(17)	-16215(87)	-7371(35)
150(g)	51(4)	-268(22)	0.67(5)	-17099(76)	837(34)
150(l)	2157(18)	-7027(67)	0.79(59)	-16983(87)	-6999(59)
160(g)	87(6)	-438(30)	1.14(7)	-17818(56)	663(37)
160(l)	2077(15)	-6722(54)	0.87(21)	-17878(118)	-6690(51)
170(g)	132(11)	-630(63)	1.7(1)	-18644(62)	462(94)
170(l)	1962(21)	-6294(66)	1.8(5)	-18755(52)	-6220(55)
180(g)	193(23)	-871(104)	2.4(2)	-19497(78)	182(161)
180(l)	1843(41)	-5890(139)	2.1(3)	-19603(158)	-5798(153)
190(g)	310(44)	-1312(170)	3.5(3)	-20334(56)	-358(228)
190(l)	1736(41)	-5539(131)	3.5(5)	-20432(67)	-5373(129)
200(g)	422(34)	-1687(122)	4.5(2)	-21272(21)	-796(158)
200(l)	1527(104)	-4897(299)	4.7(4)	-21388(64)	-4650(301)

Table A.17: GEMC simulation results of krypton using the  $4d2f$ - $\{2d1f\}$  potential.

T/K	$\rho/\text{kgm}^{-3}$	U/Jmol <sup>-1</sup>	p/MPa	$\mu/\text{Jmol}^{-1}$	H/Jmol <sup>-1</sup>
140(g)	33(3)	-173(19)	0.42(4)	-16268(88)	904(31)
140(l)	2257(10)	-7495(38)	-0.09(56)	-15860(235)	-7502(30)
150(g)	50(2)	-249(10)	0.67(3)	-17098(51)	868(14)
150(l)	2182(14)	-7187(62)	0.40(37)	-16850(151)	-7174(71)
160(g)	84(11)	-393(48)	1.12(12)	-17831(111)	736(67)
160(l)	2082(26)	-6798(94)	0.82(66)	-17848(126)	-6768(91)
170(g)	131(7)	-588(35)	1.73(7)	-18604(39)	526(56)
170(l)	1963(18)	-6329(71)	1.37(24)	-18710(73)	-6274(73)
180(g)	195(9)	-842(44)	2.5(1)	-19434(35)	239(48)
180(l)	1854(30)	-5946(108)	2.6(5)	-19481(76)	-5831(108)
190(g)	265(10)	-1089(39)	3.3(1)	-20340(23)	-33(54)
190(l)	1677(28)	-5356(79)	3.1(9)	-20380(58)	-5207(64)

Table A.18: *ab initio* potentials ( $\mu E_h$ ) for the neon–argon dimer.

R (Å)	avqz	av5z	av45z
2.500	6559.88	6368.37	6167.44
2.750	1918.36	1817.03	1710.72
3.000	372.42	317.71	260.31
3.250	-79.52	-110.46	-142.92
3.475	-167.84	-187.57	-208.27
3.500	-169.84	-188.69	-208.46
3.525	-170.94	-188.82	-207.58
3.750	-155.30	-166.91	-179.09
4.000	-119.74	-126.99	-134.60
4.250	-87.29	-91.81	-96.55
4.500	-62.57	-65.48	-68.53
5.000	-32.55	-33.80	-35.11
6.000	-10.29	-10.53	-10.78

Table A.19: Parameters of fitting for the neon–argon potentials.

Parameter	av5z	av45z
A ( $E_h$ )	65.50	80.30
$\alpha$ ( $a_0^{-1}$ )	1.68212	1.8085
$\beta$ ( $a_0^{-2}$ )	-.047	-.026
$b$ ( $a_0^{-1}$ )	1.50	1.70
$C_6$ ( $E_h a_0^6$ )	18.30	15.78
$C_8$ ( $E_h a_0^8$ )	440.72	563.00
$C_{10}$ ( $E_h a_0^{10}$ )	17186.30	21460.00

Table A.20: GEMC simulation results for the neon-argon mixture with the av45z potential along 101.94 K.

p/ MPa	$\rho/\text{kgm}^{-3}$	U/Jmol <sup>-1</sup>	p/ MPa	$\mu_{\text{ne}}/\text{Jmol}^{-1}$	$\mu_{\text{ar}}/\text{Jmol}^{-1}$	H/Jmol <sup>-1</sup>	% neon
5.52(g)	151(4)	-213(16)	5.8(4)	-7213(20)	-10437(180)	592(24)	91(2)
5.52(l)	1382(8)	-5764(56)	5.54(4)	-7167(63)	-9454(659)	-5600(58)	3(1)
7.05(g)	190(2)	-255(6)	7.1(5)	-6995(7)	-10456(57)	550(9)	93(1)
7.05(l)	1377(10)	-5678(65)	7.05(2)	-6988(41)	-9638(409)	-5478(66)	5(1)
13.20(g)	349(5)	-457(10)	13.1(4)	-6459(9)	-10136(38)	360(18)	93.3(4)
13.20(l)	1369(7)	-5453(60)	13.25(2)	-6442(40)	-9524(245)	-5089(64)	8(1)
20.62(g)	524(15)	-710(39)	20.9(3)	-6088(11)	-10368(68)	154(53)	91(1)
20.62(l)	1384(13)	-5388(102)	20.6(2)	-6035(39)	-8733(197)	-4818(110)	11(1)
27.51(g)	639(18)	-861(67)	27.6(7)	-5827(26)	-9958(96)	93(74)	91(2)
27.51(l)	1375(12)	-5178(142)	27.7(2)	-5760(66)	-8964(305)	-4434(133)	14(2)
34.47(g)	726(10)	-958(26)	34.5(7)	-5580(18)	-9786(47)	89(35)	91(1)
34.47(l)	1396(11)	-5222(113)	34.7(3)	-5509(70)	-8102(289)	-4310(128)	15(1)
39.61(g)	767(14)	-988(41)	39.6(4)	-5427(16)	-9755(86)	133(43)	92(1)
39.61(l)	1346(9)	-4587(85)	39.7(4)	-5368(61)	-9095(504)	-3553(91)	24(1)

Table A.21: GEMC simulation results for the neon-argon mixture with the av45z potential along 110.78 K.

p/ MPa	$\rho/\text{kgm}^{-3}$	U/Jmol <sup>-1</sup>	p/ MPa	$\mu_{\text{ne}}/\text{Jmol}^{-1}$	$\mu_{\text{ar}}/\text{Jmol}^{-1}$	H/Jmol <sup>-1</sup>	% neon
5.23(g)	145(1)	-219(4)	5.56(2)	-8056(11)	-11086(41)	659(6)	86(1)
5.23(l)	1304(12)	-5315(80)	5.0(7)	-8011(88)	-10706(172)	-6166(83)	5(1)
8.27(g)	211(4)	-301(14)	8.31(4)	-7657(10)	-11042(72)	579(20)	89(1)
8.27(l)	1315(10)	-5296(72)	8.1(6)	-7613(27)	-10549(274)	-5060(76)	6(1)
12.20(g)	307(4)	-429(12)	12.22(3)	-7291(9)	-10910(50)	459(17)	89(1)
12.20(l)	1301(8)	-5074(60)	11.7(6)	-7276(36)	-10496(159)	-4734(63)	10(1)
20.10(g)	494(8)	-714(30)	20.1(1)	-6821(15)	-10651(51)	213(34)	87(1)
20.10(l)	1303(11)	-4869(95)	19.6(7)	-6743(40)	-10126(294)	-4312(87)	14(1)
23.92(g)	555(5)	-782(13)	24.0(2)	-6633(13)	-10602(26)	194(19)	88(1)
23.92(l)	1277(16)	-4561(119)	23.3(3)	-6595(54)	-10365(184)	-3902(118)	19(2)
28.61(g)	635(10)	-920(22)	28.7(2)	-6466(29)	-10479(47)	116(32)	86(1)
28.61(l)	1291(16)	-4558(121)	28.1(4)	-6448(22)	-9856(311)	-3776(123)	20(1)

Table A.22: GEMC simulation results for the neon-argon mixture with the av45z potential a.long 121.36 K.

p/ MPa	$\rho/\text{kgm}^{-3}$	U/Jmol <sup>-1</sup>	p/ MPa	$\mu_{\text{ne}}/\text{Jmol}^{-1}$	$\mu_{\text{ar}}/\text{Jmol}^{-1}$	H/Jmol <sup>-1</sup>	% neon
5.81(g)	106(3)	-320(13)	5.78(4)	-9145(23)	-11681(33)	604(21)	73(1)
5.81(l)	1237(11)	-4985(58)	5.8(4)	-9131(35)	-11659(232)	-4804(47)	4.4(3)
7.52(g)	200(7)	-363(35)	7.52(5)	-8827(31)	-11663(80)	571(52)	77(3)
7.52(l)	1236(12)	-4915(76)	7.4(4)	-8796(61)	-11583(118)	-4685(75)	6(1)
9.96(g)	263(9)	-463(36)	9.98(8)	-8507(23)	-11566(61)	466(48)	78(2)
9.96(l)	1215(3)	-4700(23)	9.8(8)	-8507(51)	-11443(217)	-4394(43)	8.9(4)
14.13g)	351(8)	-567(26)	14.15(6)	-8097(11)	-11535(42)	394(36)	81(1)
14.13(l)	1198(8)	-4448(51)	14.2(6)	-8100(35)	-11304(144)	-4009(43)	14(1)
16.96(g)	421(9)	-694(25)	16.9(2)	-7935(24)	-11422(18)	282(34)	79.1(4)
16.96(l)	1221(12)	-4513(94)	17.0(4)	-7912(39)	-11201(145)	-3995(91)	14(1)
18.79(g)	464(16)	-769(56)	18.8(2)	-7809(20)	-11392(36)	216(78)	79(2)
18.79(l)	1196(23)	-4289(158)	18.7(5)	-7796(32)	-11225(223)	-3720(158)	17(2)
19.79(g)	513(12)	-906(45)	19.7(1)	-7760(12)	-11322(22)	54(55)	76(1)
19.79(l)	1200(15)	-4294(98)	19.8(3)	-7766(27)	-11207(151)	-3792(94)	17(1)



Table A.23: GEMC simulation results for the neon-argon mixture with the av45z potential along 129.93 K.

p/ MPa	$\rho/\text{kgm}^{-3}$	U/Jmol <sup>-1</sup>	p/ MPa	$\mu_{\text{ne}}/\text{Jmol}^{-1}$	$\mu_{\text{ar}}/\text{Jmol}^{-1}$	H/Jmol <sup>-1</sup>	% neon
5.62(g)	166(3)	-411(12)	5.61(4)	-10159(5)	-12302(16)	541(18)	60(1)
5.62(l)	1171(17)	-4691(84)	5.6(4)	-10158(17)	-12176(175)	-4507(84)	4(1)
7.24(g)	208(7)	-474(38)	7.25(3)	-9810(20)	-12239(40)	478(51)	64(2)
7.24(l)	1162(9)	-4570(59)	7.3(5)	-9779(29)	-12136(85)	-4331(52)	6(1)
9.31(g)	258(6)	-540(20)	9.31(3)	-9469(14)	-12199(20)	419(33)	68(1)
9.31(l)	1155(8)	-4445(43)	9(1)	-9456(23)	-12055(70)	-4141(39)	8(1)
11.31(g)	305(3)	-606(19)	11.30(7)	-9213(12)	-12164(8)	361(28)	70(1)
11.31(l)	1129(33)	-4238(191)	11.4(5)	-9212(34)	-12085(58)	-3860(201)	11(2)
14.13(g)	374(6)	-731(28)	14.0(1)	-8948(18)	-12092(29)	248(35)	70(1)
14.13(l)	1117(21)	-4062(142)	14.5(3)	-8932(30)	-12110(111)	-3583(152)	15(2)
15.17(g)	406(14)	-797(54)	15.2(1)	-8850(30)	-12047(34)	182(67)	70(2)
15.17(l)	1101(53)	-3916(276)	15.4(7)	-8813(52)	-12024(54)	-3407(272)	17(3)

Table A.24: GEMC simulation results for the neon-argon mixture with the av45z plus AT potentials along 101.94 K.

p/ MPa	$\rho/\text{kgm}^{-3}$	U/Jmol <sup>-1</sup>	p/ MPa	$\mu_{\text{ne}}/\text{Jmol}^{-1}$	$\mu_{\text{ar}}/\text{Jmol}^{-1}$	H/Jmol <sup>-1</sup>	% neon
5.52(g)	157(5)	-232(16)	5.54(2)	-7232(10)	-10239(102)	563(26)	88(2)
5.52(l)	1295(8)	-5116(51)	5.4(5)	-7220(56)	-9996(289)	-4956(51)	5.3(5)
7.05(g)	199(4)	-287(14)	7.10(5)	-7017(16)	-10208(68)	508(18)	89.5(1)
7.05(l)	1300(11)	-5097(76)	6.8(8)	-6982(31)	-9864(102)	-4896(71)	6(1)
13.20(g)	363(6)	-501(18)	13.1(1)	-6488(13)	-10079(58)	301(26)	90(1)
13.20(l)	1291(17)	-4829(127)	13(1)	-6464(34)	-9670(70)	-4446(104)	11(2)
20.62(g)	555(10)	-796(27)	20.6(1)	-6104(17)	-9856(27)	49(38)	87(1)
20.62(l)	1287(15)	-4584(122)	20.6(4)	-6077(27)	-9518(260)	-3999(130)	16(2)
27.51(g)	685(40)	-1000(137)	27.8(6)	-5823(32)	-9742(69)	-68(157)	86(4)
27.51(l)	1244(13)	-4025(86)	27.4(7)	-5801(29)	-9431(293)	-3260(81)	26(1)
34.47(g)	783(32)	-1167(109)	34.6(2)	-5605(18)	-9589(44)	-142(125)	84(3)
34.47(l)	1222(4)	-3680(27)	34.6(4)	-5571(33)	-9378(162)	-2733(28)	32.6(4)

Table A.25: GEMC simulation results for the neon-argon mixture with the av45z plus AT potentials along 110.78 K.

p/ MPa	$\rho/\text{kgm}^{-3}$	U/ Jmol <sup>-1</sup>	p/ MPa	$\mu_{\text{ne}}/\text{Jmol}^{-1}$	$\mu_{\text{ar}}/\text{Jmol}^{-1}$	H/ Jmol <sup>-1</sup>	% neon
5.53(g)	161(4)	-294(18)	5.54(3)	-8134(13)	-10745(59)	553(29)	78(2)
5.53(l)	1221(6)	-4753(38)	5.4(4)	-8121(23)	-10676(42)	-4583(42)	5.8(3)
8.27(g)	227(5)	-365(17)	8.26(3)	-7712(13)	-10747(52)	490(24)	83(2)
8.27(l)	1214(10)	-4598(70)	8.1(9)	-7704(43)	-10693(104)	-4344(83)	9(1)
12.20(g)	341(8)	-550(26)	12.3(2)	-7344(20)	-10555(111)	303(32)	82(1)
12.20(l)	1217(24)	-4486(167)	11.7(5)	-7346(15)	-10598(34)	-4127(168)	12(2)
17.24(g)	488(34)	-798(102)	17.3(3)	-6998(22)	-10493(43)	57(133)	80(3)
17.24(l)	1205(13)	-4234(92)	16.8(5)	-6996(39)	-10355(247)	-3725(98)	17(1)
20.10(g)	578(34)	-1008(127)	20.2(2)	-6861(23)	-10414(17)	-140(153)	76(4)
20.10(l)	1183(20)	-3991(148)	19.8(6)	-6857(60)	-10372(52)	-3394(151)	21(2)
23.92(g)	609(38)	-973(124)	24.0(6)	-6671(24)	-10424(47)	-25(138)	81(3)
23.92(l)	1144(16)	-3595(105)	24(1)	-6654(31)	-10456(120)	-2889(106)	28(2)

Table A.26: GEMC simulation results for the neon-argon mixture with the av45z plus AT potentials along 121.36 K.

p/ MPa	$\rho$ /kgm <sup>-3</sup>	U/Jmol <sup>-1</sup>	p/ MPa	$\mu_{\text{ne}}$ /Jmol <sup>-1</sup>	$\mu_{\text{ar}}$ /Jmol <sup>-1</sup>	H/Jmol <sup>-1</sup>	% neon
5.81(g)	178(6)	-414(26)	5.78(2)	-9235(27)	-11482(35)	470(40)	64(2)
5.81(l)	1165(11)	-4518(61)	6(1)	-9216(29)	-11502(158)	-4310(74)	5.1(3)
7.52(g)	231(10)	-509(43)	7.53(7)	-8905(27)	-11432(46)	364(59)	67(3)
7.52(l)	1154(18)	-4391(101)	7.6(6)	-8893(17)	-11428(141)	-4140(93)	7(1)
9.96(g)	302(13)	-619(53)	9.9(2)	-8579(15)	-11356(34)	253(79)	79(2)
9.96(l)	1157(22)	-4325(123)	10(1)	-8579(41)	-11355(118)	-3998(114)	10(1)
14.13(g)	407(29)	-764(106)	14.12(2)	-8155(22)	-11308(65)	131(139)	72(4)
14.13(l)	1132(38)	-4020(235)	14.12(5)	-8140(21)	-11350(117)	-3562(245)	15(3)
16.96(g)	497(11)	-981(24)	16.9(2)	-7986(38)	-11239(20)	-83(33)	68(1)
16.96(l)	1126(54)	-3907(327)	17.0(8)	-7983(44)	-111861(125)	-3358(318)	17(4)

Table A.27: GEMC simulation results for the neon-argon mixture with the av45z plus AT potentials along 129.93 K.

p/ MPa	$\rho/\text{kgm}^{-3}$	U/Jmol <sup>-1</sup>	p/ MPa	$\mu_{\text{ne}}/\text{Jmol}^{-1}$	$\mu_{\text{ar}}/\text{Jmol}^{-1}$	H/Jmol <sup>-1</sup>	% neon
5.62(g)	205(6)	-629(39)	5.71(6)	-10339(28)	-12081(18)	231(55)	46(2)
5.62(l)	1086(14)	-4194(60)	5.7(9)	-10333(16)	-12092(118)	-3994(54)	4.6(4)
7.24(g)	241(14)	-625(77)	7.40(9)	-9880(58)	-12085(38)	267(110)	55(4)
7.24(l)	1068(32)	-4024(170)	7.4(7)	-9872(44)	-12055(63)	-3762(175)	7(1)
9.31(g)	313(16)	-781(78)	9.5(1)	-9531(43)	-12024(38)	88(111)	57(3)
9.31(l)	1022(44)	-3709(216)	9(1)	-9502(54)	-12027(119)	-3378(207)	12(2)
11.31(g)	396(25)	-980(107)	11.6(1)	-9303(27)	-11954(22)	-131(141)	55(3)
11.31(l)	1029(31)	-3667(149)	11.2(5)	-9289(26)	-12051(126)	-3264(168)	14(1)
14.13(g)	541(84)	-1386(364)	14.2(5)	-9005(36)	-11917(18)	-591(452)	51(7)
14.13(l)	941(80)	-3105(382)	14.1(5)	-8991(57)	-11948(116)	-2567(414)	22(5)

Table A.28: GEMC simulation results for the neon-argon mixture with the av5z potential along 95.82 K.

p/ MPa	$\rho/\text{kgm}^{-3}$	U/Jmol <sup>-1</sup>	p/ MPa	$\mu_{\text{ne}}/\text{Jmol}^{-1}$	$\mu_{\text{ar}}/\text{Jmol}^{-1}$	H/Jmol <sup>-1</sup>	% neon
4.16(g)	121(2)	-165(7)	4.15(2)	-6893(9)	-9713(63)	598(9)	89(1)
4.16(l)	1333(9)	-5245(54)	4.2(4)	-6849(39)	-9286(254)	-5124(44)	3.2(4)
6.94(g)	202(4)	-262(12)	6.95(4)	-6466(11)	-9615(73)	493(21)	91(1)
6.94(l)	1330(19)	-5123(132)	6.9(2)	-6432(56)	-9207(302)	-4924(136)	6(1)
8.62(g)	246(3)	-308(8)	8.64(4)	-6288(10)	-9628(54)	456(13)	92(1)
8.62(l)	1324(8)	-5035(66)	8.6(6)	-6253(40)	-9252(302)	-4788(72)	7(1)
10.33(g)	291(5)	-359(14)	10.36(5)	-6141(17)	-9610(92)	414(16)	92(1)
10.33(l)	1327(17)	-4996(135)	10.5(5)	-6083(58)	-9135(193)	-4694(142)	8(2)
20.86(g)	555(12)	-716(32)	20.82(7)	-5557(11)	-9286(25)	118(45)	89(1)
20.86(l)	1318(10)	-4652(84)	20.8(4)	-5529(16)	-8939(132)	-4070(75)	15(2)
27.61(g)	660(7)	-842(27)	27.5(3)	-5308(13)	-9166(27)	85(34)	89(1)
27.61(l)	1296(27)	-4314(246)	27.5(4)	-5290(23)	-8701(260)	-3555(245)	21(4)
41.71(g)	893(30)	-1366(135)	41.6(4)	-4879(35)	-8711(108)	-244(140)	80(3)
41.71(l)	1295(8)	-3976(67)	41.6(9)	-4846(41)	-8216(207)	-2875(69)	28(1)

Table A.29: GEMC simulation results for the neon-argon mixture with the av5z potential along 101.94 K.

p/ MPa	$\rho/\text{kgm}^{-3}$	U/Jmol <sup>-1</sup>	p/ MPa	$\mu_{\text{ne}}/\text{Jmol}^{-1}$	$\mu_{\text{ar}}/\text{Jmol}^{-1}$	H/Jmol <sup>-1</sup>	% neon
5.52(g)	158(4)	-229(15)	5.53(5)	-7241(14)	-10056(73)	577(21)	86(2)
5.52(l)	1290(5)	-4977(24)	5.5(4)	-7189(19)	-9897(218)	-4812(20)	4.5(1)
7.05(g)	197(2)	-270(4)	7.03(5)	-7020(10)	-10031(15)	538(5)	87.4(2)
7.05(l)	1280(12)	-4858(76)	7.1(6)	-7027(30)	-9838(193)	-4645(70)	6.0(4)
13.20(g)	363(13)	-486(38)	13.2(1)	-6463(16)	-9861(87)	338(51)	88(2)
13.20(l)	1260(6)	-4526(49)	13.4(2)	-6445(28)	-9659(134)	-4128(51)	12(1)
20.62(g)	533(14)	-722(43)	20.8(2)	-6056(23)	-9696(44)	168(56)	86(2)
20.62(l)	1234(13)	-4118(82)	20.8(5)	-6031(30)	-9568(95)	-3513(74)	20(1)
27.51(g)	661(7)	-932(20)	27.4(2)	-5783(20)	-9527(44)	35(18)	84(1)
27.51(l)	1238(7)	-3969(53)	27.2(7)	-5794(29)	-9460(150)	-3195(69)	24(1)
34.47(g)	750(10)	-1048(34)	34.4(3)	-5528(8)	-9358(23)	24(37)	84(1)
34.47(l)	1240(17)	-3807(132)	34.2(7)	-5484(41)	-9084(205)	-2858(140)	28(2)
39.61(g)	830(50)	-1253(215)	39.6(5)	-5402(17)	-9249(29)	-101(225)	80(6)
39.61(l)	1125(15)	-2868(102)	39.7(4)	-5387(32)	-9094(107)	-1776(103)	45(2)

Table A.30: GEMC simulation results for the neon-argon mixture with the av5z potential along 110.78 K.

p/ MPa	$\rho/\text{kgm}^{-3}$	U/Jmol <sup>-1</sup>	p/ MPa	$\mu_{\text{ne}}/\text{Jmol}^{-1}$	$\mu_{\text{ar}}/\text{Jmol}^{-1}$	H/Jmol <sup>-1</sup>	% neon
5.53(g)	157(2)	-262(9)	5.54(2)	-8120(9)	-10684(33)	601(14)	78(1)
5.53(l)	1206(16)	-4560(85)	5.25(5)	-8128(37)	-10685(79)	-4393(89)	5.5(6)
8.27(g)	228(7)	-350(24)	8.27(5)	-7703(11)	-10614(66)	517(34)	81(2)
8.27(l)	1185(12)	-4331(68)	7.6(3)	-7706(16)	-10569(142)	-4088(65)	9.2(6)
12.20(g)	327(7)	-486(25)	12.2(1)	-7319(17)	-10492(38)	394(37)	82(1)
12.20(l)	1177(15)	-4145(85)	11.6(6)	-7334(18)	-10469(60)	-3780(79)	13(1)
20.10(g)	517(15)	-774(47)	20.2(2)	-6795(17)	-10290(31)	162(60)	81(2)
20.10(l)	1112(17)	-3479(308)	19.4(4)	-6779(14)	-10226(111)	-2872(314)	26(4)
23.92(g)	595(25)	-913(88)	23.9(2)	-6618(5)	-10213(19)	66(107)	79(3)
23.92(l)	1077(37)	-3151(216)	23.9(3)	-6599(15)	-10174(94)	-2408(229)	32(3)
27.27(g)	699(24)	-1193(88)	27.2(2)	-6507(16)	-10098(27)	-199(105)	73(3)
27.27(l)	1082(55)	-3062(343)	27.0(4)	-6485(42)	-10061(147)	-2239(351)	35(6)



Table A.31: *ab initio* potentials ( $\mu E_h$ ) for the argon–krypton dimer.

R (Å)	avtz	avqz	av34z
3.0	7174.65	6391.43	5819.89
3.2	2913.43	2402.79	2030.16
3.4	918.91	595.46	359.43
3.6	49.5	-151.07	-297.43
3.8	-282.02	-404.78	-494.36
4.0	-369.19	-444.64	-499.70
4.2	-354.71	-402.15	-436.77
4.4	-305.11	-336.15	-358.80
4.6	-249.76	-270.73	-286.10
4.8	-199.43	-214.13	-224.86
5.0	-157.83	-168.27	-175.89
6.0	-51.02	-53.11	-54.64
8.0	-8.29	-8.58	-8.79
10.0	-2.11	-2.17	-2.21

Table A.32: Parameters of fitting for the argon–krypton potential.

Parameter	av34z
A ( $E_h$ )	112.08
$\alpha$ ( $a_0^{-1}$ )	1.42241
$\beta$ ( $a_0^{-2}$ )	-.040
$b$ ( $a_0^{-1}$ )	1.50
$C_6$ ( $E_h a_0^6$ )	94.08
$C_8$ ( $E_h a_0^8$ )	2452.27
$C_{10}$ ( $E_h a_0^{10}$ )	93790.30

Table A.33: GEMC simulation results for the argon–krypton mixture with the two-body *ab initio* potentials at 193.15 K.

p/ atm	$\rho/\text{kgm}^{-3}$	U/Jmol <sup>-1</sup>	p/ atm	$\mu_{\text{ar}}/\text{Jmol}^{-1}$	$\mu_{\text{kr}}/\text{Jmol}^{-1}$	H/Jmol <sup>-1</sup>	% krypton
35.00(g)	216(3)	-935(28)	35.0(2)	-20362(17)	-21325(11)	212(50)	68.2(2)
35.00(l)	1785(34)	-6107(123)	36(4)	-20387(81)	-21525(133)	-5953(112)	88.4(6)
37.75(g)	233(4)	-996(26)	37.7(3)	-20099(14)	-21337(10)	129(40)	64.9(4)
37.75(l)	1762(39)	-6028(138)	33(4)	-20065(100)	-21457(100)	-5886(140)	86(1)
40.23(g)	259(8)	-1107(37)	40.2(5)	-19965(46)	-21303(22)	-30(69)	64(1)
40.23(l)	1751(38)	-5982(120)	43(10)	-19932(120)	-21321(150)	-5797(123)	85(1)
45.22(g)	282(5)	-1178(33)	45.3(3)	-19452(42)	-21422(42)	-129(49)	55(1)
45.22(l)	1675(25)	-5729(89)	45(8)	-19445(24)	-21473(52)	-5531(59)	79.0(3)
50.17(g)	328(13)	-1383(77)	50.3(3)	-19234(33)	-21439(16)	-397(110)	53(1)
50.17(l)	1647(35)	-5626(126)	51(4)	-19241(39)	-21528(71)	-5399(121)	76(1)

Table A.34: GEMC simulation results for the argon–krypton mixture with the two-body *ab initio* potentials at 177.38 K.

p/ atm	$\rho/\text{kgm}^{-3}$	$U/\text{Jmol}^{-1}$	p/ atm	$\mu_{\text{ar}}/\text{Jmol}^{-1}$	$\mu_{\text{kr}}/\text{Jmol}^{-1}$	$H/\text{Jmol}^{-1}$	% krypton
25.37(g)	144(2)	-651(10)	25.3(2)	-18371(35)	-20016(19)	492(18)	55(1)
25.37(l)	1939(16)	-6703(62)	27(8)	-18304(106)	-19987(205)	-6598(78)	85.5(5)
30.16(g)	159(2)	-706(11)	30.2(3)	-17813(29)	-20209(32)	425(18)	43(1)
30.16(l)	1783(19)	-6147(70)	23(9)	-17795(73)	-20427(90)	-6061(64)	76(1)
35.10(g)	188(5)	-833(23)	35.1(2)	-17517(45)	-20235(73)	224(34)	39(2)
35.10(l)	1734(32)	-5985(113)	35(9)	-17505(111)	-20237(76)	-5845(130)	71(1)
40.26(g)	227(6)	-998(20)	40.0(3)	-17269(32)	-20245(22)	6(38)	35.3(4)
40.26(l)	1659(31)	-5735(109)	43(6)	-17183(94)	-20271(161)	-5558(99)	66(1)
45.22(g)	246(10)	-1073(46)	44.7(3)	-17067(42)	-20389(79)	-85(74)	31(2)
45.22(l)	1576(41)	-5473(130)	44(3)	-17043(112)	-20413(143)	-5288(131)	59(2)
50.17(g)	308(8)	-1354(42)	50.4(8)	-16871(21)	-20457(28)	-475(60)	29(1)
50.17(l)	1452(20)	-5051(62)	52(3)	-16928(36)	-20561(99)	-4827(53)	52(1)
55.09(g)	474(66)	-2002(237)	55(1)	-16719(16)	-20534(28)	-1363(315)	30(1)
55.09(l)	1421(34)	-4970(111)	58(3)	-16728(50)	-20618(97)	-4722(119)	48(1)

Table A.35: GEMC simulation results for the argon–krypton mixture with the two-body *ab initio* potentials at 163.15 K.

p/ atm	$\rho/\text{kgm}^{-3}$	U/Jmol <sup>-1</sup>	p/ atm	$\mu_{\text{Ar}}/\text{Jmol}^{-1}$	$\mu_{\text{Kr}}/\text{Jmol}^{-1}$	H/Jmol <sup>-1</sup>	% krypton
20.29(g)	105(1)	-492(8)	20.3(1)	-16508(26)	-18935(23)	617(15)	38(1)
20.29(l)	2003(23)	-6999(84)	21(12)	-16428(28)	-18864(262)	-6924(60)	80(1)
25.23(g)	123(2)	-569(9)	25.3(3)	-16013(5)	-19238(27)	504(14)	25.5(3)
25.23(l)	1771(26)	-6194(91)	22(3)	-15990(66)	-19071(153)	-6110(92)	64(2)
30.26(g)	151(1)	-703(6)	30.3(4)	-15742(41)	-19321(93)	310(14)	22(2)
30.26(l)	1660(23)	-5832(77)	29(7)	-15722(54)	-19228(203)	-5719(84)	55(1)
35.28(g)	178(2)	-832(9)	35.3(3)	-15518(9)	-19484(43)	133(13)	18(1)
35.28(l)	1502(25)	-5329(91)	36.0(5)	-15488(43)	-19537(55)	-5190(76)	44(1)
40.16(g)	211(6)	-984(40)	40.1(5)	-15341(30)	-19661(72)	85(66)	15(1)
40.16(l)	1389(22)	-4969(70)	44(7)	-15395(30)	-19638(70)	-4790(65)	37(1)
45.30(g)	259(9)	-1199(46)	45.3(7)	-15166(19)	-19993(48)	-393(82)	12(1)
45.30(l)	1226(23)	-4486(70)	44(6)	-15174(37)	-20047(62)	-4302(46)	26(1)
50.29(g)	360(59)	-1589(238)	50(1)	-15056(26)	-20181(49)	-927(338)	10.5(8)
50.29(l)	1165(33)	-4316(119)	56(4)	-15038(25)	-20194(789)	-4076(133)	21.8(3)

Table A.36: GEMC simulation results for the argon–krypton mixture with the two-body *ab initio* potentials at 158.15 K.

P/ atm	$\rho/\text{kgm}^{-3}$	$U/\text{Jmol}^{-1}$	p/ atm	$\mu_{\text{ar}}/\text{Jmol}^{-1}$	$\mu_{\text{kr}}/\text{Jmol}^{-1}$	$H/\text{Jmol}^{-1}$	% krypton
12.63(g)	68(1)	-325(9)	12.65(4)	-16679(19)	-18467(35)	821(17)	47(1)
12.63(l)	2164(24)	-7626(99)	17(7)	-16504(105)	-18145(449)	-7569(101)	88(1)
15.41(g)	81(1)	-390(8)	15.38(4)	-16297(18)	-18441(27)	722(11)	41(1)
15.41(l)	2099(21)	-7370(87)	27(8)	-16149(104)	-18114(320)	-7295(91)	83.7(5)
20.26(g)	98(1)	-464(12)	20.3(1)	-15718(24)	-18726(55)	620(17)	27(1)
20.26(l)	1924(33)	-6751(118)	21(10)	-15602(131)	-18777(267)	-6678(112)	71(2)
25.22(g)	123(1)	-586(9)	25.2(1)	-15359(17)	-18871(59)	439(13)	21(1)
25.22(l)	1780(20)	-6270(68)	30(3)	-15413(59)	-18735(92)	-6158(74)	60(1)
30.22(g)	147(3)	-703(11)	30(1)	-15086(28)	-19156(96)	272(22)	15(1)
30.22(l)	1566(22)	-5581(77)	30(8)	-15107(33)	-19300(124)	-5473(77)	44(1)
35.41(g)	181(2)	-871(16)	35.7(3)	-14860(21)	-19437(70)	28(27)	11(1)
35.41(l)	1360(23)	-4947(70)	34(5)	-14877(29)	-19441(43)	-4814(66)	31(1)
40.42(g)	211(3)	-1013(24)	40.4(4)	-14706(8)	-19849(58)	-169(35)	8.0(4)
40.42(l)	1178(30)	-4396(98)	40(4)	-14734(30)	-19873(74)	-4230(88)	20(1)
45.56(g)	301(36)	-1429(172)	45.9(2)	-14585(28)	-19948(49)	-744(253)	7.8(3)
45.56(l)	1178(29)	-4416(95)	50(7)	-14640(22)	-19964(55)	-4216(79)	18(1)
47.37(g)	330(61)	-1553(273)	48(1)	-14541(15)	-20269(47)	-905(368)	6(1)
47.37(l)	1081(26)	-4122(97)	47(4)	-14585(16)	-20286(60)	-3924(115)	13(1)

Table A.37: GEMC simulation results for the argon–krypton mixture with the two-body *ab initio* potentials at 193.15 K.

p/ atm	$\rho$ /kgm <sup>-3</sup>	U/Jmol <sup>-1</sup>	p/ atm	$\mu_{\text{Ar}}$ /Jmol <sup>-1</sup>	$\mu_{\text{Kr}}$ /Jmol <sup>-1</sup>	H/Jmol <sup>-1</sup>	% krypton
37.75(g)	297(12)	-1268(47)	38.1(6)	-21375(42)	-20926(28)	-262(69)	85.1(1)
37.75(l)	1737(26)	-5766(93)	45(5)	-21382(51)	-21076(35)	-5563(106)	94.2(4)
40.23(g)	363(39)	-1586(192)	40.2(8)	-21047(85)	-20890(35)	-718(276)	83.6(2)
40.23(l)	1759(29)	-5837(104)	51(10)	-20996(98)	-21117(70)	-5609(101)	93.3(3)
45.22(g)	380(25)	-1587(115)	45.1(5)	-20245(47)	-20985(28)	-711(162)	74.7(5)
45.22(l)	1672(11)	-5552(34)	45(9)	-20237(54)	-21234(89)	-5350(26)	87.7(4)
50.17(g)	458(36)	-1858(163)	50.1(4)	-19691(55)	-21053(18)	-1077(225)	68.3(3)
50.17(l)	1676(46)	-5581(167)	52(14)	-19726(92)	-21335(55)	-5353(119)	84(1)
55.11(g)	543(107)	-2102(316)	55(2)	-19326(94)	-21158(36)	-1388(425)	63(1)
55.11(l)	1493(113)	-4967(358)	54(6)	-19345(105)	-21378(59)	-4703(379)	77(2)

Table A.38: GEMC simulation results for the argon–krypton mixture with the two-body plus AT potentials at 177.38 K.

p/ atm	$\rho/\text{kgm}^{-3}$	$U/\text{Jmol}^{-1}$	p/ atm	$\mu_{\text{ar}}/\text{Jmol}^{-1}$	$\mu_{\text{kr}}/\text{Jmol}^{-1}$	$H/\text{Jmol}^{-1}$	% krypton
25.37(g)	175(1)	-795(13)	25.4(4)	-19283(80)	-19552(15)	288(16)	76(1)
25.37(l)	1904(35)	-6375(137)	22(4)	-19202(134)	-19759(105)	-6286(141)	93(1)
30.16(g)	200(4)	-889(15)	30.4(3)	-18413(19)	-19658(14)	155(26)	63(1)
30.16(l)	1792(27)	-5972(99)	28(7)	-18361(37)	-19713(109)	-5854(129)	86(1)
35.10(g)	222(9)	-959(45)	35.3(6)	-17837(71)	-19808(44)	55(71)	52(2)
35.10(l)	1650(48)	-5496(167)	38(5)	-17848(50)	-19898(64)	-5328(166)	78(2)
40.26(g)	268(14)	-1152(71)	40.0(8)	-17640(37)	-19776(25)	-210(112)	48(1)
40.26(l)	1647(59)	-5487(204)	41(7)	-17647(38)	-19850(86)	-5307(194)	73(1)
45.22(g)	317(29)	-1339(115)	46(1)	-17341(39)	-19880(40)	-462(174)	45(1)
45.22(l)	1568(17)	-5229(60)	47(10)	-17380(94)	-20028(33)	-5025(75)	66.8(5)
50.17(g)	366(21)	-1520(90)	50.0(3)	-17104(13)	-19985(26)	-714(123)	41(1)
50.17(l)	1485(40)	-4979(138)	50(7)	-17120(59)	-20127(98)	-4757(146)	62(1)
55.09(g)	508(68)	-2038(246)	55(2)	-16919(46)	-20077(35)	-1388(329)	40(1)
55.09(l)	1539(70)	-5214(259)	54(10)	-16976(45)	-20382(131)	-4989(271)	60(2)

Table A.39: GEMC simulation results for the argon–krypton mixture with the two-body plus AT potentials at 163.15 K.

p/ atm	$\rho/\text{kgm}^{-3}$	U/Jmol <sup>-1</sup>	p/ atm	$\mu_{\text{Ar}}/\text{Jmol}^{-1}$	$\mu_{\text{Kr}}/\text{Jmol}^{-1}$	H/Jmol <sup>-1</sup>	% krypton
20.29(g)	119(3)	-559(22)	20.3(2)	-16780(17)	-18564(16)	511(34)	49.6(1)
20.29(l)	2104(28)	-7307(115)	25(25)	-16738(158)	-19245(153)	-7231(157)	87(1)
25.23(g)	152(5)	-707(27)	25.3(1)	-16377(29)	-18530(45)	295(50)	44(1)
25.23(l)	1924(26)	-6516(95)	27(12)	-16381(85)	-18776(174)	-6420(82)	80(1)
30.26(g)	175(3)	-801(20)	30.4(6)	-15998(49)	-18694(51)	174(23)	36(2)
30.26(l)	1746(67)	-5885(238)	34(3)	-15997(70)	-18839(87)	-5754(249)	70(3)
35.28(g)	216(5)	-988(33)	35.1(2)	-15713(15)	-18814(10)	-105(54)	30.4(4)
35.28(l)	1662(67)	-5636(241)	35(7)	-15747(33)	-19057(61)	-5500(257)	62(3)
40.16(g)	258(11)	-1163(47)	40.2(7)	-15488(19)	-18972(15)	-348(68)	26(1)
40.16(l)	1535(18)	-5227(65)	47(5)	-15538(29)	-19127(90)	-5038(56)	53(1)
45.30(g)	300(15)	-1334(73)	46(1)	-15287(19)	-19238(8)	-575(93)	20.6(4)
45.30(l)	1345(27)	-4645(89)	50(4)	-15309(46)	-19320(58)	-4434(83)	41.1(5)



Table A.40: GEMC simulation results for the argon–krypton mixture with the two-body plus AT potentials at 158.15 K.

p/ atm	$\rho/\text{kgm}^{-3}$	$\bar{U}/\text{Jmol}^{-1}$	p/ atm	$\mu_{\text{ar}}/\text{Jmol}^{-1}$	$\mu_{\text{kr}}/\text{Jmol}^{-1}$	$H/\text{Jmol}^{-1}$	% krypton
12.63(g)	80(2)	-397(7)	12.7(1)	-17259(43)	-18007(31)	710(18)	66(1)
12.63(l)	2086(18)	-7072(70)	13(6)	-17268(67)	-18039(190)	-7026(78)	93(1)
15.41(g)	96(1)	-466(13)	15.49(5)	-16742(13)	-17976(15)	608(25)	58.4(4)
15.41(l)	2079(17)	-7069(67)	22(17)	-16696(104)	-18186(134)	-6990(49)	90(1)
20.26(g)	114(3)	-544(18)	20.3(1)	-15988(33)	-18177(47)	500(32)	41(2)
20.26(l)	1949(45)	-6624(173)	21(6)	-15990(103)	-18362(88)	-6548(181)	80(2)
25.22(g)	149(5)	-709(25)	25.3(4)	-15592(15)	-18193(31)	243(38)	35(1)
25.22(l)	1882(13)	-6407(50)	38(12)	-15542(110)	-18454(132)	-6270(50)	73(1)
30.22(g)	173(3)	-808(13)	30.3(3)	-15262(50)	-18415(86)	112(17)	27(2)
30.22(l)	1784(127)	-6122(475)	32(14)	-15295(93)	-18706(64)	-6006(473)	65(6)
35.41(g)	211(8)	-987(43)	35.5(3)	-15021(14)	-18600(67)	-137(67)	22(2)
35.41(l)	1651(89)	-5692(332)	30(9)	-15056(14)	-18879(83)	-5586(315)	55(3)
40.42(g)	257(8)	-1190(35)	40.4(3)	-14831(12)	-18813(29)	-419(50)	18.4(3)
40.42(l)	1460(37)	-5088(123)	34(5)	-14909(41)	-19048(82)	-4960(140)	42(2)

## Erklärung

“Ich versichere, daß ich die von mir vorgelegte Dissertation selbständig angefertigt, die benutzten Quellen und Hilfsmittel vollständig angegeben und die Stellen der Arbeit — einschließlich Tabellen, Karten und Abbildungen —, die anderen Werken im Wortlaut oder dem Sinn nach entnommen sind, in jedem Einzelfall als Entlehnung kenntlich gemacht habe; daß diese Dissertation noch keiner anderen Fakultät oder Universität zur Prüfung vorgelegen hat; daß sie — abgesehen von unten angegebenen Teilpublikationen — noch nicht veröffentlicht worden ist sowie, daß sich eine solche Veröffentlichung vor Abschluß des Promotionsverfahrens nicht vornehmen werde. Die Bestimmungen dieser Promotionsordnung sind mir bekannt. Die von mir vorgelegte Dissertation ist von (Prof. Dr. Ulrich K. Deiters) betreut worden.”

Name: Afshin Eskandari Nasrabad

Datum.....                      Unterschrift.....

## Lebenslauf

---

---

Name: Eskandari Nasrabad  
Vorname: Afshin  
Geschlecht: Männlich  
Geburtsdatum: 2 Aug. 1967  
Geburstort: Mashad (Iran)  
Familienstand: Ledig

Adresse:

Universität zu Köln  
Physikalische Chemie Institut  
A. K. Prof. U. K. Deiters  
Luxemburger Str. 116  
50939 Köln  
Deutschland

E-mail: Afshin.Eskandari@Uni-Koeln.De

---

Datum ..... Unterschrift .....

## Ausbildung:

---

---

Promotion:	Von Sommer Semester 2001 - 5 Feb. 2003 Physikalische Chemie Institut Universität zu Köln Deutschland
Betreuer:	Prof. Dr. U. K. Deiters
Titel meiner Dissertation:	“Global Simulation of Noble Gases and Their Binary Mixtures”

---

M.Sc. (Diplom):	Sep. 1994 - Feb. 1998 Chemistry Department Faculty of Science University of Teheran Teheran Iran
Betreuer:	Prof. Dr. Ali Maghari
Titel meiner Diplom Arbeit:	“Equilibrium Properties of Some Non Polar Dense Fluids”

---

B.Sc.	1988-1993 Chemie University of Isfahan Iran
-------	---

---